OXY-COMBUSTION OF FOSSIL FUEL IN A SWIRL STABILIZED NON-PREMIXED COMBUSTOR

BY

MOHAMMAD RAGHIB SHAKEEL

A Thesis Presented to the
DEANSHIP OF GRADUATE STUDIES

KING FAHD UNIVERSITY OF PETROLEUM & MINERALS

DHAHRAN, SAUDI ARABIA

In Partial Fulfillment of the
Requirements for the Degree of

MASTER OF SCIENCE

In

MECHANICAL ENGINEERING

MAY 2017

KING FAHD UNIVERSITY OF PETROLEUM & MINERALS

DHAHRAN- 31261, SAUDI ARABIA

DEANSHIP OF GRADUATE STUDIES

This thesis, written by **Mohammad Raghib Shakeel** under the direction of his thesis advisor and approved by his thesis committee, has been presented and accepted by the Dean of Graduate Studies, in partial fulfilment of the requirements for the degree of **MASTER OF SCIENCE IN MECHANICAL ENGINEERING.**

Dr. Esmail M. A. Mokheimer
(Advisor)

Dr. Mohamed A. Habib
(Member)

Dr. Zuhair M. Gasem
Department Chairman

Dr. Rached Ben Mansour
(Member)

Dr. Salam A. Zummo
Dean of Graduate Studies

16/7/2017
Date

DEDICATED TO

MY BELOVED PARENTS
AND

SIBLINGS

ACKNOWLEDGMENTS

All praise and thanks are due to Almighty Allah alone, for his mercy and guidance throughout my M.Sc. Program. I am grateful to KFUPM for providing me with the opportunity and scholarship to pursue my Master's degree.

I would like to express my profound gratitude and deep regards for my M.Sc. thesis advisor, Dr. Esmail Mokheimer for his guidance and support throughout my research work at KFUPM. I deeply appreciate and thank him for his patience, motivation, enthusiasm, insightful comments, mentorship and his kind advice during my thesis.

I also appreciate the help of Dr. Mohamed Habib for his invaluable discussions and important ideas during the course of my research. Special thanks to Dr. Rached Ben Mansour for introducing me to the world of numerical modelling and pushing me in the right direction when I was stuck in my thesis.

My profound thanks to Dr. Yinka Sanusi, from whom I learnt a lot about combustion modelling, and whose continuous help and guidance propelled my work.

I would like to acknowledge the assistance of Mr. Karam in setting up the experiments in the lab. I would also like to acknowledge my colleagues in the combustion research group, Mr. Zubairu Abubakr, Mr. Ibrahim Mansir, Mr. Mansur Aliyu and Mr. Abdul Rahman Magdy for the insightful, and fruitful discussions and also for their help in my coursework and thesis.

Thanks to the Indian community and all my friends Faisal Moiz Hussain, Ameeruddin Khaja, Basheeruddin, Suleman Haroon, Ataur Rahman and Dr. Allabaksh for making my stay at KFUPM a memorable experience.

Last but not the least, my deepest thanks and gratitude goes out to my Parents and my siblings. I would not have been here without their encouragement, help and support throughout my life.

TABLE OF CONTENTS

LIST OF TABLES

LIST OF FIGURES

LIST OF ABBREVIATIONS

CCS	Carbon Capture and Storage
CFD	Computational Fluid Dynamics
DO	Discrete Ordinate
EDC	Eddy Dissipation Concept
$EWBM$	Exponential Wide Band Model
GHG	Green House Gas
GRI	Gas Research Institute
JL	Jones-Lindstedt
LES	Large Eddy Simulation
MR	Molar Ratio
PPM	Parts Per Million
RNG	Renormalization Group
$SIMPLE$	Semi-Implicit Method for Pressure Linked Equations
WD	Westbrook-Dryer
$WSGGM$	Weighted Sum of Gray Gas Model

LIST OF SYMBOLS

A	Pre-exponential factor
A_r	Area of cross-section
A_A	Area of the oxidizer nozzle
A_F	Area of the fuel nozzle
a_j	Gas weighted fraction
b	Temperature Coefficient
C	Arbitrary constant
CO	Carbon monoxide
CO_2	Carbon dioxide
c_p	Specific heat at constant pressure (J/kg K)
D_c	Combustor diameter
D_j, m	Diffusion flux of species j (m^2/s)
d_F	Diameter of the fuel nozzle
d_{ox}	Diameter of the oxidizer orifice
d_{eff}	Effective diameter of the fuel nozzle
E_a	Activation energy (kJ/kmol K)
f_s	Stoichiometric oxidizer to fuel mass ratio
G_k	Turbulence Production energy
g	Acceleration due to gravity
H_2	Hydrogen

H_2O	Water
h	Enthalpy
k	Turbulent kinetic energy
k_f	Thermal conductivity
L	Flame length
$L_{n,e1}$,$L_{n,e2}$, $L_{n,e3}$	Empirical normalised flame length
$L_{n,m}$	Experimental normalised measured flame length
L_c	Length of the combustor
m	Metre, Unit of length
MR	Molar Ratio
n_{O_2}	Number of mole of oxygen per unit mole of the fuel mixture
P	Pressure (N/m^2)
P_{ij}	Compressive stress tensor
T_{ad}	Adiabatic flame temperature
T_{in}	Combustor temperature inlet
T	Temperature
t_F	Thickness of the fuel nozzle
u_A	Oxidizer velocity
u_F	Fuel velocity
u_{ox}	Oxidizer velocity
α_F	Thermal diffusivity of the fuel mixture
β	Temperature coefficient

ρ_F	Density of the fuel
ρ_{oxi}	Density of the oxidizer
ρ_A	Density of oxidizer
ρ_{O_2}	Density of oxygen
ρ_{eff}	Effective mixture density

ABSTRACT

Full Name : Mohammad Raghib Shakeel

Thesis Title : Oxy-Combustion of fossil fuel in a swirl-stabilized non-premixed combustor

Major Field : Mechanical Engineering

Date of Degree : May 2017

Oxyfuel combustion, involving combustion of fossil fuel with pure oxygen is a promising technology to reduce the CO_2 emissions by capturing and sequestering the CO_2 produced by fossil fuel combustion. In the present study, oxy-combustion of methane at stoichiometry is examined experimentally and numerically.

Experiments were carried out in a non-premixed combustor to study the flame stability and the flame length variation with varying CO_2 composition in the oxidizer mixture at stoichiometry. The firing rate of the combustor was varied between 2.5-4.5 MW/m^3-bar. The fuel used was 100% CH_4 and 20/80% H_2/CH_4 mixture. When the combustor was operated under gas turbine conditions (≥3.5 MW/m^3-bar), the flame transitions exhibited tri-modal regime below which the flame transitions exhibited bimodal regime. Weak flames at the nozzle exit were generally observed to precede the Attached flame → Lifted flame transition. The predicted flame length, using empirical equations based on the Near-field concept gave a good match within 5% of our experimentally observed flame length.

The temperature along the radius of the combustor was measured for validation of numerical models to have further insight into the Oxy-combustion dynamics of methane in a cost-effective way. A numerical model was developed to model the oxyfuel combustion. The developed model gave an insight into the flow dynamics, temperature distribution and the emissions from the combustor.

With increase in CO_2 percentage in the oxidizer stream the maximum temperature was found to decrease, but the CO emissions were found to increase. At stoichiometry, for energy level of 4 MW/m^3-bar, increasing the CO_2 composition in the O_2/CO_2 oxidizer from 0 to 40% led to a temperature reduction of 15.5% from 3292 K to 2782 K. For the same change in CO_2 composition, CO emission increased by 650%, from 682 ppm to 4958 ppm. However, for 40% CO_2 in the O_2/CO_2 oxidizer, the CO emission was reduced to 0.3 ppm by bringing down the equivalence ratio from 1 to 0.98. The decrease is attributed to excess O_2 which helps in oxidation of CO. At stoichiometry, for 40% CO_2 in the O_2/CO_2 oxidizer, the increase in the energy level of the combustor from 4 to 5 MW/m^3-bar, was found to decrease the CO emissions by 51 % from 4598 ppm to 2428 ppm, due to high temperatures inside the combustor which resulted in efficient burning. Based on the numerical study a new combustor head was designed which improved the swirl flow inside the combustor.

ملخص الرسالة

الاسم الكامل: محمد راغب شكيل

عنوان الرسالة: دراسة احتراق الوقود الأحفوري مع الأكسجين داخل غرفة احتراق مستقرة بالسريان الدوامي

التخصص: هندسة ميكانيكية

تاريخ الدرجة العلمية: مايو 2017

إن حرق الوقود مع الأكسجين يعتبر تقنية واعدة لتقليل انبعاثات ثاني أكسيد الكربون وذلك عن طريق فصله وتخزينه بعد عملية الاحتراق. تم في هذه الرسالة دراسة عملية وعددية لاحتراق غاز الميثان مع الأكسجين - مع حفظ نسب العناصر حسب معادلة الاحتراق الكيميائي – تجريبيا و عن طريق التحليل الرقمي. أجريت التجارب في غرفة احتراق حيث يمزج الوقود مع الأكسجين بعد دخولهما إلى داخل الغرفة. وذلك لدراسة تأثير نسبة ثاني أكسيد الكربون على استقرار اللهب وطوله مع مراعاة اكتمال احتراق الوقود وفقا لمعادلات التفاعل. معدل الاشتعال تم تغييره من 2.5 إلى 4.5 MW/m^3-bar. واستخدم نوعين من الوقود (ميثان نقي وخليط من 20% هيدروجين و80% ميثان) خلال التجارب.

عندما يتم تشغيل الحارق في ظروف التوربينات الغازية فإن تحولات اللهب تمر بثلاث مراحل. فقد لوحظ أن اللهب يتخذ أشكالا ثلاثة: أولها هو لهب ضعيف يوجد في نهاية فوهة غرفة الاحتراق يتلوه اللهب المتصل (أي الذي لا يلاحظ فيه فجوة بين اللهب والفوهة)، والمرحلة الأخيرة هو اللهب المرتفع الذي يتميز بوجود فجوة بينه وبين فوهة الاحتراق. في هذه الدراسة تم تطوير معادلات رياضية اعتماداً على نتائج التجارب ، و استطاعت هذه المعادلات أن تتوقع أطوال اللهب التي تم قياسها خلال التجارب المعملية بمعدل خطأ لا يزيد على 5 %.

إضافة إلى ذلك تم تطوير نموذج رقمي لمحاكاة عملية الاحتراق وتم التحقق من نتائج ذلك النموذج عن طريق القياس التجريبي لدرجات الحرارة على طول نصف قطر غرفة الاحتراق الاسطوانية وذلك لدراسة ديناميكية احتراق الميثان مع الأكسجين بشكل فعال اقتصادياً. النموذج الرقمي شرح العديد من خصائص عملية الاحتراق مثل ديناميكية السريان والتوزيع الحراري وكذلك انبعاثات الاحتراق.

لوحظ أن درجة الحرارة القصوى تقل عند زيادة نسبة ثاني أكسيد الكربون في تيار الأكسدة ، و لكن في نفس الوقت تزداد انبعاثات أول أكسيد الكربون بنسبة 650% وذلك من انبعاثات بمقدار 682 جزء في المليون إلى 4958 جزء في المليون. ولكن يمكن تخفيض هذه الانبعاثات إلى 0.3 جزء في المليون بتقليل النسبة المكافئة للاحتراق من 1 إلى 0.98 حيث يساهم الأكسجين الزائد في أكسدة أول أوكسيد الكربون و تحويله إلى ثاني أكسيد الكربون. كما إن زيادة معدلات الطاقة الداخلة إلى الحارق من 4 إلى 5 MW/m^3-bar تقلل كذلك من انبعاثات أول أكسيد الكربون بنسبة 51 % وذلك من 4598 جزء في المليون إلى 2248 جزء في المليون حيث تساهم درجات الحرارة العالية في تحقيق احتراق ذو كفاءة عالية يمنع تكون هذا الغاز. وبناء على نتائج هذه الدراسة تم تصميم غرفة احتراق جديدة زادت من كفاءة السريان الدوراني داخل الغرفة.

CHAPTER 1

INTRODUCTION

Every object we produce, devices we use requires energy to make and/or energy to transport, and the energy demands are closely linked to the economic growth of a country. Meeting the energy demand of over 7 billion people around the world while maintaining the environment is one of the major challenges for the human race.

1.1 Energy and Environment

Since the turn of the 20th century, the global concentration of greenhouse gases (GHG) has continued to increase dramatically [1]. The increased concentration of GHG has led to increase in global mean surface temperatures (GMST) [2]. The primary constituent of these greenhouse gases is carbon dioxide (CO_2) and methane (CH_4). Among the many human activities that produce greenhouse gases, the use of energy represents by far the largest source of emissions. Smaller shares correspond to agriculture, producing mainly CH_4 and N_2O from domestic livestock and rice cultivation, and to industrial processes not related to energy, producing mainly fluorinated gases and N_2O.

Heat and electricity generation industry has been identified as the single largest contributor to the emission of carbon dioxide. The latest report published by International Energy Agency (IEA) states that the heat and electricity generation sector alone contributed 42% of the total CO_2 emission from burning fossil fuels in the year 2014 [1]. The alarming rise in global temperature in the past century causing decrease in the volume of polar ice caps

and increase in the rise of sea levels has fuelled the need to mitigate greenhouse gas emissions. International treaties and agreements like the Kyoto Protocol and the Paris Climate agreement have mandated countries to lower GHG emissions with the aim of keeping the global temperature below 2°C of the pre-industrial era [3] global temperature.

While on the other hand, the energy demand of the world continues to increase [4]. The challenge is to meet the growing energy demand while limiting the GHG emission. One way is to move away from fossil fuels and increase reliability on other sources of energy like Nuclear, renewable sources like hydro, biogas and solar. However, due to the recent accident at Fukushima Daiichi nuclear plant in Japan, and the hazardous waste generation from nuclear energy, the interest in nuclear energy for power generation has been deteriorating [5–8], with many countries like Germany completely shutting down all their 17 nuclear plants [9]. Renewable sources like solar, hydro, geothermal, biomass, wind and ocean have been gaining momentum and popularity, however, the share of energy generated from renewable energy still remains below 14% [10]. Undoubtedly, renewable sources are the future for power generation but until such a time when they can be efficiently utilised to produce power, there is a need to make the currently available technologies more environment friendly while maintaining the efficiency of these technologies [11].

This has led to the development of clean combustion and carbon capture and storage (CCS) technology. The aim of this technology is to reduce the greenhouse emission gases while continuing to rely on fossil fuels for power generation. Coal, oil and natural gas are still the major fuels used for electric power generation [12] since they are the most abundant

resources and the technology for their utilisation are the most economically affordable and reliable. But with decreasing coal resources and the need for reduced emission, the use of CCS technologies such as oxyfuel combustion presents an attractive avenue, as such technologies can provide zero emission power.

1.2 Oxyfuel combustion

Oxyfuel combustion is a CCS technology which involves burning fossil fuels in the presence of pure oxygen. Due to this, the only products in the flue gas are CO_2 and H_2O. The flue gas can be easily condensed and the resulting CO_2 can be transported, to be stored in offsite areas. Thus, oxyfuel combustion can help capture and store CO_2. Since no nitrogen is present in the combustion process the use of oxyfuel technology almost completely eliminates NOx emissions which are a major concern when burning fuel in the air.

1.3 Problem Statement

The major concern with burning fossil fuels (e.g., methane) with pure oxygen is the stability and the high temperatures associated with oxyfuel combustion. To control the stability and high temperatures a certain fixed amount of flue gas containing mostly CO_2 is recirculated back into the combustion chamber which not only enhances the mixing of the methane gas but also helps to bring down the high temperatures. Earlier works by Nemitallah and Habib [13] focussed on equivalence ratio between 0.55-0.75. However, one of the major challenges with using oxyfuel combustion is the high-energy cost required to separate oxygen from air. Oxygen production consumes a part of the produced energy

in oxyfuel combustion technology, which brings down the system efficiency and adds to the cost of energy.

Burning the fuel in lean conditions where more oxygen is supplied than the stoichiometric necessity, wastes a considerable amount of oxygen and hence a considerable amount of energy. As such, oxyfuel combustion of fossil fuels closer to the stoichiometry is of interest to enhance the efficiency of practical systems.

Numerical models help in studying the flame structure and also in predicting the flame behaviour under changing conditions. One of the prominent difficulty in setting up a numerical model for turbulent combustion is the modelling of chemical kinetics that takes place in the combustion chamber. While there are many reaction mechanisms to model methane-air combustion, very few exist for oxyfuel combustion of methane. Therefore, developing a validated numerical model to simulate the oxyfuel combustion will help in studying the flame characteristics without much dependence on experiments.

1.4 Objectives

The main objectives of the thesis are to experimentally and numerically study the flame characteristics, emission and temperatures for oxyfuel combustion of fossil fuel gases in an atmospheric diffusion gas turbine model combustor.

The specific objectives to achieve the above are:

1. To develop a numerical model to simulate the observed flame characteristics and emissions in the model combustor.

2. To conduct experimental study for some cases for validating the developed mathematical model and the developed numerical scheme.
3. To study the effects of oxidizer (CO_2) dilution on the flame stability, structure and emission for different fuel composition.

1.5 Methodology

The procedure for obtaining the specific objectives of the work is highlighted in this section.

1. Experiments are carried out in a non-premixed swirl stabilised combustor with 45° swirl angle with methane as fuel in a CO_2/O_2 environment. CO_2 sweep test is carried out to study the effect of CO_2 addition of flame structure, and length of flame.
2. Temperature data at different points in the combustor is recorded for Numerical validation.
3. A numerical model is developed and validated with experimental data to study the effect of CO_2 addition on the flame temperature and emission. The effect of change in energy level (2.5-5 Mw/m^3) and equivalence ratio (0.8-1.0) is also examined.
4. Based on findings from above work a new burner head design is proposed and studied to enhance the swirling of flow inside the combustor.

CHAPTER 2

LITERATURE REVIEW

2.1 Carbon Capture and Storage and Utilisation

Carbon capture and storage (CCS) is a technology that in recent years have gained widescale popularity, as an effective method to reduce the greenhouse gas emissions. Use of CCS can reduce the CO_2/kWh by 80-90% CO_2/kWh in comparison to air fired plants [14]. The technology involves three stages:

- Capturing the carbon dioxide: This involves preventing the release of CO_2 into the atmosphere by capturing the carbon dioxide emitted from industrial processes or by burning of fossil fuels for power generation.
- Transporting: The captured CO_2 is compressed and transferred by pipelines road tankers or ships.
- Storage/Utilisation: The CO_2 is stored several kilometres below the earth surface in geological rock formations which do not allow it to escape, it can also be stored in deep oceans where the high pressure of the water prevents CO_2 from rising to the surface. The captured CO_2 can also be utilised in Enhanced oil recovery (EOR), chemical feedstock.

A number of carbon capture technologies has been proposed and developed [15,16]. The carbon capture technologies are broadly classified into post-combustion capture, pre-

combustion capture and oxyfuel combustion [17]. Figure 2.1 shows the different carbon capture processes.

- Post-combustion process involves the capture and removal of CO_2 after the fossil fuel has been burned and the required energy is extracted. The CO_2 can be separated from the flue gas using various technologies like chemical solvents, solid absorbents, membrane separation or cryogenic separation technique. Absorption by monoethanolamine (MEA) is one of the widely-used technique. However, it reduces the energy efficiency of the plant as the regeneration of MEA requires a significant amount of heat [18]. Other techniques also incur such energy penalties.
- In the case of pre-combustion, the fossil fuel is partially oxidised in a gasifier resulting in the production of Syngas (CO and $H_{2)}$. Syngas can be directly used in combustion and the resulting CO_2 removed post-combustion or alternatively syngas can be converted into CO_2 and H_2. The CO_2 produced can be removed and pure H_2 can be used as the fuel. This method can also help capture CO_2 in some industrial processes.
- Oxyfuel combustion involves burning the fossil fuel in a stream of pure oxygen instead of air. Burning fuel in oxygen gives rise to high temperatures, to limit high temperatures cooler exhaust gases can be recirculated into the combustion chamber. This process can only be applied to fossil fuel power generation plants.

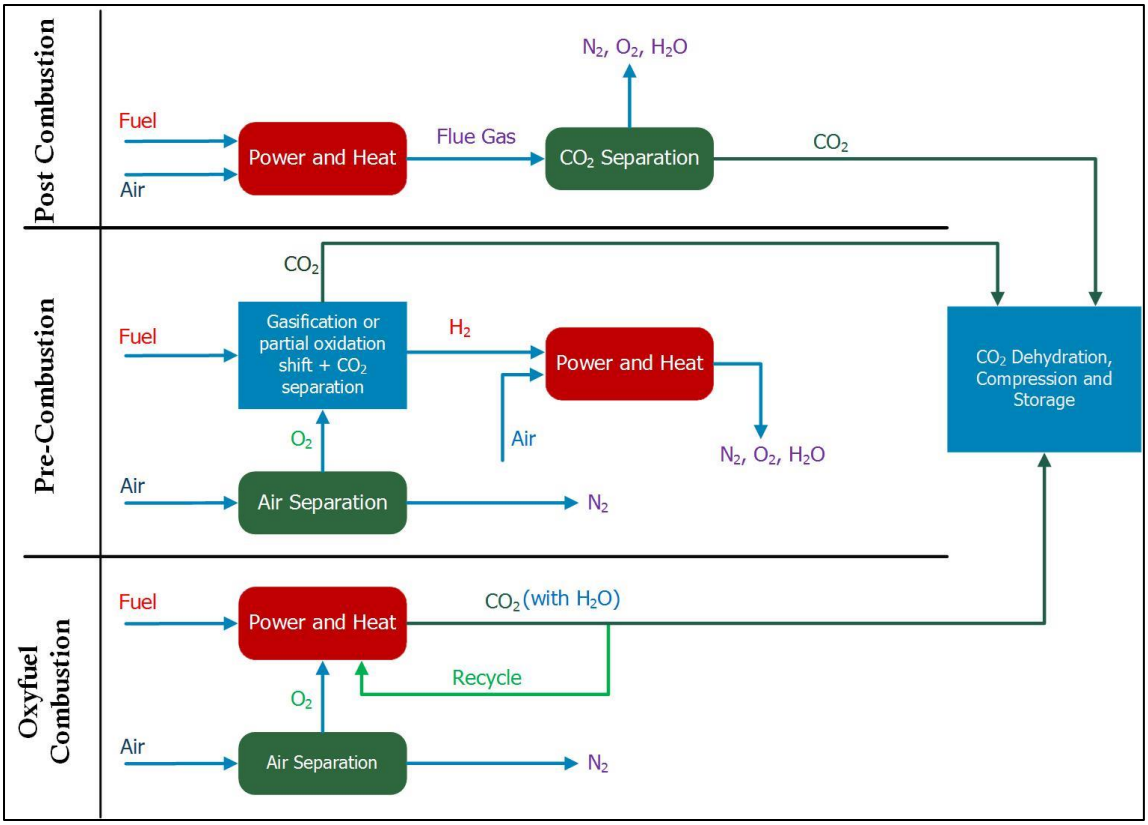

Figure 2.1: Different CCS technologies for carbon capture, reproduced from [17]

2.2 Oxyfuel Combustion

Conventional power plants use air for combustion which comprises of about 79% of nitrogen by volume due to which the concentration of CO_2 in the flue gas is diluted. Sequestration of CO_2 from such diluted mixtures is expensive economically and from the energy utilisation aspect [19,20]. In oxyfuel combustion, oxygen typically with a 95-99% purity and flue gases recycled from the exhaust of the combustor is used for combustion of the fuel. Combustion of a typical hydrocarbon in pure oxygen produces CO_2 and H_2O.

$$C_aH_b + \left(a + \frac{b}{4}\right) O_2 \rightarrow a\, CO_2 + \frac{b}{2}\, H_2O \qquad (2.1)$$

The flue gas consisting of CO_2 and H_2O can easily be sequestrated after removing H_2O or can be recirculated into the combustor with or without removing H_2O from the mixture. The recirculated flue gas can be used to control the temperature of the flame and to replace the missing volume of N_2 so that there is enough gas at the inlet for proper mixing of fuel and oxygen in a gas turbine. The recirculated flue also aids in efficiently carrying the heat through a boiler in coal powered systems. Since there is no NOx formation in oxyfuel combustion, and the CO_2 formed can be easily captured and stored it is often referred to as zero emission combustion process [21].

Most of the studies involving oxyfuel combustion technologies deal with the combustion of pulverised coal in boilers to produce exhaust gas rich in CO_2 which can be easily sequestrated. A few other studies have focussed on oxyfuel combustion using gaseous fuels in gas turbine power plants.

In 1982, Abraham proposed a coal fired process to generate CO_2 for Enhanced Oil Recovery (EOR) [22]. The literature contains many review works on the development of oxyfuel combustion technologies [17,23–27]. Figure 2.2 shows the scheme for a typical coal fired oxyfuel boiler.

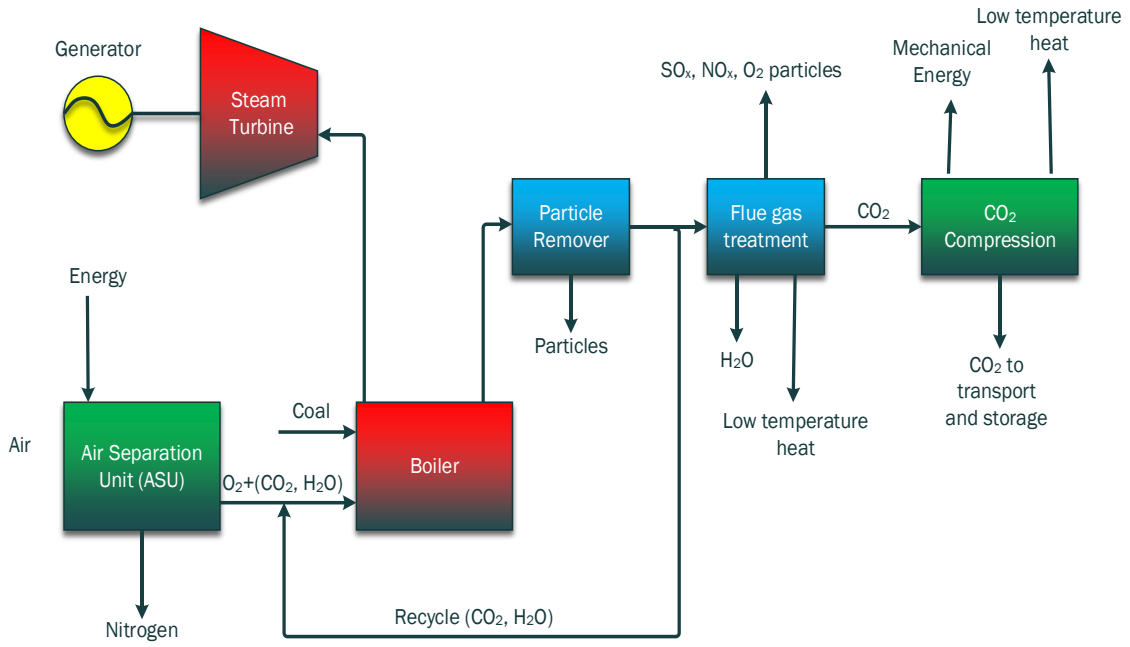

Figure 2.2: A scheme of a typical coal fired oxyfuel boiler plant, reproduced from [28].

Oxygen is firstly separated from air using air separation unit (ASU) and is then mixed with the stream of recirculated flue gas (RFG) from the boiler. Coal is burnt in an oxidizer which consists of O_2 and recirculated flue gas. The flue gas after combustion is again partially recycled into the combustor as oxidizer along with a fresh charge of O_2. The amount of CO_2 in the flue gas is increased from 17% in air to 80% when using oxyfuel. Flue gas also contains water vapour which is condensed to separate CO_2 from the mixture which is either recirculated or sequestrated. Oxyfuel combustion when coupled with CO_2 capture is an emission free technology. The pure CO_2 obtained from cooling the flue gas can be compressed and store or transported for EOR utilisation. However, the addition of ASU and sequestration of CO_2 adds to the capital and the operating cost of the plant.

Amongst the earliest pilot studies for a coal fired, oxyfuel combustion were the ones carried out by Argonne National Laboratory (ANL), International Flame Research Foundation (IFRF), IHI Japan, Air Liquide along with Babcock and Wilcox and CANMET Canada. Apart from validating the use of oxy-combustion of coal as a replacement for air fired combustors, they concluded that oxy-combustion of fuels lead to significantly lower NOx concentration per unit of energy produced [25,27].

The characteristics of oxyfuel combustion differ significantly from air-combustion in several ways which include:

- To achieve a similar adiabatic flame temperature (AFT) in oxyfuel combustion, the volume percentage of O_2 in the oxidizer is higher than the O_2 percentage in air fired combustors.
- The high percentages of H_2O and CO_2 in the combustor results in higher gas emissivity than in air.
- CO_2 and H_2O have higher heat capacities compared to nitrogen, resulting in increased heat transfer in the convection sections.
- The flue gas obtained from oxyfuel combustion has a higher density due to the presence of CO_2 with a molecular mass of 44, in comparison to the flue gas obtained after air combustion which contains mostly N_2 with a molecular mass of 28.
- Oxyfuel combustion with sequestration requires significant other units not present in the air fired plants, like flue gas compressor, Oxygen separator, sequestration unit. These units reduce the efficiency and also increase the capital and operating costs.

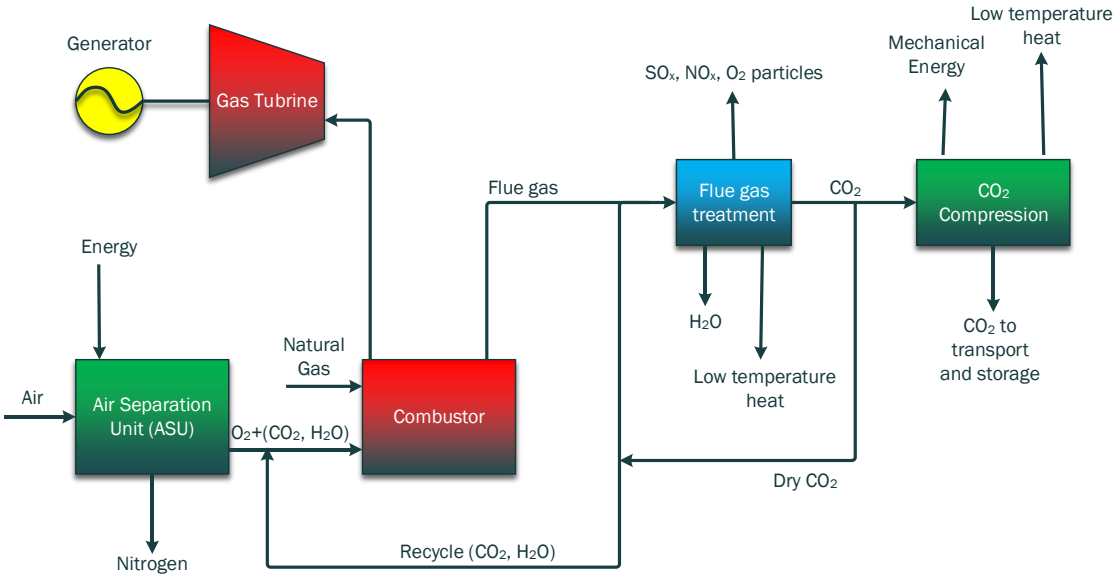

Figure 2.3: A scheme of typical natural gas fired oxyfuel combustion plant

Oxyfuel combustion in gas turbines is a relatively new avenue, started once a better understanding of coal fired oxy combustors was achieved. Figure 2.3 shows a schematic diagram of typical natural gas fired oxyfuel combustion plant. Tan et al. [29] investigated the combustion of natural gas on a down-fired vertical combustor at CANMET which was earlier used for coal combustion. The combustor was 8.3 m long, with an inner diameter of 60 cm, and had a rated capacity of 0.3 MW. The combustor was fired under oxygen enriched and O_2/CO_2 operating condition. They measured the composition of flue gas, the temperature of the flame and heat transfer profiles inside the combustor. While O_2 enriched combustion significantly increases NOx production, oxyfuel combustion of natural gas with recycled flue gas and no air leakage was found to eliminate NOx emission. Moreover, oxyfuel combustion of natural gas with recycled flue gas increased the plant efficiency due to lower gas volume and enhanced the flexibility of operation of the plant. They concluded

that the O_2/CO_2 combustion with recycled flue gas has potential to be easily retrofitted in the current air-fuel natural gas combustors.

Maier et al. carried out combustion experiment in an electrically heated 20 kW test facility with flue gas recirculation [30,31]. Oxy coal combustion was compared with air-fired combustion with different concentrations of O_2. The results showed that oxy-coal combustion with 27% O_2/73% CO_2 had higher effectiveness in NOx reduction in comparison to 23% O_2 in the oxidizer. The 23% O_2 flame was also found to be unstable.

Edge et al. [32] modelled a 500MW oxy-coal plant, with integrated CFD model for the boiler, with the aim of evaluating the potential for using oxyfuel burners to existing plant designs. They found that at 32% oxygen concentration in the oxidizer, corresponding to 70% recycling ratio, the oxyfuel combustion is able to match the air-fired steam and power output.

Ditaranto and Oppelet [33] experimentally studied radiative heat flux along the flame axis of a methane jet flame in a combustor of 350 mm diameter. The oxygen concentration of the O_2/CO_2 oxidizer was varied from 35% to 70%, along with the Reynolds number from 468-2340. As the O_2 concentration was increased the flame length observed was shorter. At 35% O_2 in the oxidizer, the heat flux distribution within the combustor was found to be similar to that of air combustion, in spite of the difference in flame temperature. The heat loss through radiation increases with increase in oxygen concentration in the oxidizer. The peak flame temperature was found to increase with the increase in O_2 concentration, and the peak temperature was found to move closer to the base of the flame.

Kim et al.[34] experimentally studied the combustion characteristics, flame length and flame structure in a non-premixed oxyfuel combustor for different oxidizer velocities and fuel nozzle diameter. The combustor wall was made of quartz glass and was 1200 mm long with 300 mm diameter. The combustor was fired an equivalence ratio of 0.98, with methane producing 0.03 MW of energy inside the combustor. The fuel and oxidizer velocities were varied to study its effect on the flame length. The flame length was found to decrease with increased fuel and oxygen velocities because of increased entrapment and turbulent mixing. The transitional Reynolds number of oxyfuel combustion was found to be higher than that of air combustion. This was attributed to the molecular viscosity of oxyfuel combustion, which was 1.2 times higher at stoichiometric condition than that of air combustion.

Krieger et al. [35] simulated a 3-D, non-premixed gas turbine combustor of 210 mm length and diameter of 74 mm with a swirler having 45° vane angle. Reynolds stress model (RSM) was used to model the turbulent flow inside the combustor, along with Discrete Ordinate (D.O) radiation model. The assumption of chemical equilibrium was used for the study to model the turbulence-chemistry interaction. Propane and Syngas were used as the fuel in the combustor along with O_2/CO_2 mixture as an oxidizer. For the case of oxy-propane combustion, the maximum temperature of the contour plot was obtained along the centre line of the combustor suggesting the flame to be present along the centre line. While the flames in the oxy-syngas combustion were V-shaped when the contour of the plane along the centre was viewed. Most stable flames were observed at 0.65 equivalence ratio. Combustion below 21% O_2 in the mixture was not possible.

Kutne et al. [36] carried out experimental studies on a partially premixed swirl stabilised oxyfuel combustor operating at atmospheric pressure. The combustor was fitted with a dual swirl burner. The study was carried out for equivalence ratios of 0.5-1, powers of 10-30kW and oxidizer consisting of 20-40% O_2. The combustor has a height of 120 mm and a cross-section of 85 × 85 mm. Like Krieger et al. [35] combustion below 22% O_2 in the oxidizer mixture of O_2/CO_2 was not possible. It was observed that equivalence ratio slightly affected the flame shape while the O_2 concentration strongly influenced the shape of the flame. The heat loss from the combustor for the oxy-methane case was found to be higher than that of air-methane combustion.

Ditaranto and Hals [37] examined combustion instabilities in sudden expansion methane oxyfuel flame. The combustion channel consisted of a square inlet section of 54 mm × 54 mm. The length of the channel was 800 mm. The fuel is allowed to premix with the oxidizer before being passed into the combustion section of the channel through a small slot.

Andersson and Johnsson experimentally studied the radiative properties of a natural gas fired O_2/CO_2 combustion using a 100 kW test unit with flue gas recycling capabilities [38–40]. A reference test of combustion in air was compared with 21% and 27 % by volume oxygen containing oxidizer, the rest being recycled flue gas consisting of CO_2. Fuel burnout was found to be delayed when 21% O_2 by volume was used in comparison to air-fired condition. The delay was caused by reduced temperature levels which itself was a result of dilution by the recycled CO_2. When 27% O_2 was used, the flame temperature and gas concentration was found to be similar to that of air-fired combustion case, but increased levels of flame radiation intensity were observed in comparison to air-fired combustion.

This behaviour was a result of increased emissivity of the gases and higher radiative contribution from flame soot.

Heil et al.[41] also demonstrated poor burnout and unstable flames with 21% O_2. However, stable flame and full burnout were observed when the O_2 % was increased to 27% and beyond.

Numerical investigations by Liu et al. [42] showed that the preheated primary oxidizer in the upstream needs a minimum of 24% oxygen by volume for a stable combustion. Nemitallah and Habib [13,43,44] investigated the effect of O_2/CO_2 ratio on the stability of a diffusion flame in a gas turbine model combustor between 0.5-0.75 equivalence ratio and observed that the stability of the flames greatly decreased when the O_2 composition is reduced below 25% and also confirmed that below 21% percentage composition mark of O_2 the combustion is highly unstable and often leads to blowout of the flame.

Seepana and Jayanti used a horizontal, swirl-stabilized combustor to investigate the stability of oxyfuel combustion of methane and liquefied petroleum gas (LPG) with air/CO_2, air/N_2 and O_2/CO_2 as oxidizer [45–48]. When using methane as the fuel and Nitrogen as diluent the critical O_2 concentration below which flame extinction occurs was found to be 15% by volume, this percentage increased to 21 when CO_2 was used as diluent. When using LPG as fuel and CO_2 as diluent the critical oxygen volume remained same as that for methane.

While a great deal of experimental and numerical studies has been carried out on oxyfuel combustion of methane, all of the studies pertain to lean combustion with excess oxygen.

Since, O_2 is an expensive commodity, which requires energy to be separated from air, it would be interesting to examine the effect of burning methane at stoichiometric conditions with oxygen.

Effect of CO_2 on combustion process:

Change of oxidizer in the combustion process not only affect the combustion dynamics of a system but also modifies its flame properties, such as adiabatic flame temperature, thermal and kinetic properties, mass and heat transport properties and radiative heat transfer. The specific heat of CO_2 (47.3 kJ/mol/k) is higher than of N_2 (30 kJ/mol/K), so the adiabatic flame temperature for mixtures with O_2/CO_2 is lower than the O_2/N_2 at same equivalence ratio and same oxygen percentage in the oxidizer mixture. In order to achieve temperatures closer to air-fuel mixtures, the oxygen concentration in oxyfuel combustion process should be around 30 percent. The laminar flame speed and transport properties of oxyfuel flames are greatly affected due to high specific heat capacity and low mass diffusivity of CO_2 in the oxidizer mixture.

Zhang et al. studied methane flame structure in a counter flow configuration and reported that CO_2 is a kinetically active species and takes part in the reaction through $CO_2 + H \leftrightarrow CO + OH$. Further, they stated that the reaction reduces the concentration of O and H radicals in the flame decreasing the burning velocity of the flame [49]. Galborg and Bentzen [50] observed that CO_2 reacts in the mixture with a methylene group to increase the amount of CO emissions. $CH_2 + CO_2 \leftrightarrow CH_2O + CO$.

2.3 Computational Fluid Dynamics of Reacting Flows (CFD)

The Numerical modelling of combustion was done using the FLUENT commercial code. The generalised equation which governs the conservation of mass, momentum and energy as well as the equation for species can be written as [51]:

$$\frac{\partial}{\partial x_j}\left(\bar{\rho}\bar{u}_j\theta + \bar{\rho}\overline{u_j'\theta'}\right) = \frac{\partial}{\partial X_j}\left(\Gamma_{\theta'}\frac{\partial \Phi}{\partial x_j}\right) + \bar{\rho}\, S_\theta \tag{2.2}$$

2.3.1 Continuity and Momentum equation

The continuity Equation is written as:

$$\frac{\partial}{\partial x_j}\left(\rho u_j\right) = 0 \tag{2.3}$$

The momentum equation is written as:

$$\frac{\partial\left(\rho u_i u_j\right)}{\partial x_j} = -\frac{\partial P}{\partial x_i} + \frac{\partial\left(\tau_{ij}\right)}{\partial x_j} \tag{2.4}$$

Where t_{ij} is the viscous stress tensor given by:

$$\tau_{ij} = \mu\left[\left(\frac{\partial u_i}{\partial x_j} + \frac{\partial u_j}{\partial x_i}\right) - \frac{2}{3}\frac{\partial u_k}{\partial x_k}\,\delta_{ij}\right] \tag{2.5}$$

Here, $\delta_{ij} = 1 \quad \text{if} \quad i = j\,, \quad \delta_{ij} = 0 \quad \text{if} \quad i \neq j$

2.3.2 Turbulence Modelling

Turbulent flows have fluctuating velocity fields. These fluctuations also affect the transport properties like the momentum, energy, and species and cause them to fluctuate as well. Turbulent flows are computationally expensive to simulate in comparison to laminar flows.

The velocity at a point in a stable, steady-state laminar flow will always be at a constant value, but as the flow becomes more unstable a transition to turbulent motion occurs. Turbulent motion is characterised by the random motion of velocity and pressure about a mean value at a point in a fluid. The nature of the fluctuations is such that even though the mean values of pressure and velocity are steady, turbulent flows are inherently time-dependent. These turbulent fluctuations mix with other transport quantities such as momentum, energy, species and cause them to fluctuate as well.

Direct Numerical solution (DNS) is the most advanced technique to simulate a turbulent flow. But it requires the distance between the grid spacing to be smaller than that of Kolmogrov scale. Even with ever so advancing computation power, the DNS technique is time consuming, especially in combustion flows [52,53] where it can take up to million CPU hours.

An alternate to DNS is the use of the Large Eddy Simulation (LES) technique. It splits the turbulent length scales so that large scales are resolved directly as in DNS, while the smaller scales are filtered and modelled. This decreases the mesh resolution required, however, the computational time is still high.

The classical approach to model turbulent flows is based on single point averages of the Navier-stokes equations. The flow governing equations are time averaged to give a modified set of equations called the Reynolds Averaged Navier-Stokes (RANS) equation.

The time averaged momentum equation is written as

$$\frac{\partial}{\partial t}(\rho u_i) + \frac{\partial}{\partial x_j}(\rho\, u_i\, u_j) = -\frac{\partial p}{\partial x_i} + \frac{\partial \tau_{ij}}{\partial x_j} + \frac{\partial}{\partial x_j}\left(-\rho\, \overline{u_i'\, u_j'}\right) \tag{2.6}$$

Where,

$$\tau_{ij} = \mu \left[\left(\frac{\partial u_i}{\partial x_j} + \frac{\partial u_j}{\partial x_i} \right) - \frac{2}{3}\, \delta_{ij}\, \frac{\partial u_k}{\partial x_k} \right] \tag{2.7}$$

Equation 2.6 is called the Reynolds averaged Navier-Stokes equation. It is similar to equation 2.4. However, additional terms representing the effects of turbulence called the Reynolds stresses, $-\rho\overline{u_i'\, u_j'}$ now appear. These terms need to be modelled in order to provide closure for the momentum equation.

A number of turbulence models are available in the literature to model the turbulent flow. However, not all turbulence model can be used for any given case. Each turbulent model has its own range of problems where it can be utilised to give a good approximation of the flow.

RNG k- ε have been used by many researchers to model swirling flows [13,54,55]. RNG k-ε model accounts for the effect of swirl on turbulence, enhancing the accuracy of swirling flows. The transport equation for turbulent kinetic energy k, using the RNG model is

$$\frac{\partial}{\partial t}(\rho k) + \frac{\partial}{\partial x_i}(\rho k u_i) = \frac{\partial}{\partial x_j}\left[\alpha_k \, \mu_{eff} \, \frac{\partial k}{\partial x_j}\right] + G_k + G_b - \rho\varepsilon \qquad (2.8)$$

$$\frac{\partial}{\partial t}(\rho\varepsilon) + \frac{\partial}{\partial x_i}(\rho\varepsilon u_i) = \frac{\partial}{\partial x_j}\left[\alpha_\varepsilon \, \mu_{eff} \, \frac{\partial \varepsilon}{\partial x_j}\right] + C_{1\varepsilon}\frac{\varepsilon}{k}\,(G_k + C_{3\varepsilon}G_b) - C_{2\varepsilon}\rho\frac{\varepsilon^2}{k} - R_\varepsilon \qquad (2.9)$$

G_k represents the generation of turbulence kinetic energy due to mean velocity gradients. G_b is the generation of turbulence kinetic energy due to buoyancy. α_k and α_ε are the inverse effective Prandtl numbers for k and ε.

The effective viscosity μ_{eff} is calculated as,

$$\mu_{eff} = \rho C_\mu \frac{k^2}{\varepsilon} \qquad (2.10)$$

Where C_μ = 0.0845, and is a constant.

The turbulence production term, G_k is defined as,

$$G_k = \mu_{eff} \, S^2 \qquad (2.11)$$

Where S is the modulus of mean rate of strain tensor,

$$S \equiv \sqrt{2 S_{ij} S_{ij}} \qquad (2.12)$$

The buoyancy term G_b for ideal gases is defined as,

$$G_b = -g_i \frac{\mu_{eff}}{Pr_t}\frac{\partial \rho}{\partial x_i} \qquad (2.13)$$

The difference between standard k-ε and RNG models lies in the additional term R_ε

$$R_\varepsilon = \frac{C_\mu \rho \eta^3 \left(1 - \frac{\eta}{\eta_0}\right) \varepsilon^2}{(1 + \beta \eta^3)\, k} \tag{2.14}$$

Where $\eta \equiv S/k\varepsilon$

The values of constants used are:

Constant	Value
α_k	1.393
α_ε	1.393
η_0	4.38
β	0.012
$C_{1\varepsilon}$	1.42
$C_{2\varepsilon}$	1.68

2.3.3 Energy Equation

The energy equation taking into account heat transfer due to conduction, species diffusion, viscous dissipation and the source term is given as [51]:

$$\frac{\partial}{\partial t}(\rho u_i h) + \frac{\partial \rho u_i h}{\partial x_i} = \frac{\partial}{\partial x_i}\left(k_f \frac{\partial T}{\partial x_i}\right) + \sum_j \frac{\partial}{\partial x_i}\left(h_j \rho D_{j,m} \left(\frac{\partial Y_j}{\partial x_i}\right)\right) + S_\phi \tag{2.15}$$

S_ϕ is the energy source term including the reaction source term and radiation heat exchange, k_f is the effective thermal conductivity, Y_j is the mass fraction of species j.

Sensible enthalpy for ideal gas

$$h = \sum_j Y_j h_j \tag{2.16}$$

Enthalpy of j^{th} species is calculated as

$$h_j = \int_{T_{ref}}^{T} c_{p,j}\, dT \tag{2.17}$$

Where T_{ref} is taken as 298.15 K. and $c_{p,j}$ is the specific heat of j^{th} species as a function of Temperature.

The heat loss from combustor wall taking into account the convection and radiation at the outer surface of the wall is given as [56]:

$$\dot{q} = h(T_w - T_a) + \varepsilon_w \sigma\,(T_w^4 - T_a^4) \tag{2.18}$$

The transfer of heat within the combustor wall due to thermal conductivity is given as:

$$\frac{\partial}{\partial x_i}\left(k_q \frac{\partial T}{\partial x_i}\right) = 0 \tag{2.19}$$

h is the effective heat transfer coefficient; T_w is the temperature on the wall; T_a is the ambient temperature

2.3.4 Species Transport Model

The species transport for j^{th} species within the combustor is modelled using the equation [57]:

$$\frac{\partial}{\partial t}\left(\rho u_i Y_j\right) + \frac{\partial \rho u_i Y_j}{\partial x_i} = \frac{\partial}{\partial x_i}\left(\rho D_{j,m} + \frac{\mu_t}{Sc_t}\right)\frac{\partial Y_j}{\partial x_i} + \frac{D_{T,i}}{T}\frac{\partial T}{\partial x_i} + R_i \qquad (2.20)$$

R_i is the source term, i.e. the net rate of production or consumption of species j by chemical reaction. $D_{j,m}$ is the mass diffusion coefficient for species j in the mixture, $D_{T,i}$ is the thermal diffusion coefficient of the i^{th} species and Sc_t is the Schmidt number defined as,

$$Sc_t = \frac{\mu_t}{\rho D_t} \qquad (2.21)$$

The overall rate of reaction of fast burning fuels is controlled by turbulent mixing. In the case of non-premixed flow, turbulence mixes fuel and oxidizer into the reaction zone, where they quickly burn. Similarly, in premixed flow turbulence mixes cold reactants and hot products into the reaction zone, where quick burning occurs. The combustion in such cases are complex and limited by mixing. The Eddy-Dissipation model based on work by Magnussen and Hjertager [58], neglects the chemical kinetic rates to model turbulence-chemistry interaction. Magnussen [59] further extended the Eddy-dissipation Model to include the detailed chemical mechanism in turbulent flows to model turbulence-chemistry interaction. The extended model is known as Eddy Dissipation Concept (EDC) model. The present work utilises the EDC model for turbulence-chemistry interaction.

The EDC is based on the assumption that reaction occurs in small turbulent structures, called the fine scales. The length fraction of fine scales is modelled as,

$$\xi^* = C_\xi \left(\frac{\nu\varepsilon}{k^2}\right)^{0.25} \tag{2.22}$$

Where * denotes fine-scale quantities, C_ξ denotes volume fraction constant which has a value of 2.1377, and ν is the kinematic viscosity.

The volume fraction of the fine scales is calculated as ξ^{*^3}. Species are assumed to in fine scale structure over time scale,

$$\tau^* = C_t \left(\frac{\nu}{\varepsilon}\right)^{0.5} \tag{2.23}$$

Where, C_t is time scale constant equal to 0.4082.

The source term in the conservation equation for the mean species i is calculated as,

$$R_i = \frac{\rho(\xi^*)^2}{\tau^* \left[1 - (\xi^*)^3\right]} \left(Y_i^* - Y_i\right) \tag{2.24}$$

Where Y_i^* is the fine-scale species mass fraction after reacting over the time τ^*.

2.3.5 Combustion Chemistry

The modelling of reacting flows numerically is a major challenge. GRI-Mech 3.0 [60] details a set of 353 reactions involving 53 species for the combustion of Natural Gas. Using these large number of reaction can make the computational time very large for a turbulent flow. Instead, a set of simplified chemical mechanism is used to reduce the computational

effort required to model the flow. Combustion is often approximated by a mixed-is-burned approximation/assumption or chemical equilibrium assumption [61].

While many simplified combustion reaction mechanisms for methane are available in the literature [62–65], very few can easily and reliably be used for oxyfuel combustion of methane. Glarborg and Bentzen [50] presented and validated a chemical mechanism for use in oxyfuel combustion scenarios. The mechanism consisted of reactions which are still computationally expensive. The mechanism has been used to modify rate parameters of other more simplified air combustion mechanism of methane, namely, the 2-step Westbrook-Dryer (WD) mechanism and the 4-step Jones-Lindstedt (JL) Mechanism. These two mechanisms are widely used for modelling combustion of methane in air and oxygen.

Andersen et al. [61] modified the rate parameters of the mechanisms and validated it using the 14-step detailed chemical kinetic model used by Galborg and Bentzen [50]. The mechanism was validated for an isothermal plug flow reactor under oxyfuel condition. The modified rate parameters significantly improve the prediction of CO concentration for WD mechanism. The modified parameters of JL mechanism improved the prediction only slightly, but nevertheless making it more accurate in predicting CO concentration.

Frassoldati et al. [66] proposed another set of improvements for the Westbrook-Dryer (WD) and Jones-Lindstedt (JL) reaction mechanism. They added the oxygen disassociation and water disassociation reaction from a previous study involving detailed chemical kinetic mechanism [67] to the JL reaction mechanism. They used experimental data from counter-flow oxyfuel diffusion flame to modify the reaction parameters of the new mechanism, to

fit the experimental data. The resulting mechanism was found to give a better prediction of temperature and species concentration. However, using this mechanism in the present study did not result in any reactions taking place. This might be because counterflow diffusion flame data was used for the parameter optimisation. The counterflow diffusion flames are generally considered to be 1-D laminar flames. However, the present study deals with turbulent flames.

Yin et al. [68] carried out a study with the original WD mechanism and the WD and JL mechanism modified for oxyfuel combustion with parameters derived from works of Andersen et al. [61] and Kim et al. [69]. They found that the modified reactions for WD and JL mechanism were able to accurately predict the temperature and emissions in an industrial furnace.

The kinetic rate of a reaction is determined by Arrhenius equation which is given as,

$$Rate\ of\ reaction = A\ T^{b}\ e^{\frac{-E_a}{RT}} \tag{2.25}$$

Where A, is called the pre-exponential factor of the reaction, T is temperature in Kelvin, b is the temperature coefficient, E_a is the activation energy for the reaction, R is the universal gas constant.

Table 2.1 and 2.2 shows the reaction mechanisms and the associated pre-exponential factor, the temperature coefficient, and the activation energy for the oxyfuel modified WD and JL mechanisms. Table 2.3 lists the reaction mechanism for H_2O and O_2 disassociation used by Frassoldati et al. [66].

Table 2.1: Modified Westbrook-Dryer mechanism (WD) [61] (units in cm, s, cal and mol)

No.	Reaction	A	b	E_a	Reaction orders
1	$CH_4 + 1.5\ O_2 \rightarrow CO + 2\ H_2O$	1.59×10^{13}	0	47.8×10^3	$[CH_4]^{0.7}\ [O_2]^{0.8}$
2	$CO + 0.5\ O_2 \rightarrow CO_2$	3.98×10^8	0	10.0×10^3	$[CO]\ [O_2]^{0.25}[H_2O]^{0.5}$
3	$CO_2 \rightarrow CO + 0.5\ O_2$	6.16×10^{13}	-0.97	78.4×10^3	$[CO_2][H_2O]^{0.25}[O_2]^{-0.25}$

Table 2.2: Modified Jones-Lindstedt mechanism (JL5) [61] (units in cm, s, cal and mol)

No.	Reaction	A	b	E_a	Reaction orders
1	$CH_4 + 0.5\ O_2 \rightarrow CO + 2\ H_2$	7.82×10^{13}	0	30.0×10^3	$[CH_4]^{0.5}\ [O_2]^{1.25}$
2	$CH_4 + H_2O \rightarrow CO + 3\ H_2$	3.00×10^{11}	0	30.0×10^3	$[CH_4]\ [O_2]$
3	$H_2 + 0.5\ O_2 \rightarrow H_2O$	1.20×10^{18}	-1	40.0×10^3	$[H_2]^{0.25}\ [O_2]^{1.5}$
4	$H_2O \rightarrow H_2 + 0.5\ O_2$	7.06×10^{17}	-0.877	97.9×10^3	$[H_2]^{-0.75}\ [O_2]\ [H_2O]$
5	$CO + H_2O \leftrightarrow CO_2 + H_2$	2.75×10^{12}	0	20.0×10^3	$[CO][H_2O]$

Table 2.3: Disassociation Reactions [66] (units in cm, s, cal and mol)

No.	Reaction	A	b	E_a	Reaction orders
1	$O_2 \leftrightarrow 2O$	1.50×10^9	0	113×10^3	$[O_2]$
2	$H_2O \leftrightarrow H + OH$	2.30×10^{22}	-3	120×10^3	$[H_2O]$

In the present study, the modified WD and JL reaction mechanism for oxyfuel combustion are used to determine the most effective one in predicting the experimental results. A JL mechanism modified by adding the disassociation reaction by Frassoldati et al. [66] was also used.

2.3.6 Radiation Model

Radiation is an important aspect of modelling combustion flows. The presence of non-luminous radiation source, specifically CO_2 and H_2O necessitates the modelling of radiation inside the combustor. The most common way to model the radiation is to use the Radiative Transfer Equation, which is derived based on "energy balance on an elementary volume taken along the direction of a pencil of rays and confined within an elementary solid angle" [70].

The radiative transfer equation (RTE) is written as [71] :

$$\frac{dI(r,s)}{ds} + (\kappa + \sigma_s)I(r,s) = \frac{\kappa n^2 \sigma T^4}{\pi} + \frac{\sigma_s}{4\pi}\int_0^{4\pi} I(r,s)\,\Phi_r(s.s')d\Omega' \qquad (2.26)$$

$I =$ radiation intensity

$\kappa =$ absorption coefficient

$\sigma_s =$ scattering coefficient

$n =$ refractive index

$r =$ the position

$\sigma =$ Stefan Boltzmann constant $= 5.669\times10^{-8}\ W/m^2 - K$

$T =$ Local temperature

$\Phi_r = \text{phase function}$

$\Omega' = \text{solid angle}$

The intensity of total radiation "I", depends upon on the position vector r and the length of the path "s". The absorption coefficient for the glass and the combustion gases are modelled differently. The radiative transfer equations can be solved by a number of ways. The approaches available in the literature to solve the RTE can be divided into four broad classifications.

1. Directional Averaging: It involves averaging of the radiance field with direction.
2. Differential Approximation: Based on first order differential approximation of the RTE.
3. Energy balance method: These are stochastic methods based on probability and statistics to solve the RTE. These methods are computationally time consuming and also large computer storage is necessary.
4. Hybrid methods: These are a mixture of directional averaging and stochastic methods for determining a finite number of directions for the RTE.

The Discrete ordinate method (DOM) has been widely used for modelling the RTE. The DOM is a directional averaging method. The method does not require any assumption regarding the directional dependence of radiation intensity. It was originally suggested by Chandrashekhar [72] for astrophysical problems. The model was further developed to be used for a variety of application [73–75]. It has been widely used in simulating radiation heat transfer in combustion flows. The DO model spans the entire range of optical thicknesses and allows to solve problems ranging from surface-to-surface radiation to

participating radiation in combustion problems. It also allows the solution of radiation at semi-transparent walls. Computational cost is moderate for typical angular discretization, and memory requirements are modest.

Modelling of radiative transfer in flames requires the knowledge of the radiation characteristic of combustion products because the accuracy and prediction of the model cannot be better than the accuracy of the characteristics used in the analysis. The combustion gases mostly consist of combustion products such as carbon dioxide (CO_2), water vapour (H_2O), carbon monoxide (CO), nitrous oxide compounds (NOx). These gases do not scatter radiation significantly but they are strong selective absorbers and emitters of radiant energy [70]. Therefore, it is important to account for the variation of radiative properties within the electromagnetic spectrum. This is done by dividing the entire wavelength spectrum into several bands and assuming that the absorption and emission characteristics of a species either remain constant or is in a functional form for a particular band. The accuracy of prediction increases as the bands become narrower, however exact results can only be obtained with line by line calculations, which require in depth analysis of discrete absorption-emission lines that are produced when there is a transition between energy levels of the gas molecule. Line by line calculations requires spectroscopic data, such as those available in databases like HITRAN or HITEMP. But they are computationally very expensive to be used for engineering applications and hence are only used as a reference to calibrate other simpler models.

Another approach is to use the Narrow Band models. Narrow Band models are based on spectral emission lines of gases by assuming a line shape. The shapes of the lines are

important as it includes the effect of temperature, pressure, optical path length on the emission and absorption characteristics. These model gives the spectral transmittance over a narrow band.

Wide band absorptivity and/or emissivity models can be defined for radiation in gaseous systems since the radiation in gaseous systems are not continuous and are concentrated in spectral bands. Such models based on wide band spectral absorption/emission characteristics based on empirical and experimental results are called wide band models. The profiles of band absorption may be triangular, box shaped or exponentially decaying function. Many wide band models are available in the literature, Edwards [76] presented a review of the available wide band models. Exponential wide band model (EWBM) is a commonly used wide band model.

Despite the simplicity involved with the narrow band and wide band models, these models can still be computationally expensive to model in practical engineering applications. Hottel and Sarofim [77] prepared an in depth database of total emittance of primary radiation participating gases CO_2 and H_2O. Hottel's chart was used for calculation of total emittance data of CO_2 and H_2O. The total emittance is based on temperature, pressure and concentration of gases. However, Hottel's chart had its own shortcomings, due to part of the chart being based on extrapolation rather than experimental measurements. Narrow Band and Wideband models are used to provide reliable data of total emittance in regions were Hottel's chart is based on extrapolation.

The spectral or band absorptivities from Narrow and Wideband models are first integrated over the entire spectrum for given pressure and temperature in order to obtain curves for

total emissivity and absorptivity. Regression techniques are then used to fit these curves to appropriate polynomials at different pressures and temperatures. The polynomials can be arranged in such a way that the resulting expression can be approximated as the sum of total emissivity or absorptivity of a clear and a number of grey gases. This method of approximation of emissivity or absorptivity is known as the "weighted sum-of-gray gases" (WSGGM). The emissivity is calculated as

$$\varepsilon = \sum_{j=0}^{J} a_{\varepsilon,j} \left(1 - e^{-\kappa_j P\, L}\right) \tag{2.27}$$

$a_{\varepsilon,j}$ is the emissivity weighting factor for the j^{th} grey gas. The weighting factors are a function of the temperature of the gas and calculated as,

$$a_{\varepsilon,j} = \sum_{k=1}^{K} b_{\varepsilon,j,k}\, T^{k-1} \tag{2.28}$$

$b_{\varepsilon,j,k}$ and κ_j are the temperature polynomial coefficients obtained by fitting total emissivity to data calculated from Narrow or Wideband models. Having j grey gases and $K-1$ polynomial order, $j(K-1)$ coefficients should be evaluated. κ_j is the absorption coefficient for the j^{th} grey gas. P is the sum of partial pressures of all the absorbing gases in the unit of [atm]. L is the path length in meters and is calculated as

$$L = 3.6\frac{V}{A_r} \tag{2.29}$$

Where, V is the total volume of the combustor and A_r is the cross-section area of the combustor.

Smith et al. [78] calculated the values of the polynomial coefficients using the Exponential Wide Band Model (EWBM) as reference. The polynomial coefficients had different values for different partial pressure of the gas.

CO_2 is added to the oxidizer to cool the system and bring down the temperature of the flue gases. Smith et al. calculated the coefficients of polynomials using EWBM, assuming 3 grey gases and 1 clear gas. However, there is uncertainty regarding the use of models like that suggested by Smith et. al. [78] for oxyfuel combustion. This is because the presence of O_2/CO_2 environment in the combustion chamber leads to significant change in the emissivities [38] and under-estimation of radiative source term [79]. The pressure path lengths in oxyfuel combustion are three to four times larger than that in an air-fired combustion due to CO_2 and H_2O accounting for 90% of the volume of flue gases in oxyfuel combustion [80]. WSGGM by Smith et al. [78] are fitted for H_2O to CO_2 ratio equal to 1 or 2.

Yin et al. [81] developed a WSGGM applicable to both air-fired and oxy-fired combustion. The parameters for the model was calculated using and EWBM as reference. They assumed 4 grey gases and 1 clear gas. The model was calibrated for H_2O/CO_2 molecular ratio (MR) of 0.125, 0.25, 0.5, 0.75, 1,2 and 4. The generated data was fitted for a temperature range of 500-3000K and 0.001-60 m path length. The model was reported to effectively improve calculations for large path lengths, however, it did not yield any significant differences from the model developed by Smith et al., for geometry with small path lengths. They

demonstrated the viability of the new model using a 0.8 MW oxyfuel combustion of methane.

Johansson et al. [80,82] modified the existing WSGGM to also account for variation in the molar ratio (MR) of CO_2 and H_2O. The effect of variation of the molar ratios was included in the calculation of polynomial coefficients. They assumed 4 grey gases and one clear gas for their model. They calculated the parameters for the model based on a Statistical Narrow Band (SNB) model which was used as reference model. They fitted the parameters of the new model in range of 500-2500K, pressure path length of 0.01-60 bar-m and MR between 0.125-2. The weights for the calculation of the emissivity is calculated as,

$$a_{\varepsilon,j} = \sum_{k=1}^{K} b_{\varepsilon,j,k} \left(\frac{T}{T_{ref}}\right)^{k-1} \tag{2.30}$$

Where, T_{ref} = 1200 K. The absorption coefficient κ, was assumed to be linearly dependent on molar ratio. But, the dependence on molar ratio of coefficient $b_{\varepsilon,j,k}$ was expressed as a second-degree polynomial function.

$$\kappa_k = K1_k + K2_k \frac{Y_{H_2O}}{Y_{CO_2}} \tag{2.31}$$

$$b_{\varepsilon,j,k} = B1_{k,j} + B2_{k,j} \frac{Y_{H_2O}}{Y_{CO_2}} + B3_{k,j} \left(\frac{Y_{H_2O}}{Y_{CO_2}}\right)^2 \tag{2.32}$$

Since then many researchers [83–85] have proposed improved versions of WSGGM based on either HITEMP or HITRAN database, for oxyfuel combustion scenarios. Rajhi et al. [86] carried out a study of different radiation models such as simple grey gas (SGG),

exponential wide band (EWBM), Leckner, Perry and Weighted sum of grey gas (WSGGM) for an industrial water tube boiler. They reported that the WSGGM using the parameters suggested by Johansson et al. is able to accurately predict the results, with a maximum error of 4% when compared to the benchmark model of the boiler. More recently, Kez et al. [87] carried out a comprehensive evaluation of different radiation models in an oxyfuel fired gas turbine combustor. Many radiation models like statistical narrow-band (SNB), statistical narrow-band correlated-k (SNBCK), wide-band correlated-k (WBCK), full spectrum correlated-k (FSCK), and WSGGM using parameters by Bordbar et al. [85] were examined. Of all the models studied the FSCK was found to be most accurate. However, FSCK models can be computationally very expensive as reported by Porter et al. [79], taking up to 16 times more time than WSGGM for a converged solution in a 3D domain. Hence, the use of WSGGM by Bordbar et al. [85] was recommended by Kez et al. [87] for use with oxyfuel combustion systems for pressure path lengths of up to 10 bar-m, as the maximum reported error was 4.18%.

In the present study validation of numerical results are carried out using parameters of WSGGM proposed by Smith et al.[78], Johansson et al. [82] and Bordbar et al. [85]. Parameters by Smith et al. [78] have been proven to be unreliable for oxyfuel combustion as mentioned in the discussion above, however, the model was included for comparative purpose.

CHAPTER 3

EXPERIMENTAL MEASUREMENTS AND ANALYSIS

3.1 Experimental Setup

Experiments were carried out to examine the impact of CO_2 addition on the stability and thermal field of oxy-CH_4 and oxy-CH_4/H_2 flames under non-premixed conditions. Experiments were carried out in a swirl stabilised model combustor at firing rates of 2.5-4.5 MW/m^3-bar. Firing rate of 3.5-20 MW/m^3-bar falls within the operating condition of typical gas turbine combustor [13]. The effect of fuel ($CH_4/H_{2)}$ and oxidizer (O_2/CO_2) compositions on the flame length scaling was also analysed. An empirical model constant for predicting the flame length is proposed. Temperature was measured to gather data for the validation of a numerical model of the gas turbine combustor. The numerical model was then used to study the effects of CO_2 dilution on oxyfuel combustion of methane.

In the current setup, methane, hydrogen, oxygen and CO_2 is supplied from compressed gas cylinders of 99.9% purity. Gas flow is regulated using mass flow controllers having ±0.5% uncertainty, manufactured by Bronkhorest HIGH-TECH. Methane and hydrogen are mixed in a mixing chamber before being supplied for combustion. The fuels are transported via a stainless-steel tube of 6.35 mm diameter. At the inlet to the combustor, where the fuel pipe terminates the fuel is supplied through fuel nozzle into the combustion chamber. Flame pictures were taken using a Nikon D5200 camera to study the flame height and flame structure. A schematic diagram of the experimental setup for a non-premixed model gas turbine combustor is as shown in Figure 3.1.

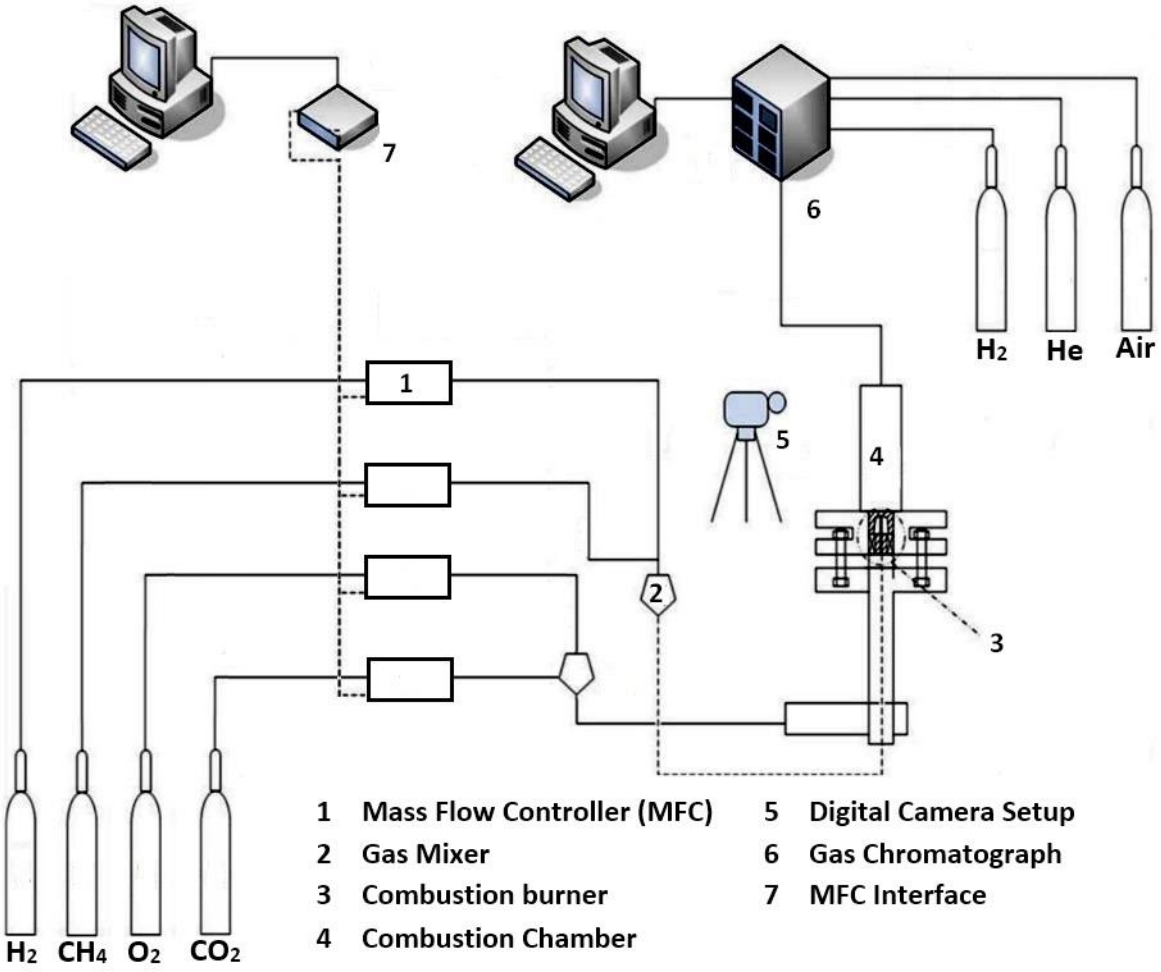

Figure 3.1: Schematic Diagram of Experimental Setup

Figure 3.2 shows the plan view of the fuel nozzle. It consists of 16 channels that are made on a bluff body of diameter 4.25 mm. The bluff body is inserted into the fuel pipe to form the nozzle, so as to increase the velocity of fuel, for flame stabilisation. Each channel is 0.45 mm × 0.2 mm in dimensions.

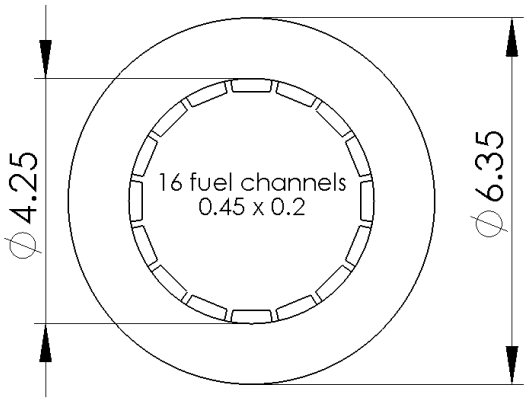

Figure 3.2: Plan view of fuel nozzle (dimensions in mm)

The oxygen is supplied using four 6.35 mm diameter tubes which are evenly distributed around a larger pipe of 50.8 mm diameter, 1.2 metres upstream of the swirler. The swirler has a diameter of 53 mm, height of 20 mm with a centre-body of 25 mm. The centre-body has a hole of 7 mm to allow for the fuel pipe to pass through it. The swirler has 8 vanes inclined at 45 degrees to the normal flow direction. The swirler generates a swirling flow which is then passed through an annular space between the fuel inlet pipe and an outside diffuser.

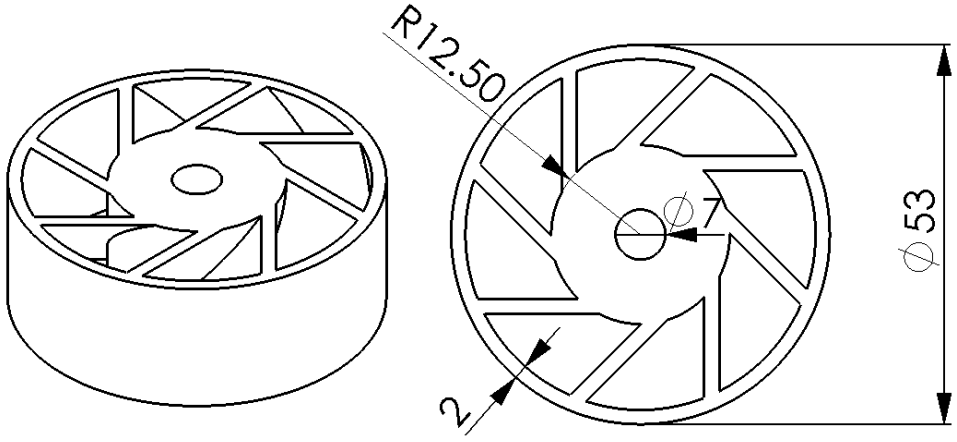

Figure 3.3: Sketch of 45° Swirler

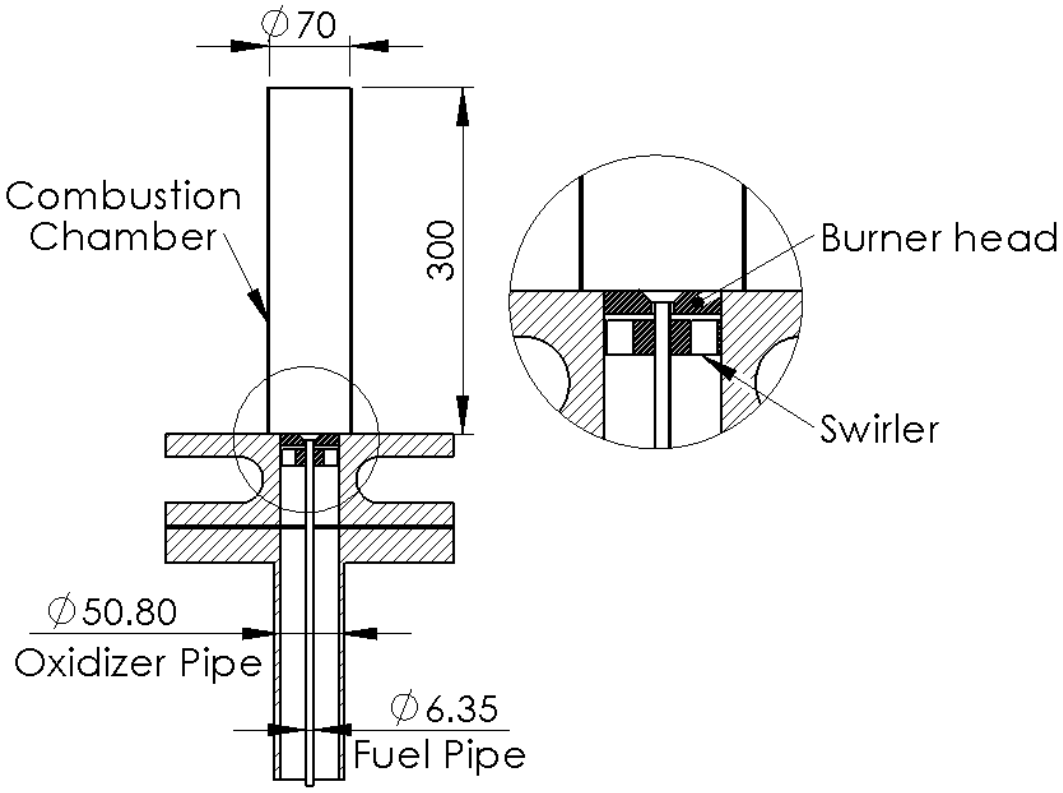

Figure 3.4: Cross-section of the combustor (dimensions in mm)

The diffuser has an inlet diameter of 10 mm and an outlet diameter of 20 mm. The thickness of the diffuser is 5mm. The exit plane of the diffuser also contains the fuel nozzle. The oxidizer and fuel enter a quartz glass combustion chamber of 70 mm diameter and 300 mm height. The combustion chamber is open to the atmosphere and all the combustion takes place at atmospheric condition.

3.2 Experimental Procedure

Oxy-combustion experiments of pure methane (0% H_2) were initially carried out to study the flame stability and combustor thermal field under non-premixed conditions and at different CO_2 concentrations in the oxidizer mixture. Experiments were, thereafter, carried

out at combustor firing rates ranging from 2.5 - 4.5 MW/m^3-bar and hydrogen contents of 10% H_2 and 20% H_2 in the fuel mixture. Flame pictures were taken using a Nikon D5200 camera to study the flame height and flame structure. The flame length at different operating conditions was, thereafter, obtained using a MATLAB custom code.

The stoichiometric combustion equation for pure oxyfuel combustion is written as

$$CH_4 + 2\,O_2 \rightarrow CO_2 + 2H_2O \tag{3.1}$$

When CO_2 is introduced as diluent along with Oxygen in the oxidizer stream the above equation can be written as,

$$CH_4 + 2\,[\,O_2 + (CP)\,CO_2] \rightarrow (1 + 2\,CP)\,CO_2 + 2H_2O \tag{3.2}$$

Where CP is calculated as

$$CP = \frac{\%\,CO_2}{1 - \%\,CO_2}\,\dot{V}_{O_2} \tag{3.3}$$

% CO_2 is the percentage volume of CO_2 in the oxidizer stream, $\dot{V}_{O_2}$ is the volume of O_2 required for stoichiometric combustion of methane.

The global equivalence ratio is calculated as,

$$\phi = \frac{\left(\frac{F}{O}\right)_{actual}}{\left(\frac{F}{O}\right)_{stoichiometric}} \tag{3.4}$$

CO_2 is treated as a diluent, and thus not included when calculating the global equivalence ratio of the combustor. Thus, the fuel to oxidizer ratio on mass basis is calculated as,

$$\frac{F}{O} = \frac{16}{2\times(1+Z)\times 32} \tag{3.5}$$

Where Z is the fraction of excess O_2 that might be present in the oxidizer mixture.

Table 3.1 shows the operating condition for various CO_2 composition in the oxidizer for 0% H_2 and 20% H_2 at 4 MW/m^3-bar

Table 3.1: Operating conditions at 0% H_2 and 20% H_2 for firing rate of 4 MW/m^3-bar

0% H_2				**20%** H_2				
% CO_2 in oxidizer mixture	Volume of CH_4 (lit/min)	Volume of O_2 (lit/min)	Volume of CO_2 (lit/min)	% CO_2 in oxidizer mixture	Volume of CH_4 (lit/min)	Volume of H_2 (lit/min)	Volume of O_2 (lit/min)	Volume of CO_2 (lit/min)
0	8.48	16.96	0	0	7.88	1.97	16.75	0
6	8.48	16.96	1.08	6	7.88	1.97	16.75	1.08
12	8.48	16.96	2.31	12	7.88	1.97	16.75	2.31
19	8.48	16.96	3.98	19	7.88	1.97	16.75	3.98
27	8.48	16.96	6.27	27	7.88	1.97	16.75	6.27
35	8.48	16.96	9.13	35	7.88	1.97	16.75	9.13
55[1]	8.48	16.96	20.72	41.8[1]	7.88	1.97	16.75	36.03
74[2]	8.48	16.96	48.27	82.3[2]	7.88	1.97	16.75	78.85

Temperature profiling near the exhaust was carried out using a B-type thermocouple from Omega instruments with measuring range of up to 1993K and accuracy of ± 0.5%. The temperature will be measured at different heights from the inlet plane of the combustor. Temperature data acquisition card from NI instruments in conjunction with LabVIEW software will be used to obtain readings from the B-type thermocouple.

To obtain the flame transition points, CO_2 sweep test was carried out. This was achieved by gradually increasing the CO_2 concentration in the oxidizer mixture by 1 % until flame transition occurs. The CO_2 sweep test was repeated three times for each test condition and the average transition point is reported. It is important to state that the maximum change in the observed transition point is 1 % (1 step). This change could be due to bulk changes in the room condition and/or uncertainty in the mass flow controller. All experiments were carried out at ambient temperature and pressure.

Following which fuel composition was altered while keeping the energy level fixed. The fuel composition was varied by introducing hydrogen into the fuel mixture. Hydrogen was varied between 0-20 % with steps of 10 %. For validation of the numerical model, temperatures obtained radially near the exit of the combustor was used to validate the numerical model.

3.3 Experimental Results and Discussion

In this section, the results pertaining to the experiments carried out with the non-premixed combustor in oxyfuel environment is presented.

Figure 3.5 shows the visible flame images for oxyfuel combustion of methane and hydrogen enriched methane for a swirl stabilised flame, for a combustor operating at 4 MW/m^3-bar energy level. On the x-axis, the percentage of CO_2 is varied while on the y-axis percentage of H_2 is varied.

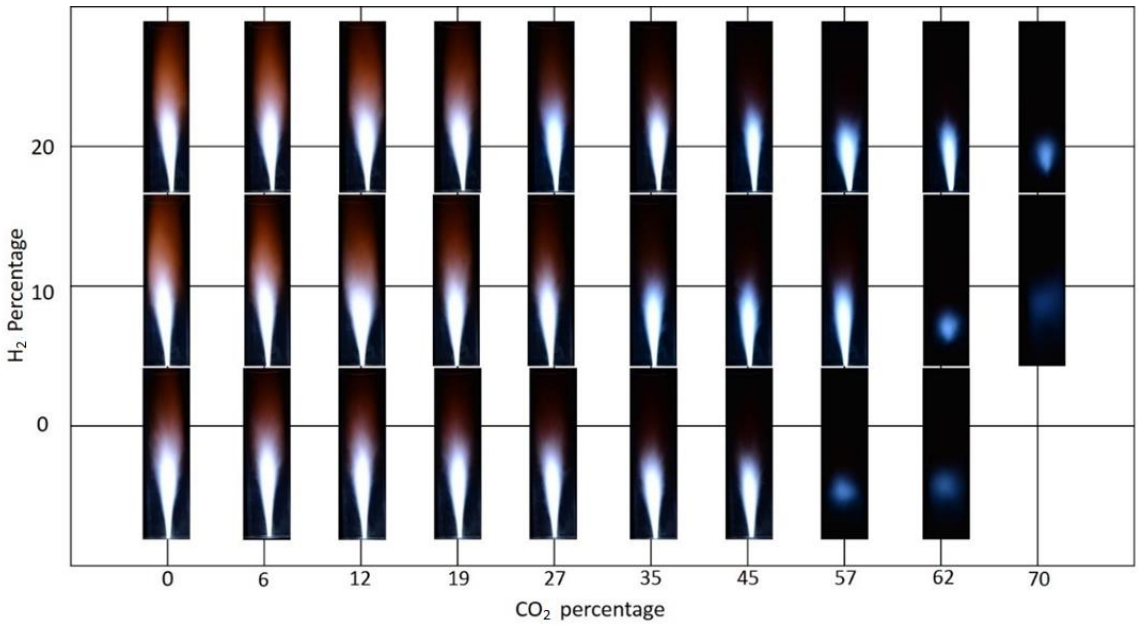

Figure 3.5: Flame images for different oxidizer (O_2/CO_2) mixtures and fuel compositions at a firing rate of 4 MW/m^3-bar

It can be seen that for low CO_2% in the CO_2/O_2 oxidizer mixture, the flame is attached to the fuel nozzle, this can be called as Attached flame. As the CO_2 percentage in the oxidizer is increased the flame lifts away from the fuel nozzle and stabilises at a distance away from the fuel nozzle, also referred to as lifted flame. As more CO_2 is added to the oxidizer the flame extinguishes, as there is no visible flame. So, the flame transits through the following regime: Attached flame → Lifted flame → No flame. For the case of pure oxyfuel methane combustion (100% CH_4 and 100% O_2), a long flame with reddish plume is observed near the exit of the combustor. The reddish plume suggests the presence of unburned hydrocarbon and formation of pollutants such as soot, implying incomplete combustion. As CO_2 is added to the oxidizer the flame length can be observed to decrease with increase in CO_2, and so does the intensity of the reddish plume. The addition of CO_2 increases the mass flow rate of the oxidizer, increasing the flow velocity of the oxidizer.

3.3.1 Flame Transition Regime

Figure 3.6 shows the stability map for oxyfuel combustion of methane at different firing rates (different mass flow rate of fuel). Transition points of the oxy-methane flame at stoichiometry are reported in the figure. The transition points were obtained by increasing the amount of CO_2 in the O_2/CO_2 oxidizer mixture. It can be seen that, at firing rates of 2.5 and 3 MW/m^3-bar, the flame transits from attached flame regime to no flame regime directly. Whereas, for firing rates greater than 3 MW/m^3-bar the flame first detaches from the fuel nozzle and stabilises at some distance away from the fuel nozzle before going completely extinct. In other words, the flame moves from the attached regime to the lifted flame regime before transitioning to the no flame regime. Typical industrial gas turbine combustors work in the firing range of 3.5-20 MW/m^3-bar [13].

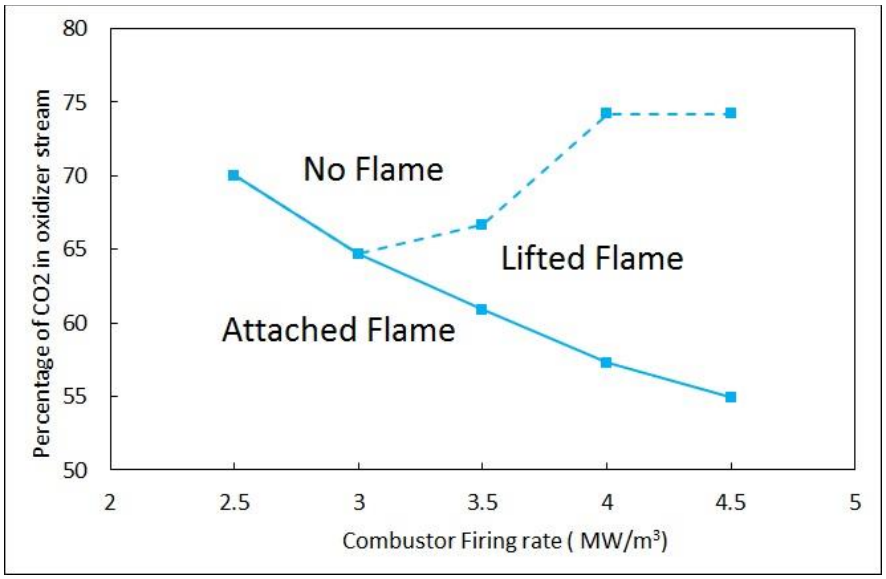

Figure 3.6: Flame stability map at different firing rate for 0% H_2. Dashed line: Lifted flame → No flame transition border

From the figure, it can also be seen that as the firing rates are increased less amount of CO_2 is needed for the flame to transit from the attached regime to the lifted regime. However,

for the flame to transit to the no flame regime a higher amount of CO_2 is needed, as the firing rate of the combustor is increased. Therefore, at a higher firing rate large amount of CO_2 is required in the oxidizer mixture before the flame can go extinct.

A similar trend is observed when H_2 is added to the fuel. Figure 3.7 shows the flame stability map at different firing rates for flames with 100% CH_4 and 80/20 CH_4/H_2 as fuel. H_2 has been reported to have higher laminar flame speeds, lower ignition energy, wide flammability limit and higher resistance to strain in comparison to methane [88–90].

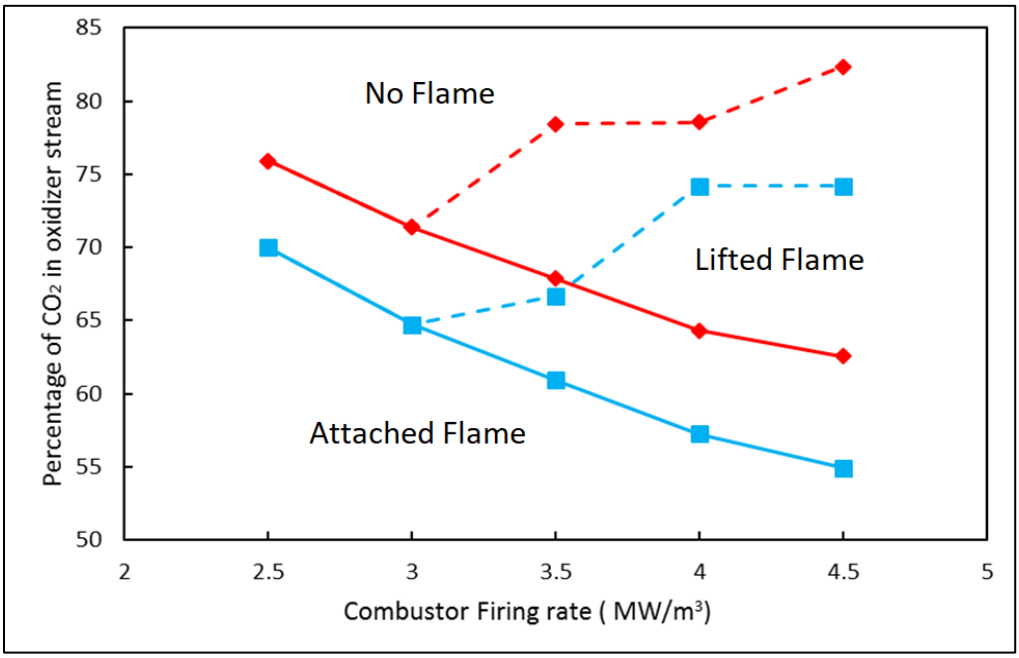

Figure 3.7: Flame stability map at different firing rate; ■ 0 % H_2: ◆ 20 % H_2. Dashed line: Lifted flame →No flame transition border

The addition of H_2 in the fuel shifts the stability map for pure methane oxyfuel combustion to a region of higher CO_2. The addition of H_2 to the fuel mixture increases the amount of CO_2 required for the flame transition to the lifted flame region as well as to the no flame region. Thus, more CO_2 can be added to the combustor making hydrogen enriched methane oxyfuel combustion more stable than methane oxyfuel combustion.

With the increase of combustor firing rate, the local flame temperature is expected to increase, extending the transition of the flame from the attached regime to the lifted regime. However, in the experimentation, a reverse trend was found to be true. At higher firing rates, the flame required less CO_2 to transition from attached regime to the lifted regime. By increasing the firing rate, the amount of fuel supplied is increased, which increases the turbulence at near the fuel nozzle. This increase in turbulence at the fuel nozzle increases the entrainment of oxidizer (containing CO_2) into the fuel stream. CO_2 has been reported to decrease the reactivity of the flame [91]. Thus, the increased entrainment of CO_2 present in the oxidizer, with increase of firing rate reduces the methane burning rate near the fuel nozzle. Weak flames with low strain resistance at the nozzle were found to precede the transition of the flame from the attached regime to lifted regime. While the flames characterised with weak flame near the fuel nozzle under high flow strain (high fuel velocity) transits from attached flame regime to lifted flame regime at lower CO_2 composition in the oxidizer.

A nearly constant oxidizer velocity (U_{ox}) for the transition of the flame from the attached regime to the lifted regime was observed, suggesting the existence of a critical velocity for such transitions from attached flame regime to the lifted flame regime. At this critical velocity, the rate of flow strain imposed on the flame in the vicinity of the nozzle is more than the strain the flame can resist (extinction strain rate), this results in the local flame extinction at the fuel nozzle leading to the stabilisation of the flame at a distance from the nozzle. Um et.al. [92] have earlier reported that the lifted flame occurs when the local strain rates are too high to match the local burning velocity. Ghafour et al. [93], identified the imbalance in the flow time scale $\left(\frac{U}{\delta}\right)$ and chemical time scale $\left(\frac{S_L}{\alpha}\right)$ as the main cause of

the flame transition. The experimental observation suggests that the transition from attached flame regime to the lifted flame regime strongly depends on the flame strain resistance such that fuel composition that produces flames with higher strain resistance will similarly have higher critical U_{ox}. This implies that the critical oxidizer velocity at which the flame transition occurs will increase with increasing hydrogen contents in the fuel mixture. The critical velocity for 0% H_2 and 20% H_2 is 20.43 m/s ± 5% and 25.58 m/s ± 4%, respectively.

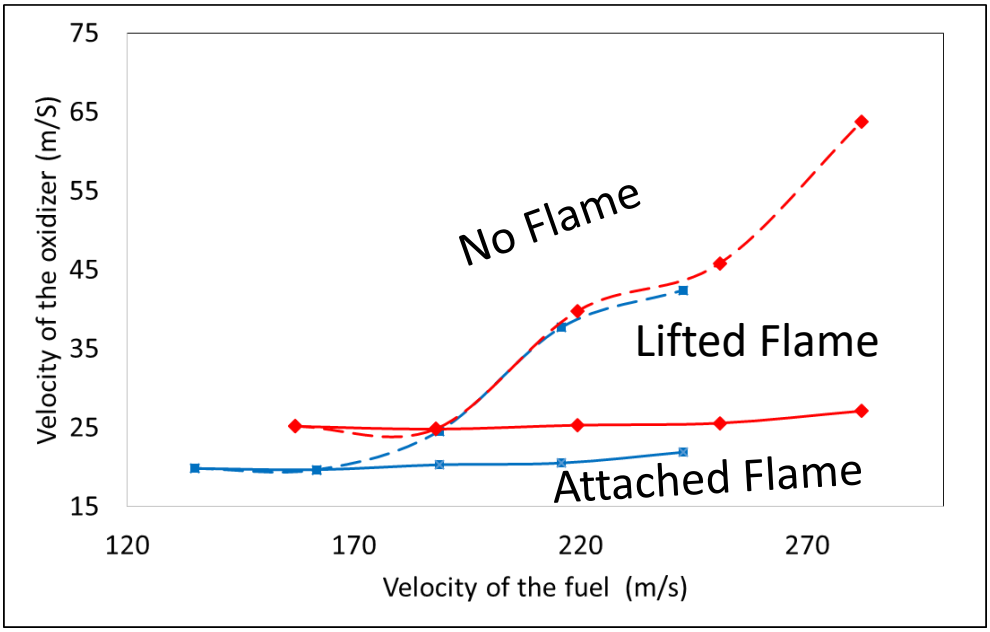

Figure 3.8: Velocities of the fuel and oxidizer at the transition points; ■ 0 %H_2: ◆ 20 %H_2. Dashed line: Lifted flame →No flame transition border

With the increase of local temperature in the combustor when the firing rate is increased, the flame burning velocity and its resistance to extinction is also increased. Thus, more amount of CO_2 can be added to the oxidizer mixture before the flame can go extinct. This observation is evident from Figure 3.8. As H_2 is added to the fuel mixture, the flame burning speed and resistance to extinction strain is further increased [88–90]. The addition

of H_2 has a stronger effect in delaying the transition point of the flame from the lifted regime to the no flame regime. For example, increasing the firing rate from 3.5 MW/m^3-bar to 4.5 MW/m^3-bar (about 29% increase) increases the U_{ox} by about 7% while increasing the hydrogen content in the fuel mixture by 20% increases the U_{ox} by about 24%.

The effect of combustor firing was isolated to study the effect of hydrogen enrichment of methane on the flame stability, as shown in Figure 3.9. The transition point for lifted and no flame from attached flame regime increases by 7% and 4 % respectively, when 20 % H_2 is added to the CH_4-H_2 fuel mixture in comparison to pure methane combustion. With the addition of 0% H_2 the fuel flow velocity is also increased by 16% due to the lower density of H_2 than CH_4. This implies that the increased flow strain imposed on flame by the increase in fuel flow velocity could be responsible for marginal extension limit observed.

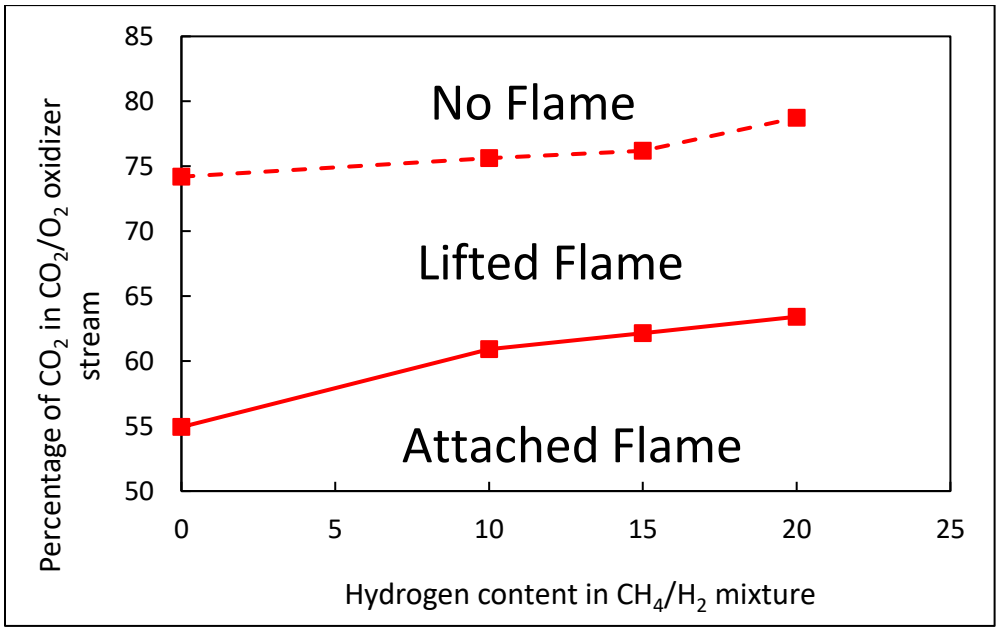

Figure 3.9: Flame stability map at different H_2 composition in the fuel mixture; Firing rate 4 MW/m^3-bar.

3.3.2 Stability of lifted non-premixed flame

Figure 3.10 shows sequential images of the flame near the lift-off point. As stated earlier, weaker flames at the base (Flame. II - V) were observed to precede the flame lift-off (Flame VI). The weak flame at the base indicates a reduction in the chemical activity leading to local flame extinction at the flame base (Flame V) and eventual flame lift off (Flame. VI).

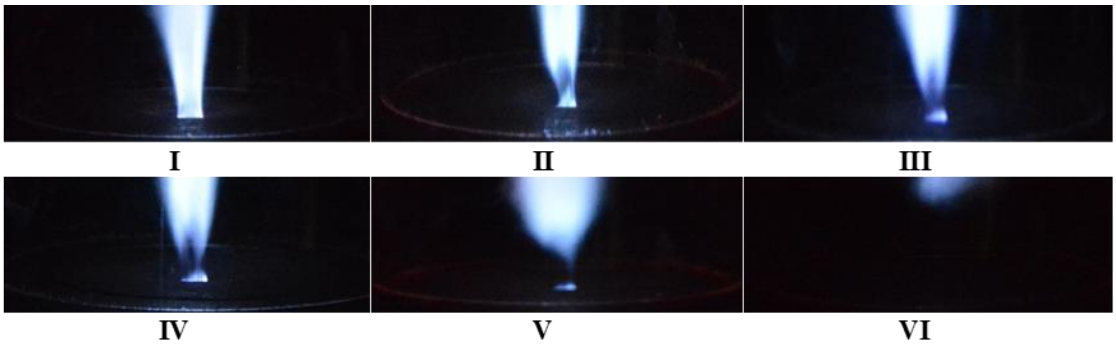

Figure 3.10: Sequential images of the flame base close to lift-off point for 0 % H_2 and different CO_2 composition in oxidizer (O_2/CO_2) mixtures; (I): 64% CO_2, (II): 65% CO_2, (III): 66% CO_2, (IV): 67% CO_2, (V): 68% CO_2, (VI): 69% CO_2

A previous Numerical study by Briones et al. [91] has similarly shown that the addition of diluent reduces the chemical activity due to a reduced temperature at the base of the flame. They concluded that the reduced temperature at the flame base is due to their observed H-atom destruction rate (i.e. reaction rate) that leads to local flame extinction and flame lift-off. Different theories have been advanced to explain the stability of a lifted non-premixed flame and summarised in [94]: Premixed Flame Theory [94], The Edge-Flame Concept [95], and The Critical Scalar Dissipation Concept [96]. In The Premixed Flame Theory, the base of a non-premixed flame is premixed [94] and burns locally at a burning velocity that stabilises the flame. The Edge-Flame Concept [95], however, claims that the leading

edge of the flame is partially premixed and propagates upstream to counter the effect of the flow field. The Critical Scalar Dissipation Concept [96] suggests that lifted flames are stabilised at a location where Scalar Dissipation rate is lower than a critical value. The Edge-Flame Concept and Scalar Dissipation Concept were collapsed in Takahashi and Katta [97] theory that suggests that lifted flame stabilisation is due to a dynamic balance in the scalar dissipation rate and characteristic reaction rate. This theory was reported to be consistent with their numerical observations. In the present study, it was observed that the leading edge of the lifted flame oscillates to and fro at different points within the combustor indicating that the stabilisation points are the points where the edge flame speed balances the local flow velocity. This is in agreement with the Takahashi and Katta [97] theory since the edge flame speed is a function of the scalar dissipation rate. The unsteady nature of the flow-flame interaction will change the distribution of the scalar dissipation rate within the combustor and the lifted flame stabilisation points. It can be concluded that the flame stabilisation location is not fixed in a turbulent non-premixed flame as the flame leading edge will continue to identify locations with lowest scalar dissipation to stabilise.

3.3.3 Flame length

In this section, we discuss the variation of the flame length with changes in the oxidizer and fuel compositions. For each operating condition, about 10 flame images were averaged based on which the flame length was obtained using custom MATLAB code. The flame length was, thereafter, normalised with the effective fuel nozzle diameter and is presented in Figure 3.11.

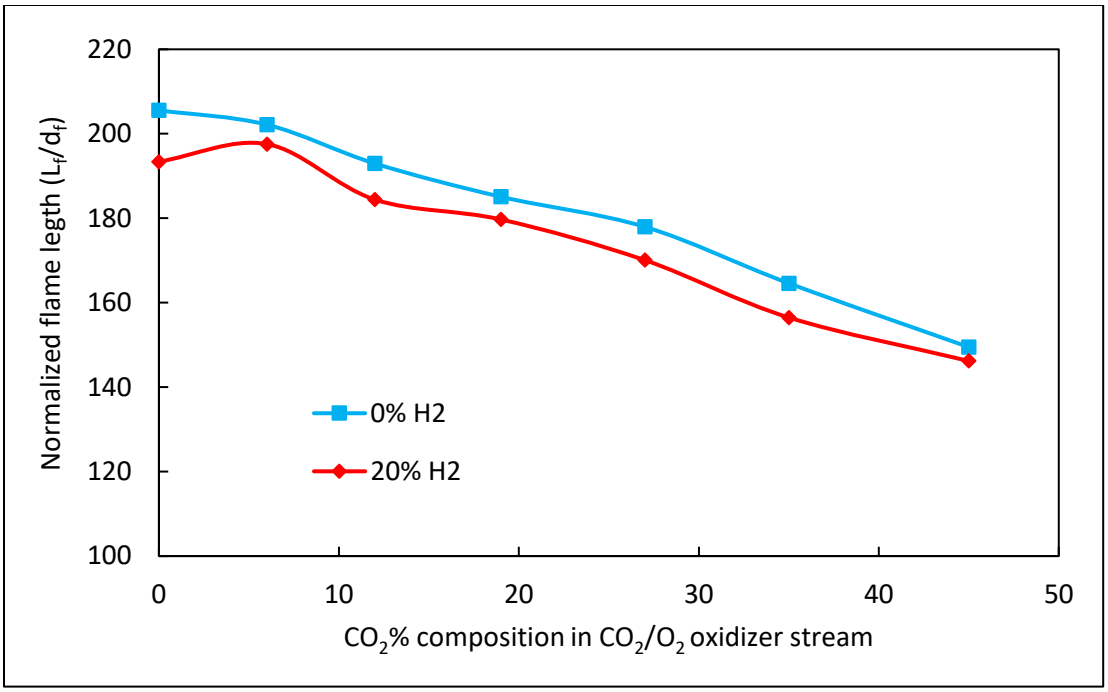

Figure 3.11: Normalised flame length for different oxidizer (O_2/CO_2) mixtures and fuel compositions at a firing rate of 4 MW/m^3-bar.

Previous studies have shown that the rate of flame propagation and density change in the flame surface are factors that affect the flame surface area [98]. It can be seen that increasing the CO_2 composition in the oxidizer alters the flame propagation rate and leads to a decreased normalised flame length. Reasons for the observed decrease in the flame length were discussed earlier and can be summarised as:

(1) Increasing the CO_2 content increases the oxidizer Reynolds number and, thereby, increases the turbulence level in the combustor. This improves the oxidizer-fuel mixing and increases the burning intensity of the flame, thus, making the flame to become compact as observed in Figure 3.5.

(2) The addition of CO_2 causes convection and radiation of heat away from the reaction zone. High heat transfer rates from the reaction zone could reduce the flame propagation rate and further contribute to decreased flame length.

(3) The addition of CO_2 lowers the molecular diffusivity of O_2 to the fuel stream, thus, affecting the rate of flame propagation.

(4) The chain branching reaction is suppressed by the addition of CO_2 leading to flame extinction even at higher flame temperature [99].

Also from Figure 3.11, the flame length for pure methane was observed to be marginally longer than those of hydrogen enriched flame. Similar observations were reported by Choudhuri et al. [100] for increasing concentration of H_2 in H_2 –Natural gas fuel mixture. They suggest that fuel mixture containing hydrogen burns faster resulting in lower residence and convective time scale. This implies that fuel containing hydrogen will burn (faster) over a shorter distance, thereby, shortening the flame length. The addition of hydrogen was also reported to increase the radical pool of OH and H that increases the rate of combustion and reduces the flame length [93]. The flame length was observed to decrease by about 4% with the addition of 20% H_2. This is comparable with the 12% flame length reduction when the hydrogen percentage in the natural gas- air flame is increased from 0 % to 50% [26].

3.3.4 Empirical model of the flame length

In the results presented in Figure 3.11, the flame length was normalised with the nominal diameter of the fuel jet. The procedures for computing the effective diameter using the Near-field and Far-field concept can be found in work of Oh et al.[101]. The normalised

flame length obtained using this approach is the characteristics length of the flame that will conceptually allow the same mass and momentum flux as the actual [101].

In the Near-field concept, the effective mixture density(ρ_{eff}) is assumed to be dependent on the fuel density (ρ_F), the effective nozzle diameter for the Near-field is given as[102]:

$$d_{eff} = d_F \left(\frac{\rho_F}{\rho_{eff}}\right)^{1/2} \tag{3.6}$$

While in the Far-field concept, the effective mixture density (ρ_{eff}) is assumed to be dependent on the density of the ambient air (ρ_A) and the effective nozzle density for the Far-field concept is calculated as [102]:

$$d_{eff} = d_F \left(\frac{\rho_{eff}}{\rho_A}\right)^{1/2} \tag{3.7}$$

The effective density is computed as given in Eq. (3.8):

$$\rho_{eff} = \frac{\rho_F . u_F^2 . A_F + \rho_A . u_A^2 . A_A}{u_F^2 . A_F + u_A^2 . A_A} \tag{3.8}$$

The calculated effective nozzle diameter using the Near-field and Far-field concept is then used to normalise the experimental flame length as:

$$L_{n,m} = \frac{L}{d_{eff}} \tag{3.9}$$

Where L is the measured flame length, $L_{n,m}$ is the normalised measured flame length.

These are compared to those obtained using the nominal diameter of the nozzle as presented in Figure 3.12 and as explained hereunder.

In modelling the flame length, Chen et al.[103] proposed an empirical model for predicting the flame length. Analysis by Dahm et al.[104] results in a similar model as given in Eq. (3.10). The model is developed to predict the flame length based on nominal nozzle diameter. The empirical normalised flame length (L_{n,e_1}) is computed as:

$$L_{n,e_1} = \frac{C.(1+f_s)\left(\frac{\rho_F}{\rho_A}\right)^{1/2}}{\left(1+\frac{\rho_A.u_A^2(d_A^2-(d_F+t_F)^2)}{\rho_F.u_F^2.d_F^2}\right)^{1/2}} \tag{3.10}$$

Kim et al. [105] also reported a theoretical model that predicts the flame length based on the Near-field The normalised flame length based on the Near-field concept (L_{n,e_2})is:

$$L_{n,e_2} = C.(1+f_s)\left(\frac{1+\left(\frac{u_A}{u_F}\right)^2.\frac{(d_F+t_F)^2}{d_F^2}}{1+\frac{\rho_A}{\rho_F}.\left(\frac{u_A}{u_F}\right)^2.\frac{(d_F+t_F)^2}{d_F^2}}\right)^{1/2} \tag{3.11}$$

The normalised flame length based on the Far-field concept (L_{n,e_3}) is:

$$L_{n,e_3} = C.(1+f_s)\left(\frac{\rho_F}{\rho_A}\right)^{1/2}\left(\frac{1+\frac{\rho_A}{\rho_F}.\left(\frac{u_A}{u_F}\right)^2.\frac{(d_F+t_F)^2}{d_F^2}}{1+\left(\frac{u_A}{u_F}\right)^2.\frac{(d_F+t_F)^2}{d_F^2}}\right)^{1/2} \tag{3.12}$$

One of the drawbacks in the above flame length models is the arbitrary constant C given in the models and which varies in all the models and changes with changes in fuel composition. In the present study, we suggest that that the constant C can be calculated as:

$$C = \left(\frac{\rho_{O_2}}{\rho_f n_{O_2}}\right)^2\left(\frac{u_F d_{ox}}{\alpha_F}\right)^{1/2} \tag{3.13}$$

By incorporating the obtained C in Eq. (3.10-3.12) the model equations can be re-written as:

For Chen et. al. [103]:

$$L_{n,e_1} = \left(\frac{\rho_{O_2}}{\rho_f n_{O_2}}\right)^2 \left(\frac{u_F d_{ox}}{\alpha_F}\right)^{1/2} . \frac{(1+f_s)\left(\frac{\rho_F}{\rho_A}\right)^{1/2}}{\left(1+\frac{\rho_A . u_A^2 (d_A^2 - (d_F+t_F)^2)}{\rho_F . u_F^2 . d_F^2}\right)^{1/2}} \quad (3.14)$$

For Near-field concept [105] :

$$L_{n,e_2} = \left(\frac{\rho_{O_2}}{\rho_f n_{O_2}}\right)^2 \left(\frac{u_F d_{ox}}{\alpha_F}\right)^{1/2} . (1+f_s) \left(\frac{1+\left(\frac{u_A}{u_F}\right)^2 . \frac{(d_F+t_F)^2}{d_F^2}}{1+\frac{\rho_A}{\rho_F} . \left(\frac{u_A}{u_F}\right)^2 . \frac{(d_F+t_F)^2}{d_F^2}}\right)^{1/2} \quad (3.15)$$

For Far-field concept [105]:

$$L_{n,e_3} = (1+f_s)\left(\frac{\rho_F}{\rho_A}\right)^{1/2} . \left(\frac{\rho_{O_2}}{\rho_f n_{O_2}}\right)^2 \left(\frac{u_F d_{ox}}{\alpha_F}\right)^{1/2} . \left(\frac{1+\frac{\rho_A}{\rho_F} . \left(\frac{u_A}{u_F}\right)^2 . \frac{(d_F+t_F)^2}{d_F^2}}{1+\left(\frac{u_A}{u_F}\right)^2 . \frac{(d_F+t_F)^2}{d_F^2}}\right)^{1/2} \quad (3.16)$$

These equations (Eqs. 3.14-3.16) are then used to predict the flame lengths. The predicted flame lengths are compared to the normalised experimentally measured flame lengths as shown in Figure 3.12. For both cases of 0% H_2 and 20 % H_2, all the models captured the trend of the normalised flame length. The Far-field, however, over-predicts the flame length while the model by Chen [103] under-predicts the flame length. The predicted flame length based on the Near-field concept gave good fit of the experimentally measured flame length. This is in agreement with Kim et al. [105] who have also reported that the Near-field model fitted their experimental measured data.

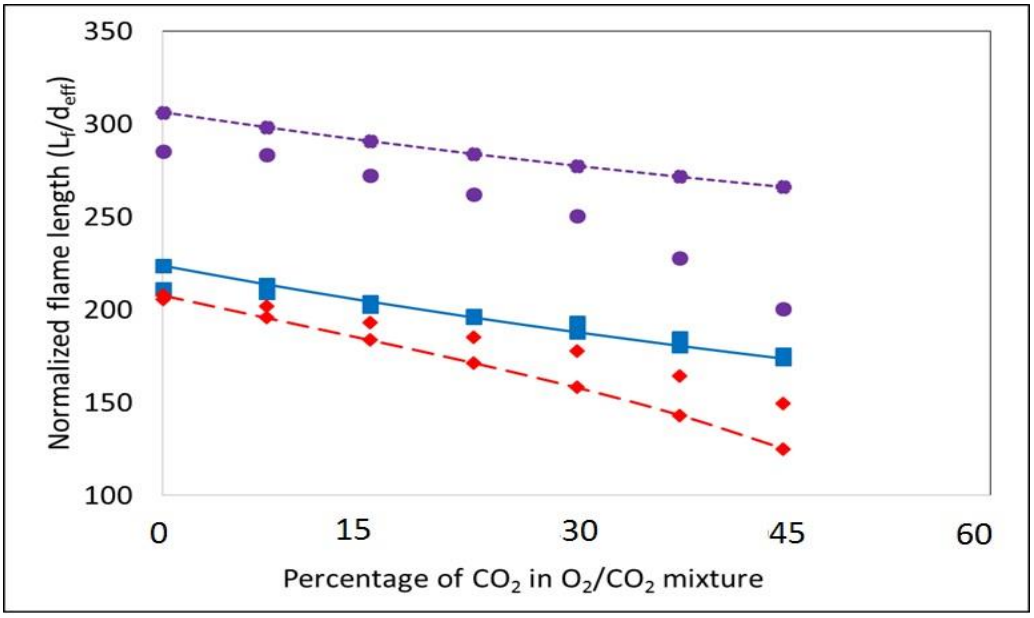

(a) Case of 0% H_2

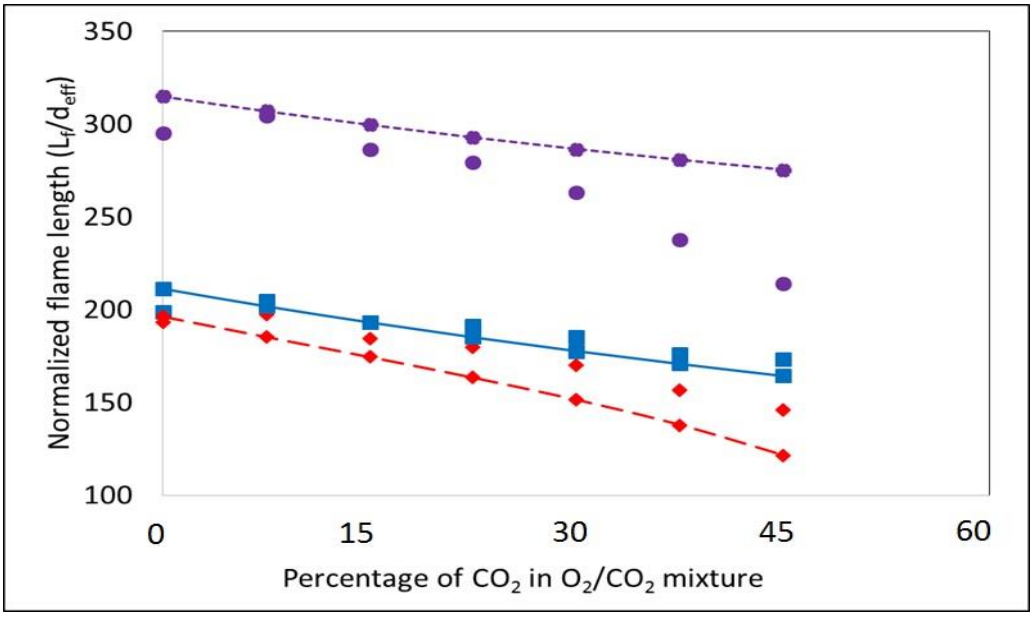

(b) Case of 20% H_2

Figure 3.12: Experimental and modelled normalized flame length for different oxidizer (O_2/CO_2) mixtures and fuel compositions at a firing rate of 4 MW/m3-bar; ■ Near-field concept, ● Far-field concept, ◆ Chen model; experiment-symbol, empirical model-line

CHAPTER 4

NUMERICAL MODELLING AND ANALYSIS

Numerical modelling of a combustion process in a gas turbine involves developing appropriate mathematical flow model along with species transport model, the chemical-turbulence interaction model, the chemical process and radiation models. The developed mathematical models after being solved need to be validated against experimental data. The set of governing equations for continuity, momentum, energy, species, and radiation along with boundary conditions are solved numerically using the CFD Fluent package software.

4.1 Geometry modelling and Meshing

The geometry for numerical modelling was created on GAMBIT 2.4. A 2D axisymmetric condition was used to model the combustion in the vertical model gas turbine combustor. Figure 4.1 shows a schematic diagram for the domain of the model combustor studied numerically. The force of gravity acted parallel to the axis of the combustor in the direction opposite to the flow of the flue gases. The area of the nozzle through which the fuel enters the combustion chamber was calculated from the actual nozzle. The outer and the inner diameter of the fuel pipe was 6.35mm and 4.25mm respectively. The fuel nozzle had a bluff body with 16 channels to allow fuel to pass through as shown in Figure 3.2. This exact geometry cannot be modelled numerically in a 2D geometry. Instead, in the 2D numerical model, the fuel was assumed to flow through an annular spacing. The internal

diameter of the annular spacing was calculated by using the area covered by the 16 fuel channels. Then appropriate mass flow condition was applied to the fuel inlet.

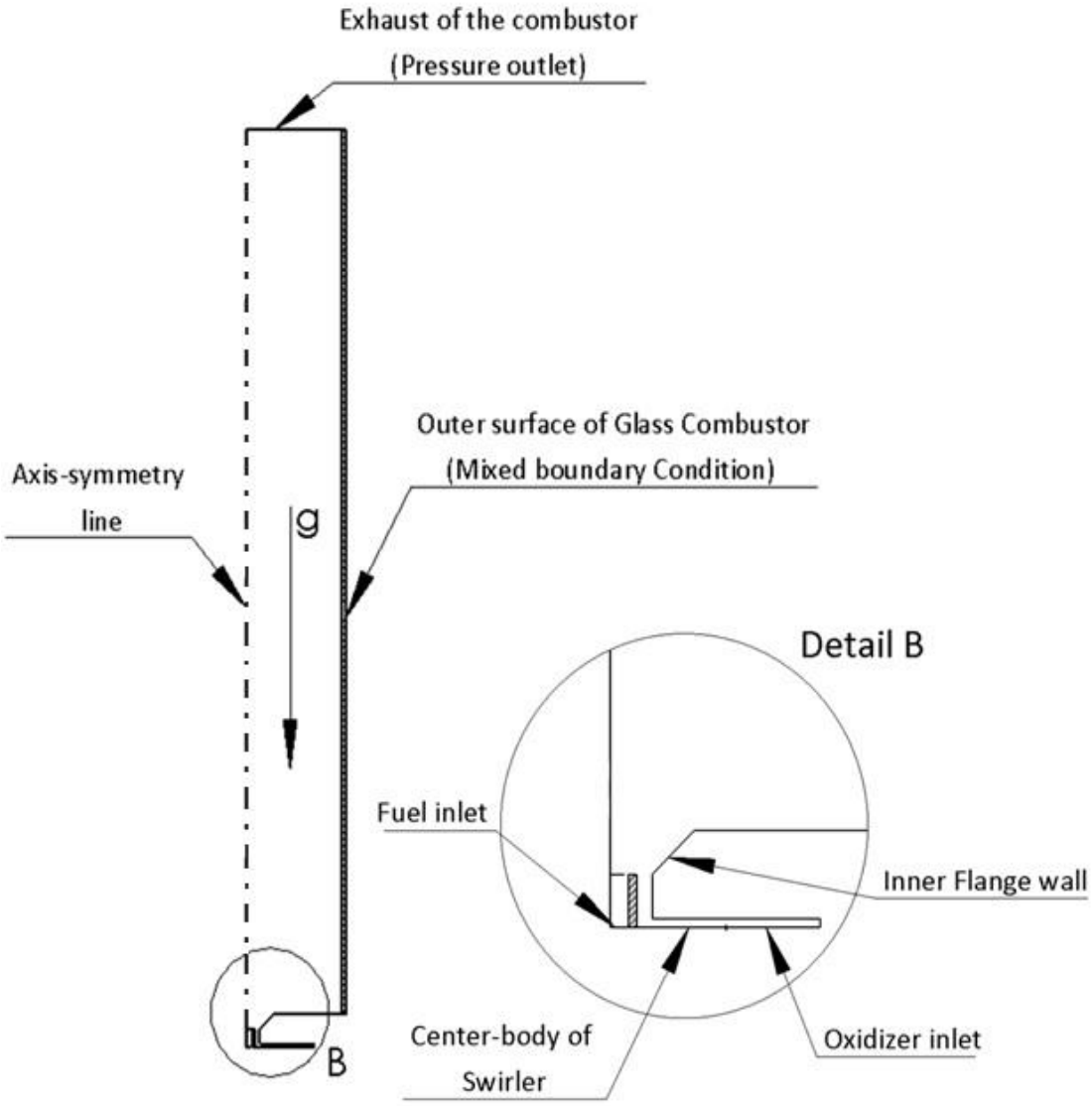

Figure 4.1: Schematic diagram for the domain of the model combustor studied numerically

The 2D geometry was discretized into quadrilateral cells and the grids were concentrated in the regions of high flow gradients, especially near the wall and the fuel inlet, to minimise the errors due to false diffusion. A mesh independence study was carried out with various mesh sizes, to determine the optimum mesh size which would yield results without using a considerable amount of computing resource and time. The set of governing equations for continuity, momentum, energy, species, and radiation along with boundary conditions are solved numerically using the CFD Fluent package software. The software utilises the finite volume approach to discretize the partial differential equations into algebraic equations and then solve them iteratively.

4.2 Boundary Conditions

The convective heat transfer from outside the combustor walls to the ambient was assumed to take place at freestream temperature of 293 K, which was the room temperature of the lab where the experiment was carried out. The emissivity of the quartz glass was taken as 0.93. The fuel and oxidizer were assumed to enter the domain at a temperature of 299 K. The flange on which the glass tube rests is represented by a line instead of the entire domain. However, since only conduction heat transfer takes place, the heat transfer through the conduction in the flange is calculated by assuming a wall thickness of 2cm. The heat is then assumed to be lost to the ambient via convection and conduction. The surface of the flange was assumed to have an emissivity of 0.7. The radiation temperature and the freestream temperature for convective heat transfer were assumed to be same as that used for the glass combustor walls. The density of the gases inside the combustor was calculated using the ideal gas equation.

4.3 Combustion chamber glass wall modelling

The walls of the combustion chamber are made of glass. Glass is a semi-transparent medium. It allows radiation in the visible part of the electromagnetic spectrum to pass through it easily. But, depending upon the type of glass it is partially or completely opaque to the radiation in the infrared region of the spectrum. This is important since most of the heat energy released is in the infrared region. Hence, proper modelling of the radiation through the glass becomes importance. The important parameters to model radiation through the glass is the absorption coefficient and the scattering coefficient in the RTE.

Absorption describes how radiative energy is converted to internal energy of matter. It is one of the two mechanisms, coupling radiative energy propagation with the thermodynamic state of matter. The other is radiative emission, which is proportional to the internal energy of matter and to its temperature. Scattering, on the other hand, causes a change in the direction of radiation propagating along S. During the scattering event, no radiative energy is converted to thermal energy (i.e., scattering in radiation is considered to be perfectly elastic except in some very special cases). However, scattering changes the directional balance of energy propagating in a given direction [71].

The RTE depends upon the absorption coefficient and the scattering coefficient. When both of them are zero there is no effective change in radiation intensity for the radiation passing through the glass. Hence, the used of proper absorption and radiation coefficient is necessary. However, since we are simulating an isolated case without considering the surrounding environment, and the scattering coefficient only effects the change in direction of the radiation, the scattering coefficient can be assumed as zero.

The glass used in the present study is a silica-fused glass, also called as Quartz glass. The complex refractive index m_λ of glass at a wavelength λ is given as,

$$m_\lambda = n_\lambda + ik_\lambda \tag{4.1}$$

Where n is the refractive index of the glass a particular wavelength and k is the absorption index. The refractive index and absorption index for different glass is available in the literature, however, the precision of these data depends upon the material of the glass and the measurement technique. Most studies are focussed on a particular range of the electromagnetic spectrum and do not cover the entire spectrum. Kitamura et al. [106] compiled the data for refractive index and absorption coefficient for silica glass at room temperature from various authors. The resulting set of data covers the electromagnetic spectrum up to 1mm wavelength.

Since the input of absorption coefficient at each wavelength will lead to increase in computation time, the electromagnetic spectrum is divided into several bands and the absorption coefficient for the particular band is taken for the wavelength at the centre of the band. Table 4.1 shows the absorption coefficient and the refractive index of glass divided into certain significant range.

Table 4.1: Absorption coefficient and Refractive index of glass for various bands

Radiation band ($\times 10^{-6}$ m)	Absorption coefficient (m^{-1})	Refractive index
0-0.35	589	1.55
0.35-3	57.88	1.52
3-5	897	1.46
5-300	420000	1.64

4.4 Mesh independence study

Mesh independence study was carried out with appropriate boundary conditions as discussed in the previous chapter. Westbrook-Dryer mechanism along with gas radiation model developed by Smith et al. was used for the study. The fuel inlet size calculated, is very small (~10^{-4} m). The small size of the fuel inlet leads to high aspect ratio of some elements within the mesh when using only quadrilateral elements. This could introduce numerical errors in the simulation especially in the fuel and oxidizer inlet zones where the gradient of temperature and velocity is very high. Therefore, a mixture of triangular and quadrilateral elements were used for the geometry discussed in the previous section. Triangular meshes were used in the oxidizer and fuel inlet zones which required very small mesh elements. In the combustor, quadrilateral mesh elements were used. Figure 4.2 shows the mesh for 11,000 elements. Section A is further magnified in the figure to show the mixture of triangular and quadrilateral mesh.

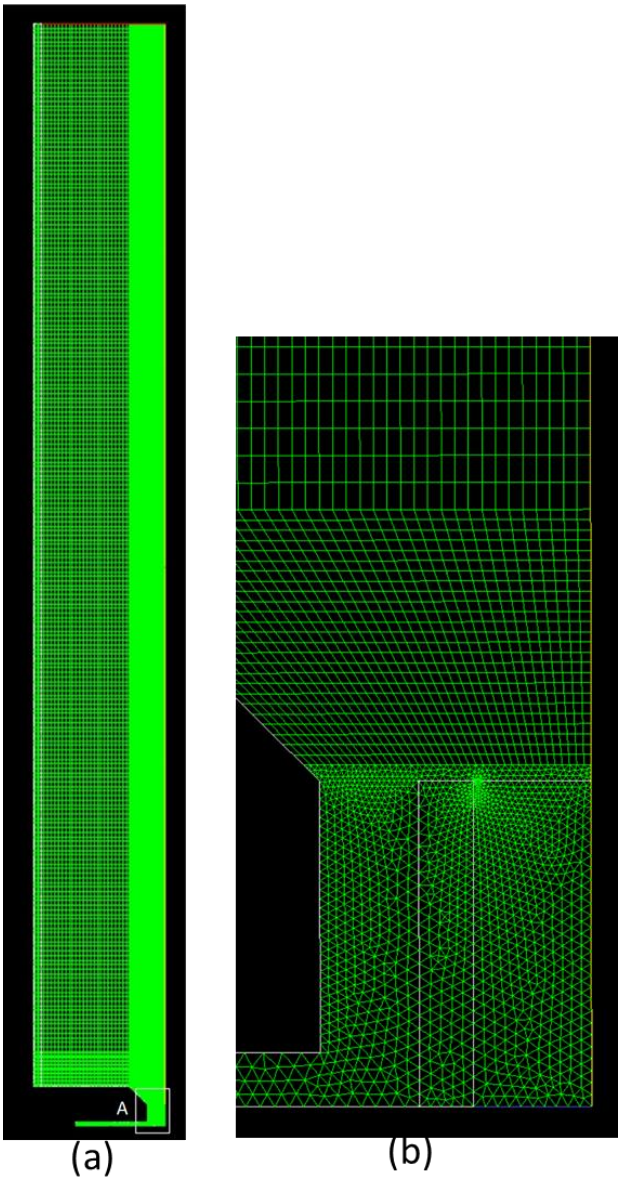

Figure 4.2: (a) Mesh with 11000 cells (b) Detailed view of section-A

The mesh size was varied from 11,000- 64000 elements. The average temperature and the mass fraction of carbon-monoxide (CO) were monitored at the exhaust of the combustor.

Table 4.2: Mesh independence study with various mesh sizes

Mesh Size	Temperature at the exhaust	Percentage difference in temperature from previous mesh size	Mass fraction of CO	Percentage difference in mass fraction of CO from previous mesh size
11000	982.6	-	0.0054136	-
21000	969.46	1.337268	0.0123668	128.4395
31000	967.49	0.203205	0.0131250	6.1309
41000	968.44	0.098192	0.0132976	1.3150
51000	968.45	0.001032	0.0133393	0.3135

From Table 4.2, it can be seen that increasing the mesh size beyond 41000 cells leads to change of less than 0.1% in the temperature at the exhaust, while it leads to change of less than 2% when considering the mass fraction of the CO at the exhaust. While mesh size of 51000 cells offers very little improvement from 41000 cells mesh. Hence, further studies were carried out with a mesh size of 41000 cells.

4.5 Validation of Numerical Model

The numerical results are validated against experimental data. The temperature along the diameter of the combustor at a height of 25m from the dump plane is used to validate the numerical model. For the validation, a combination of three chemical mechanisms (listed in Table *2.1*-2.3) and three weighted sum of grey gas models (WSGGM) are used to determine the most suitable combination of chemical mechanism-radiation model.

The mechanism referred to as WD is the modified Westbrook-Dryer mechanism as shown in Table *2.1*. The mechanism referred to as JL5 is the modified Jones-Lindstedt reaction as shown in Table *2.2*. Another set of mechanisms is obtained by adding the disassociation reactions for H2O and O2 to the modified Jones-Lindstedt reaction shown in Table *2.2*. The resulting mechanism is referred to as JL7.

Table 4.3 shows the possible combinations of chemical mechanisms and radiation models along with maximum observed deviation of numerical temperature from the experimentally measured temperature along the radius of the combustor at 5 cm below the exit of the combustor. For each of the combination, the validation was carried out at two different carbon dioxide composition in the oxidizer mixture, while keeping the global equivalence ratio constant at stoichiometry.

Table 4.3: Reaction Mechanism-Radiation Model combinations along with maximum deviation of numerical results of temperature from experimental measurements of temperature

		Weighted sum of grey gas model (WSGGM)		
		Smith et al. [78]	Johansson et al. (JO) [81]	Bordbar et al. (BO) [85]
Reaction Mechanism	Westbrook-Dryer (WD)	24.6% (WD-smith)	8.9% (WD-JO)	7.7% (WD-BO)
	Jones-Lindstedt 4 step (JL5)	24.6% (JL5-smith)	11% (JL5-JO)	8.3% (JL5-BO)
	Jones-Lindstedt 6 step (JL7)	24.6% (JL7-smith)	13% (JL7-JO)	10.1% (JL7-BO)

The names of the chemical mechanisms and the grey gas radiation models have been shortened for convenience. The radiation model by Johansson et al. is referred to as JO, while the one by Bordbar et al. is referred to as BO.

Figure 4.3 shows the radial temperature at a height of 25 cm from the dump plane, for two CO_2 concentrations, 0 and 35%. From Figure 4.3, it can be seen that all the chemical mechanisms under predict the temperature for pure oxyfuel combustion without carbon dioxide in the oxidizer, when used with the grey gas model presented by Smith et al. [78]. However, at 35% CO_2 in the mixture, the reaction mechanisms are able to predict radial temperature profile quite close to the measured experimental data.

When the reaction mechanisms are used along with JO and BO radiation models the temperatures with 0% CO_2 are much accurately predicted. When using radiation model by Johansson et al. (JO) and the Westbrook dryer (WD) mechanism, the results obtained are within the accuracy of 0-9% for both the cases of 0% CO_2 and 35% CO_2. When used with Bordbar et al. radiation model the prediction by the WD mechanism is slightly better and lies between 0-7.7%.

The JL5 and JL7 reactions give a higher inaccuracy in the range of 3.8-13% when used with JO radiation model for both the cases of 0 and 35%. When using BO radiation model, the two Jones-Lindstedt mechanisms give a much better accuracy which falls in the range of 0.5-10%.

Temperature validation using WSGGM by Smith et al. [78] for (a) 0% CO_2 (b) 35% CO_2

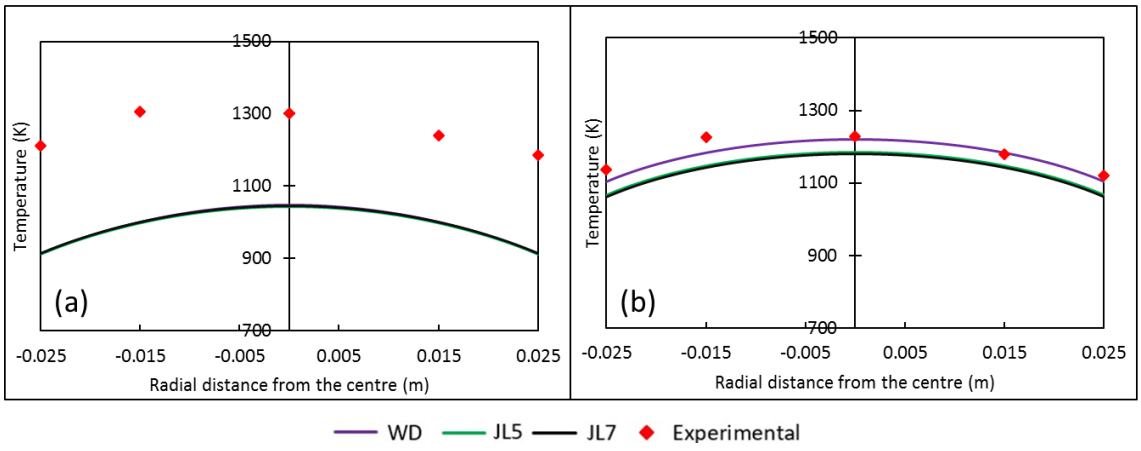

Temperature validation using WSGGM by Johansson et al. [80] for (c) 0% CO_2 (d) 35% CO_2

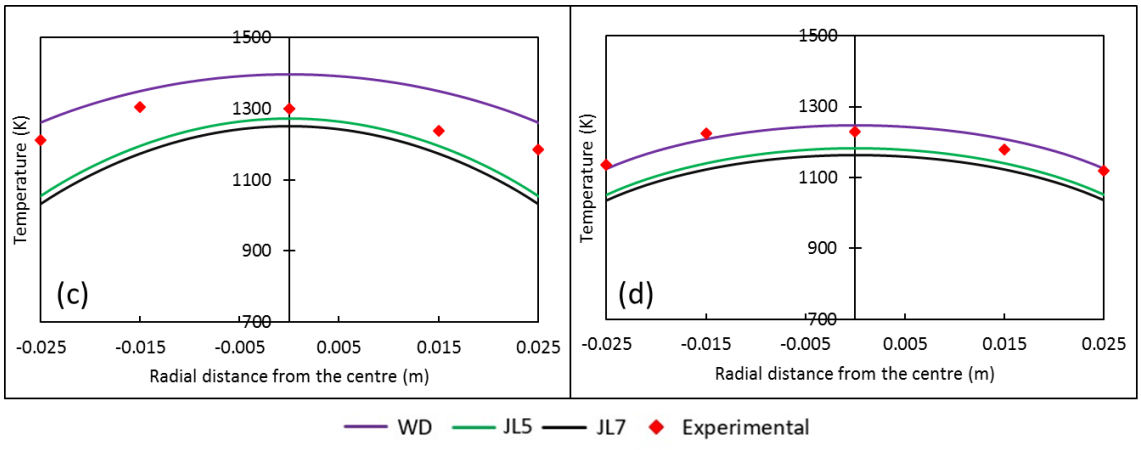

Temperature validation using WSGGM by Bordbar et al. [85] for (e) 0% CO_2 (f) 35% CO_2

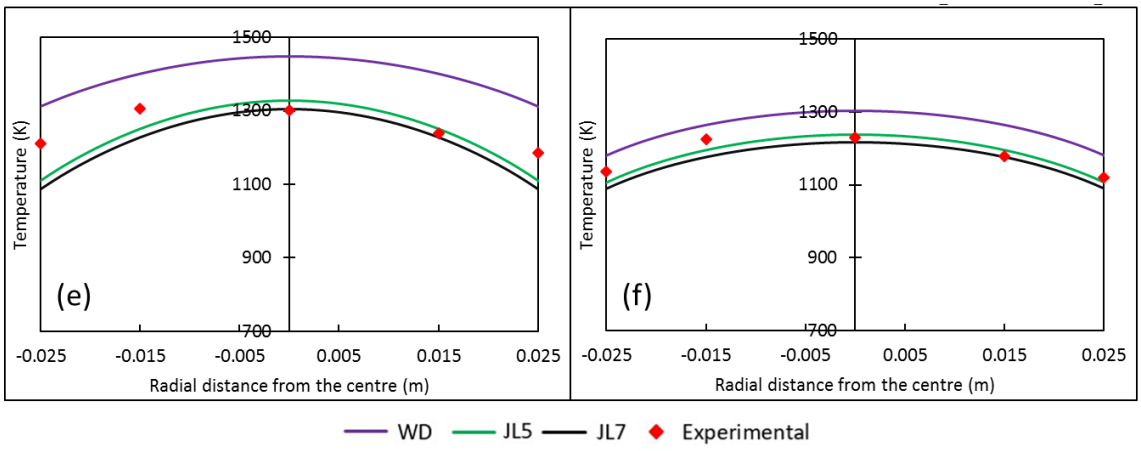

Figure 4.3: Numerical Temperature validation with experimental data

It can also be seen from Figure 4.3 that in most cases the WD predicts a temperature higher than those predicted by the Jones-Lindstedt (JL) mechanisms. The temperatures predicted by JL5 and JL7 are very close to each other. From Table 4.3 it can be seen that the WD mechanism provides the least amount of deviation from the experimental measurements. As such, it makes for a good option to be adopted for further studies. However, the WD mechanism is unable to predict the flame structure near the fuel nozzle for flows with high velocity. Figure 4.4 shows the numerical temperature contour plot in the combustor for 0% and 35% CO_2, using BO radiation model along with different mechanisms. Pictures of the flame captured during the experiments are also shown.

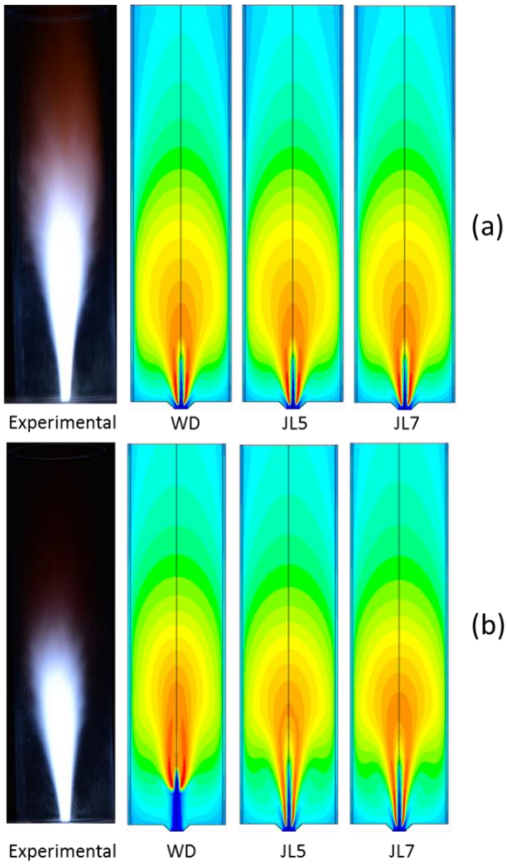

Figure 4.4: Experimental flame structure and Numerical Temperature contour plot using different chemical mechanism for (a) 0% CO_2 (b) 35% CO_2, in oxidizer mixture

The temperature contour plots for the three mechanisms for 0% CO_2 in the oxidizer are quite similar to one another. However, at 35% CO_2 the case with WD mechanism shows a lifted flame, stabilised away from the fuel nozzle, which is clearly not the case as can be seen in the experimental image. The WD mechanism predicted lifted flame for CO_2 as low as 20%. The WD mechanism is unable to capture the temperature distribution accurately, suggesting that while the WD mechanism may be able to predict the temperature downstream of the flame accurately, it is not able to capture the attachment of flames to the fuel nozzle.

The JL7 reaction mechanism, involves two additional reactions in comparison to JL5, to model the O_2 and H_2O decomposition. These additional reactions can help predict the distribution of OH radicals within the combustor. Apart from this, JL5 and JL7 mechanisms predict very similar temperature within 2% of each other. Moreover, the solution convergence time with JL7 mechanism is higher than that with the JL5 mechanism. Thus, use of JL5 mechanism offers better convergence time along with similar results to JL7 mechanisms and is most suited unless the distribution of OH radicals is of concern.

Hereafter, further parametric studies are carried out using the weighted sum of grey gas model suggested by Bordbar et al. along with modified JL5 reaction mechanism.

4.6 Flame structure

In this section, an attempt to understand the flame structure is made. While the numerical temperature contour may not give an accurate prediction of the visible flame, it helps identify and understand the zones with high and low temperatures, giving an insight into the flame structure. Figure 4.5(a) shows a detailed view of the temperature contour plot near the inlet of the fuel and oxidizer, for the case of pure oxyfuel combustion of methane at stoichiometry.

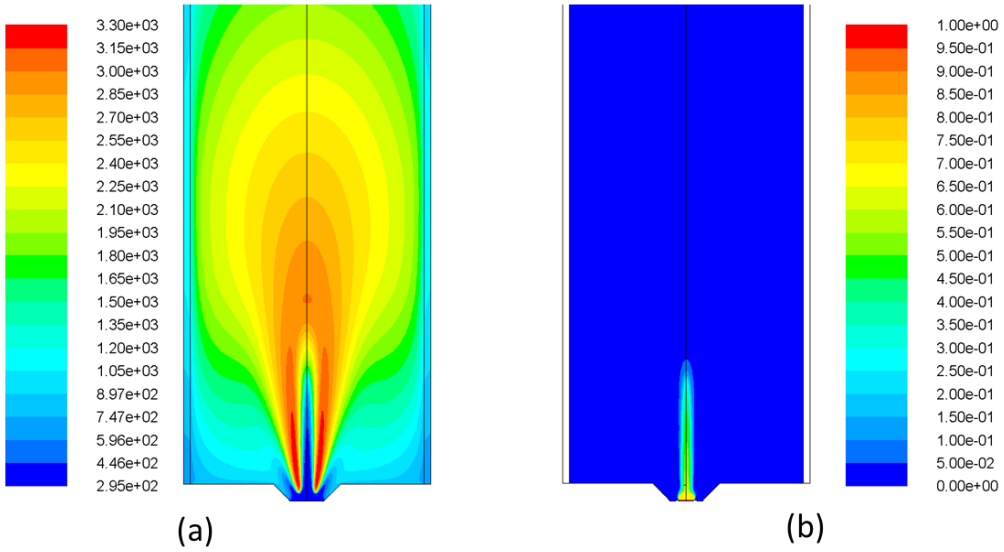

Figure 4.5: Detailed view of (a) temperature contour (b) CH_4 mass fraction distribution contour, for 100% oxygen oxidizer stream

The temperatures shown are in Kelvin. It can be seen that the methane and oxygen combust to give a flame along the axis of the combustor. Maximum temperatures do not occur along the axis of the combustor but rather occurs near the fuel inlet along a cylindrical zone around the oxidizer-fuel mixture that is at a lower temperature. The flame is characterised with a preheat zone in the interior, where the methane-oxygen mixture is preheated before

it can combust. Figure 4.5(b) shows the mass fraction of methane near the inlet of the fuel and oxidizer. As soon as the methane-oxygen mixture reaches the ignition temperature of methane, all of it combusts to form intermediate species CO and H_2. The intermediate species CO and H_2 are further oxidised to form the final products CO_2 and H_2O, which also releases a significant amount of heat down the combustor.

4.7 Effect of CO_2 content

The effect of addition of CO_2 on the temperature distribution inside the combustor and the emissions from the combustor is examined. Oxyfuel combustion of methane at stoichiometry was carried out inside the combustor in the gas turbine region, with a firing rate of 4 MW/m^3. Figure 4.6 shows the contour plot as well as the experimental flame at different CO_2 percentages. It can be seen, from the experimental images that, as the CO_2 percentage increases the visible flame becomes shorter and lifts off from the base.

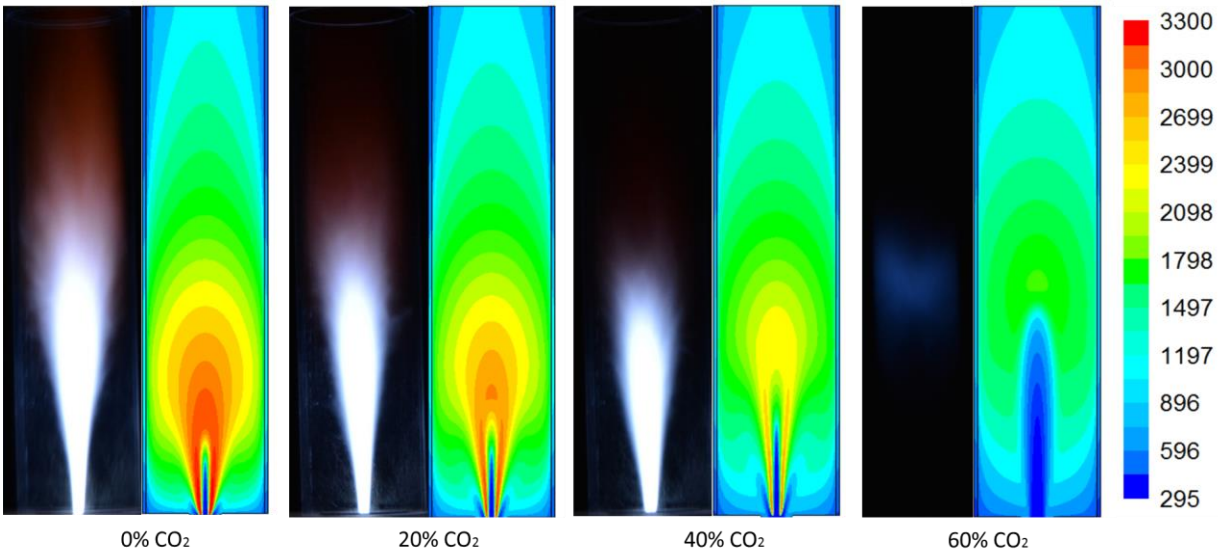

Figure 4.6: Visible experimental flame and Numerical Temperature contour plot at different CO_2% in the CO_2/O_2 oxidizer stream

Comparing the flame structure, one can observe that as the composition of CO_2 in the CO_2/O_2 mixture increases the inner preheating zone of the flame also increases in height. This is because of the high velocity of the gases associated with increase in CO_2. At 60% CO_2, the preheat zone is relatively very large and the combustion occurs close to the combustor wall.

For pure oxy-methane combustion, the high flame speed, coupled with the lower specific heat of CO_2 at high temperature and poor radiative heat transfer properties of O_2 leads to high flame temperatures within the combustor. Figure 4.7 shows the peak temperature within the combustor at stoichiometry, along with the temperature of the gases at the exhaust, with varying CO_2 percentages.

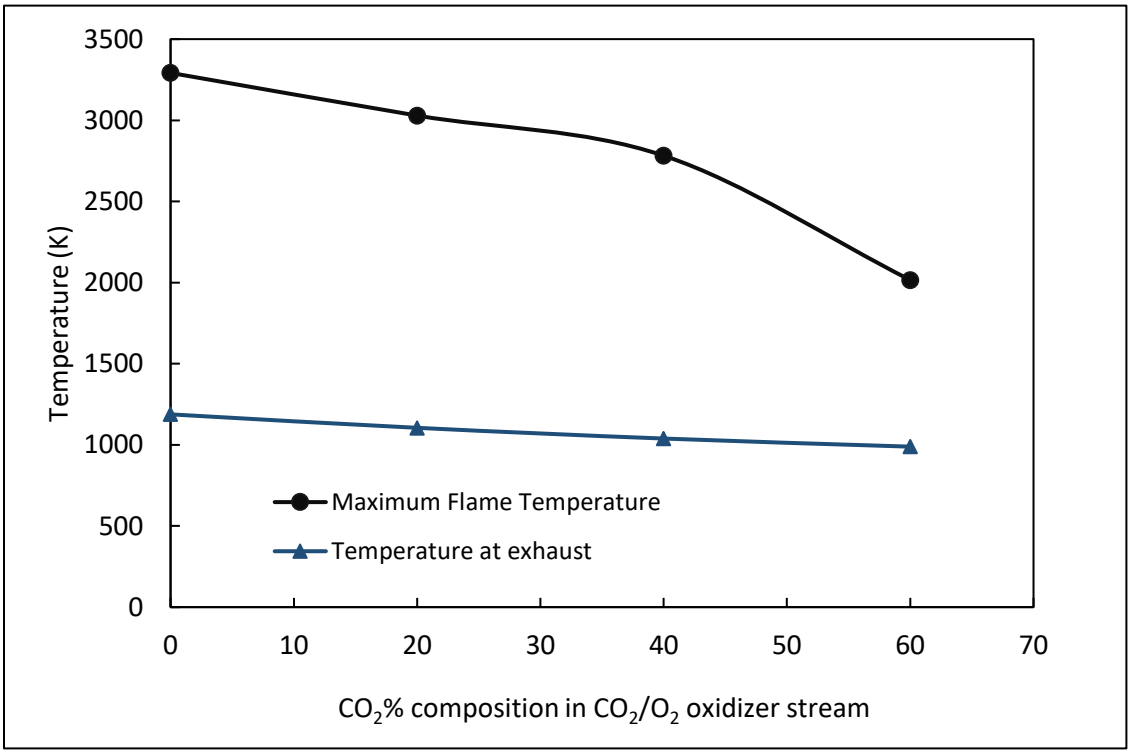

Figure 4.7: Maximum flame temperature and exhaust gas temperature

The peak temperature is observed to be the highest for the case of pure methane-oxygen combustion without CO_2. As CO_2 is introduced into the combustor, due to its physical and chemical properties the burning velocity of methane is reduced, which lowers the peak temperature within the combustor. CO_2 by virtue of its high specific heat at higher temperatures is able to absorb a large amount of heat to bring down the temperature within the combustor. As a result, with increases in CO_2 concentration in the oxidizer, the temperature of the gases at the exhaust also decreases as can be seen Figure 4.7.

For 20% CO_2, there is an 8% decrease in maximum flame temperature and 7% decrease in temperature of the gases at the exhaust in comparison to the case with 0% CO_2 in the oxidizer. For 40% CO_2, there is an 8.1% decrease in maximum flame temperature and 6% decrease in temperature of the gases at the exhaust in comparison to the case with 20% CO_2 in the oxidizer. At 60% CO_2, the maximum flame temperature reduces by 27.5% but the temperature at the exhaust only reduces by 4.8% in comparison to the case with 40% CO_2.

These figures could be explained by considering the heat lost from the gases. Convection and radiation are the major phenomena responsible for carrying the heat from the gases. The heat lost via radiation can be defined as,

$$radiation\ fraction = \frac{radiative\ heat\ on\ the\ combustor\ boundaries}{total\ heat\ generated\ by\ chemical\ reaction}$$

Figure 4.8 shows the radiation fraction of the heat loss from the combustor.

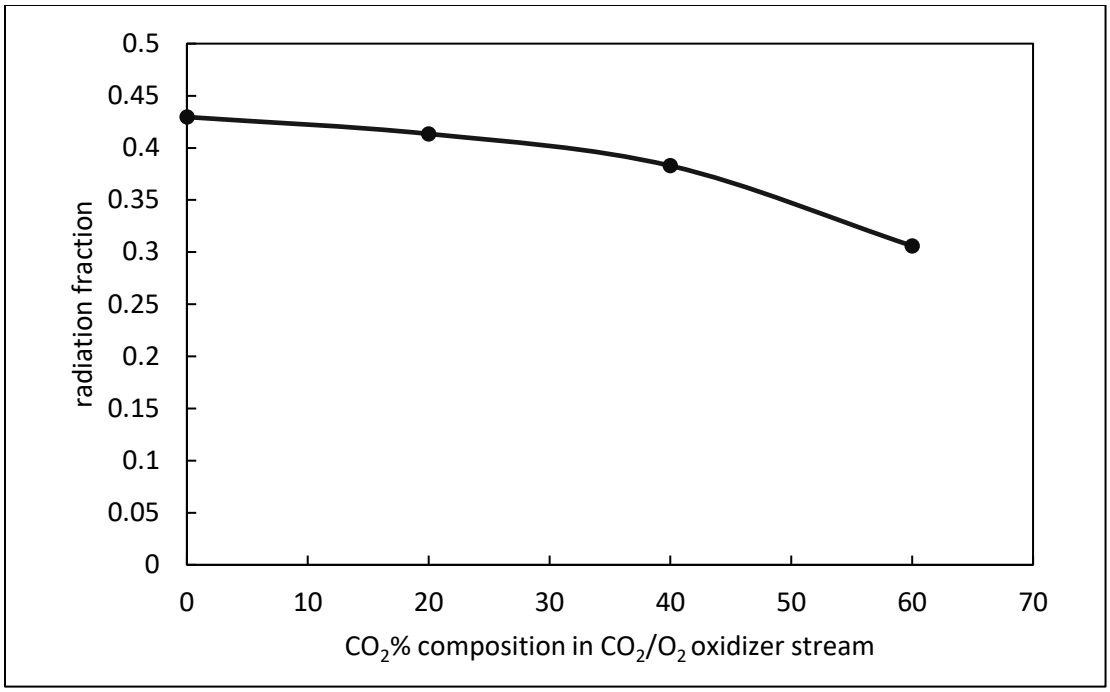

Figure 4.8: Radiation fraction at different CO_2 composition

It can be seen from the figure that as the CO_2 composition in the oxidizer increases the radiation fraction decreases. From 0 to 20% increase in CO2 composition, the radiation fraction decreases by 3.7%. When increasing CO_2 composition from 20 to 40%, the radiation fraction decreases by 7.4%. This decrease in radiation fraction is more pronounced when the CO_2 composition is increased from 40 to 60%. This results in a decrease of 20% in the radiation fraction. As the percentage of CO_2 in the mixture is increased the burning velocity of the fuel decreases (Figure 4.9), resulting in decreased temperatures within the combustor (Figure 4.10). The decreased temperature results in lower heat flux emission from the flame, as a result, the radiation fraction of the flame decreases.

When increasing the CO_2 composition in the oxidizer stream from 40% to 60%, the CO_2 reduces in lower heat loss via radiation. However, the heat generated by combustion of

CH_4 is mostly carried away by convection. Thus, while the maximum flame temperature reduces by 27.5% the temperature at the exit of the combustor reduces by 4.8% as more heat transfer occurs via convection.

The reduction in burning velocity of methane is evident from Figure 4.9. Figure 4.9 shows the kinetic rate of reaction for the primary methane reaction. The reaction is shown in Table *2.2* as reaction-1.

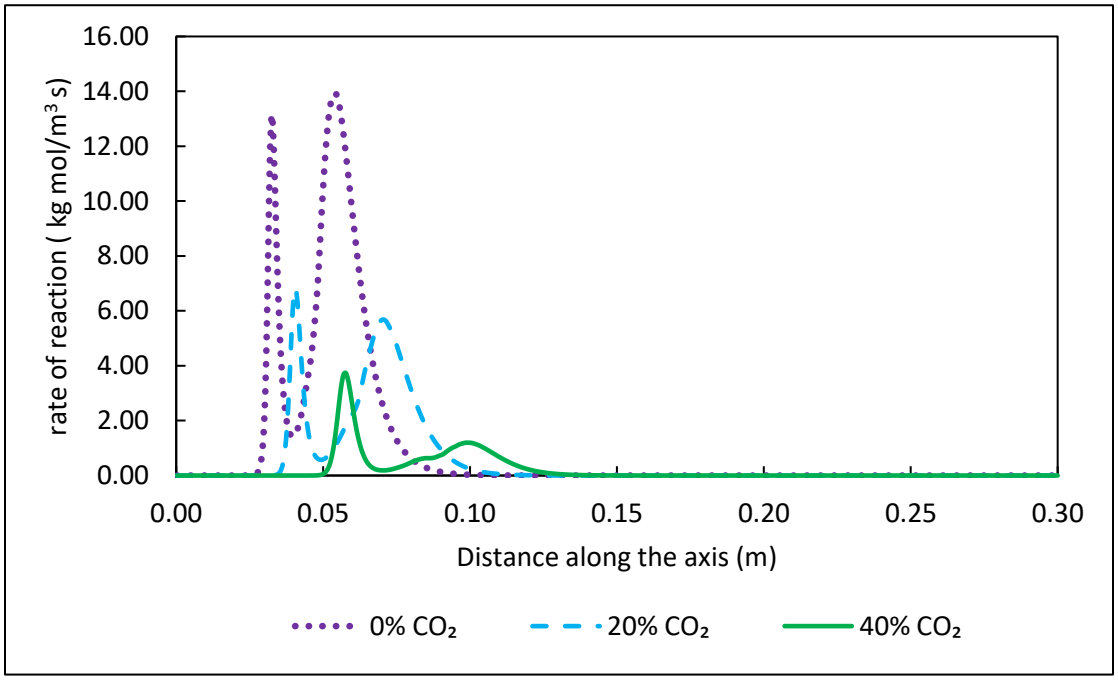

Figure 4.9: Kinetic rate of reaction-1 (Table *2.2*) for different CO_2 composition

It can be seen from the figure as the amount of CO_2 in the O_2/CO_2 oxidizer mixture is increased the rate of reaction for the primary reaction-1 (Table *2.2*) decreases. The reduction in burning velocity of methane due to the addition of CO_2 has been confirmed by Shy et al. [107,108]. The decreased methane burning rates lead to decrease in temperatures.

Figure 4.10 shows the temperature distribution along the axis of the combustor. It can be seen that with the introduction of CO_2 in the oxidizer, the peak temperature along the axis reduces.

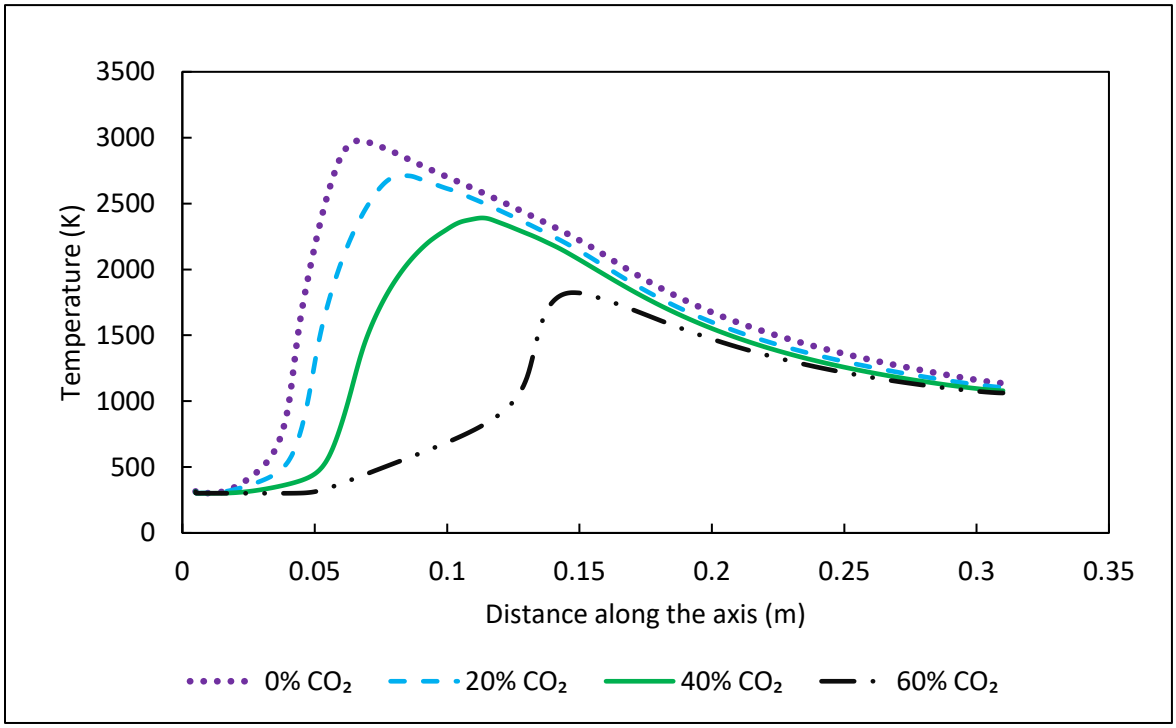

Figure 4.10: Temperature distribution along the axis of the combustor for different CO_2 composition in CO_2/O_2 oxidizer stream

The peak temperature also shifts away from the flame base with increase in CO_2 percentage in the oxidizer. This shift can be attributed to the decrease in the burning velocity of methane. A similar observation was made by Ditaranto and Oppelet [33]. It should also be noted that the maximum flame temperature does not lie on the axis of the combustor, rather the maximum flame temperature exists along the sides of the flame in the region near the fuel inlet, as can be seen in Figure 4.5.

Figure 4.11 shows the distribution of species along the axis of the combustor for (a) 0% CO_2 and (b) 40% CO_2. From the figure, it can be seen that H_2O is a product formed in the combustion zone as a result of the reaction of CH_4 with O_2. Beyond the reaction zone, the amount of H_2O remains almost constant.

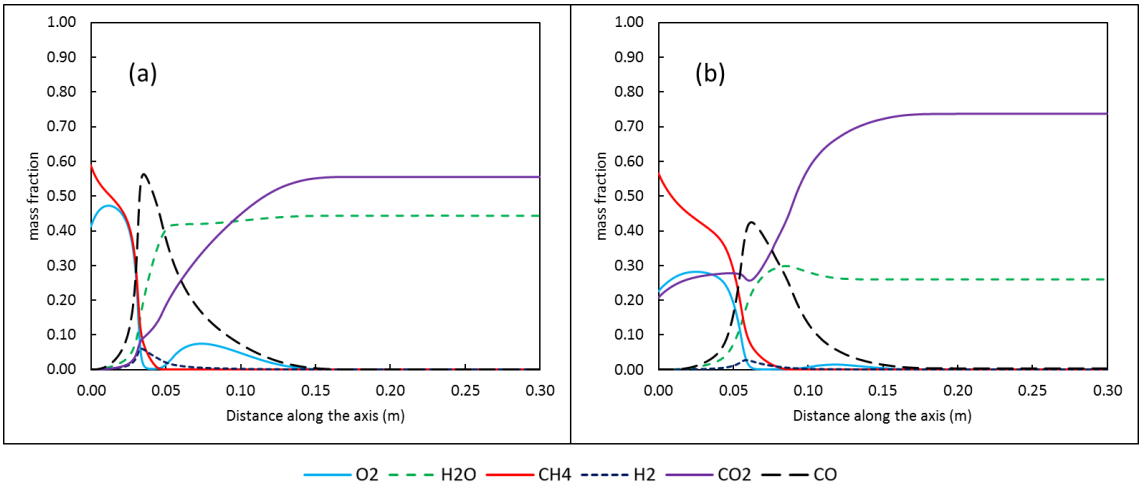

Figure 4.11: Species Mass fraction along the axis of the combustor for (a) 0% CO_2 (b) 40% CO_2

It can be seen that while the mass fraction of H_2O remains constant beyond the flame region, however, the mass fraction of CO_2 increases beyond the flame zone. This is because of CO which reacts with O_2 to form CO_2. The mass fraction of CO is high in the flame zone and decreases down the combustor. This is because CO is an intermediate compound, formed by the reaction of CH_4 with O_2. Mass fraction of CO decreases down the combustor (away from the flame zone) as CO further reacts with O_2 to form CO_2. It can be seen that the mass fraction of CO and O_2 reaches close to zero at the same point along the combustor. Also, the mass fraction of CO_2 reaches its peak at the very same point.

The amount of CO produced as an intermediate product in the flame decreases with the increase of CO_2 percentage from 0-60 in the oxidizer. This is due to the addition of CO_2 which not only helps bring down the peak temperature inside the combustor but also improves the mixing inside the combustor resulting in lower peak CO production. Figure 4.12 shows the mass of CO that is produced inside the combustor.

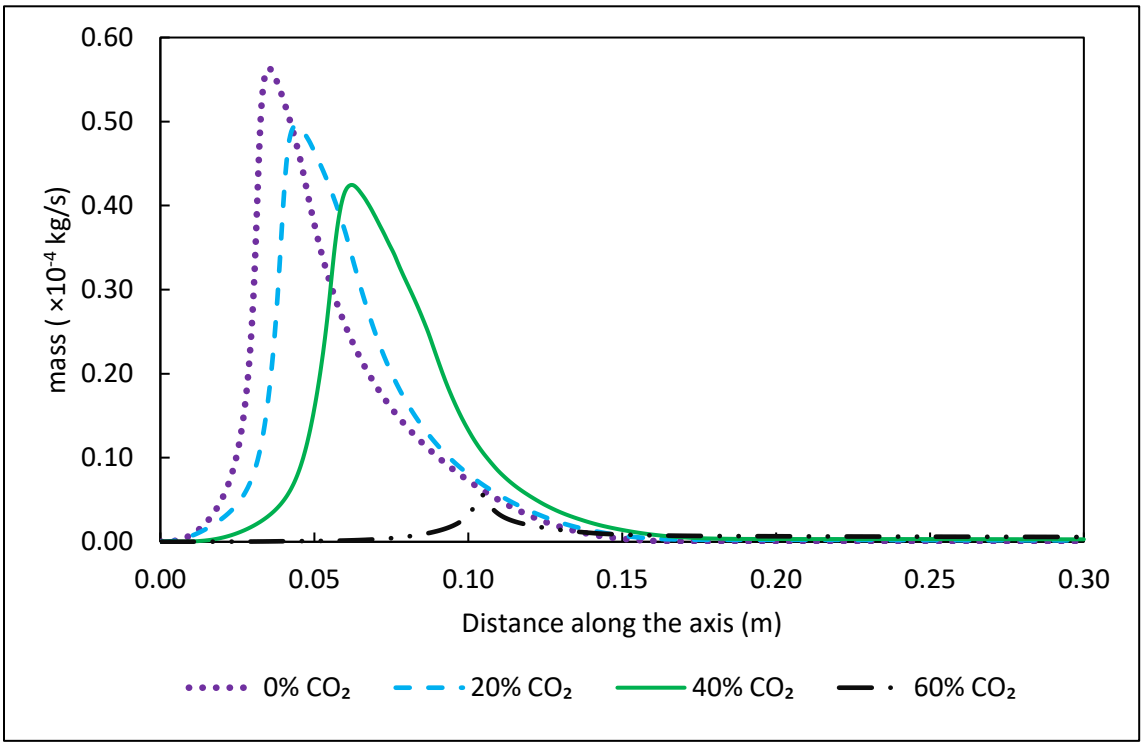

Figure 4.12: Mass of CO produced along the axis of the combustor

From Figure 4.12 it can be seen very less intermediate CO is produced in the flame for the case of 60% CO_2 in the oxidizer. However, it can also be seen that a higher amount of CO exits the combustor in the flue gas. Despite less CO being produced inside the combustor with increase of CO_2 amount in the oxidizer, the CO emission at the exhaust increases with increase in CO_2 percentage in the oxidizer. Figure 4.13 shows the amount of CO at the exhaust in ppm. Least amount of CO is emitted for 0% CO_2. It can be seen that the CO

emission at the exhaust drastically increases with the increase of CO_2, while the temperature at the exhaust decreases (Figure 4.7).

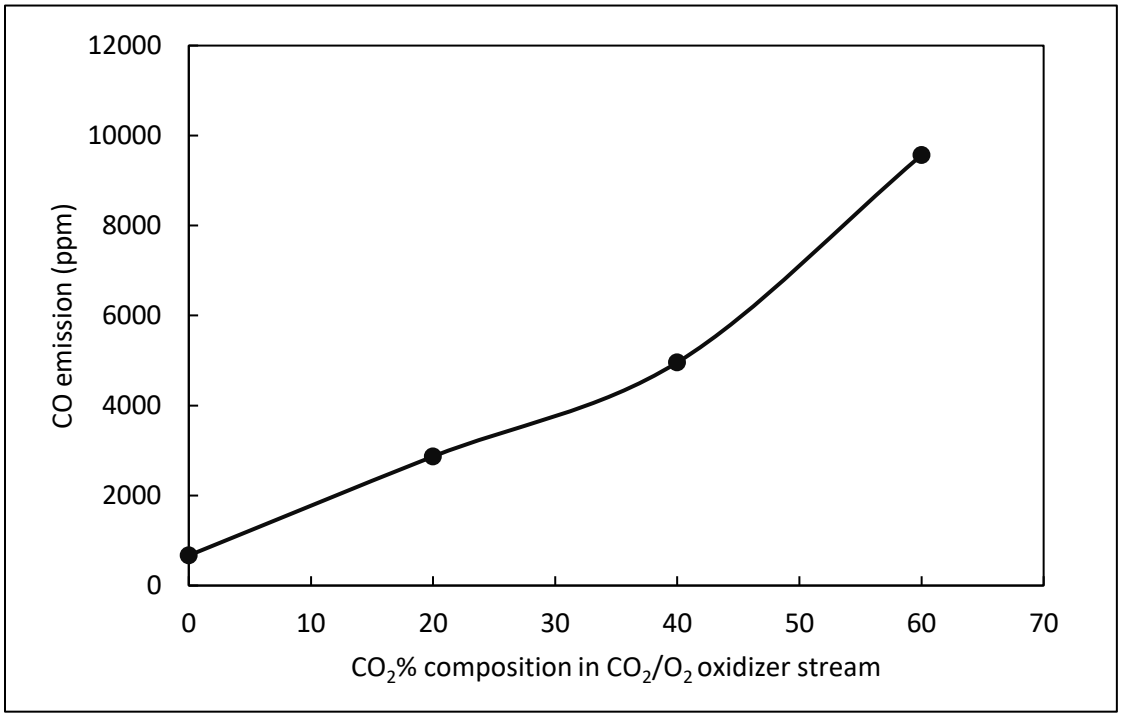

Figure 4.13: CO emission at the exhaust

The increase in CO emission with increase in CO_2 concentration could be understood by looking at Reaction 5 of the JL5 reaction mechanism. CO is an intermediate product, formed by the reactions 1 and 2 (Table *2.2*). The CO formed via reaction mechanism 1 and 2 is oxidised to CO_2 via reaction 5 (Table *2.2*). However, the presence of excess CO_2 inhibits the oxidation of CO to CO_2. Abian et al. [109] showed that the presence of CO_2 can inhibit the oxidation of CO.

Another possible explanation could be the reduced residence time. Richards et al. [21] reported increase in CO burnout time with decrease in adiabatic flame temperature, especially for the case of stoichiometric combustion of methane, which showed

exceptionally long CO burnout time. With the increase in CO_2 percentage in the oxidizer, the mass flow through the combustor increases, resulting in high flow velocities of the gases. Figure 4.14 shows the gas residence time inside the combustor.

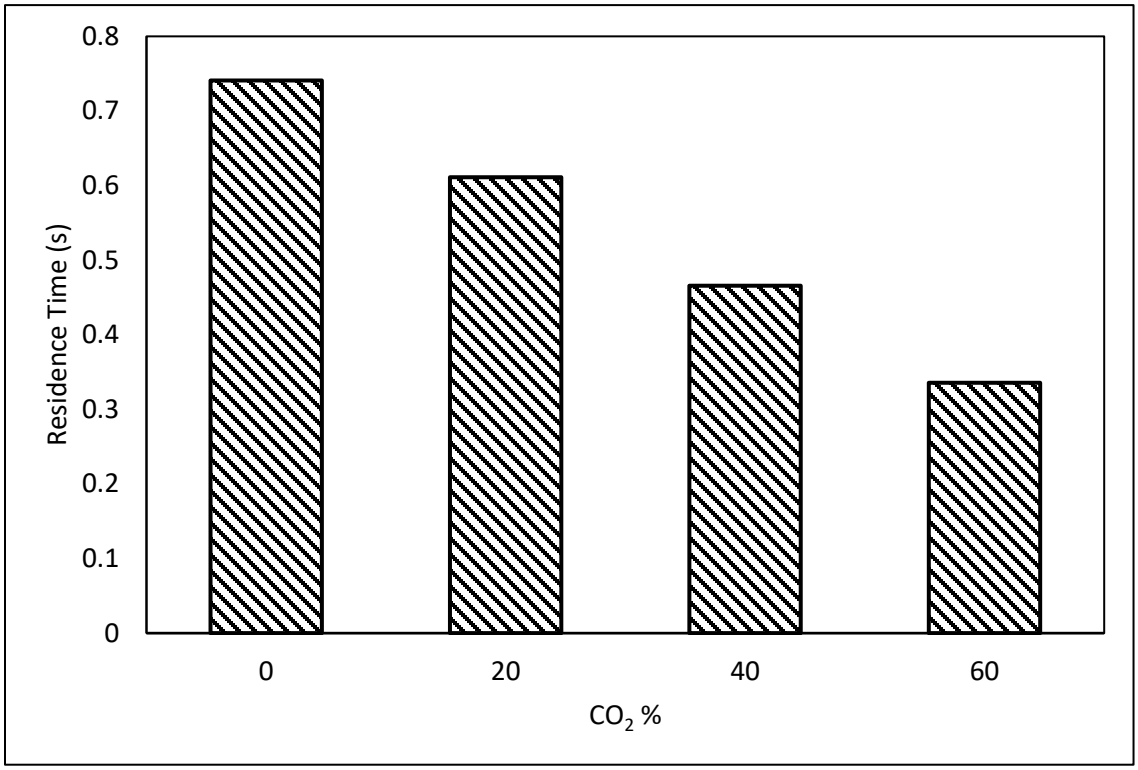

Figure 4.14: Gas residence time

As more CO_2 is added the flame temperature is reduced due to which more residence time is needed for CO to completely burn out to form CO_2. However, the increased CO_2 reduces the residence time of the gases in the combustor, this leads to an increased CO emission as more CO_2 is added to the oxidizer stream.

Figure 4.15 shows the streamlines of the flow inside the combustor superimposed over the temperature contour of the combustor.

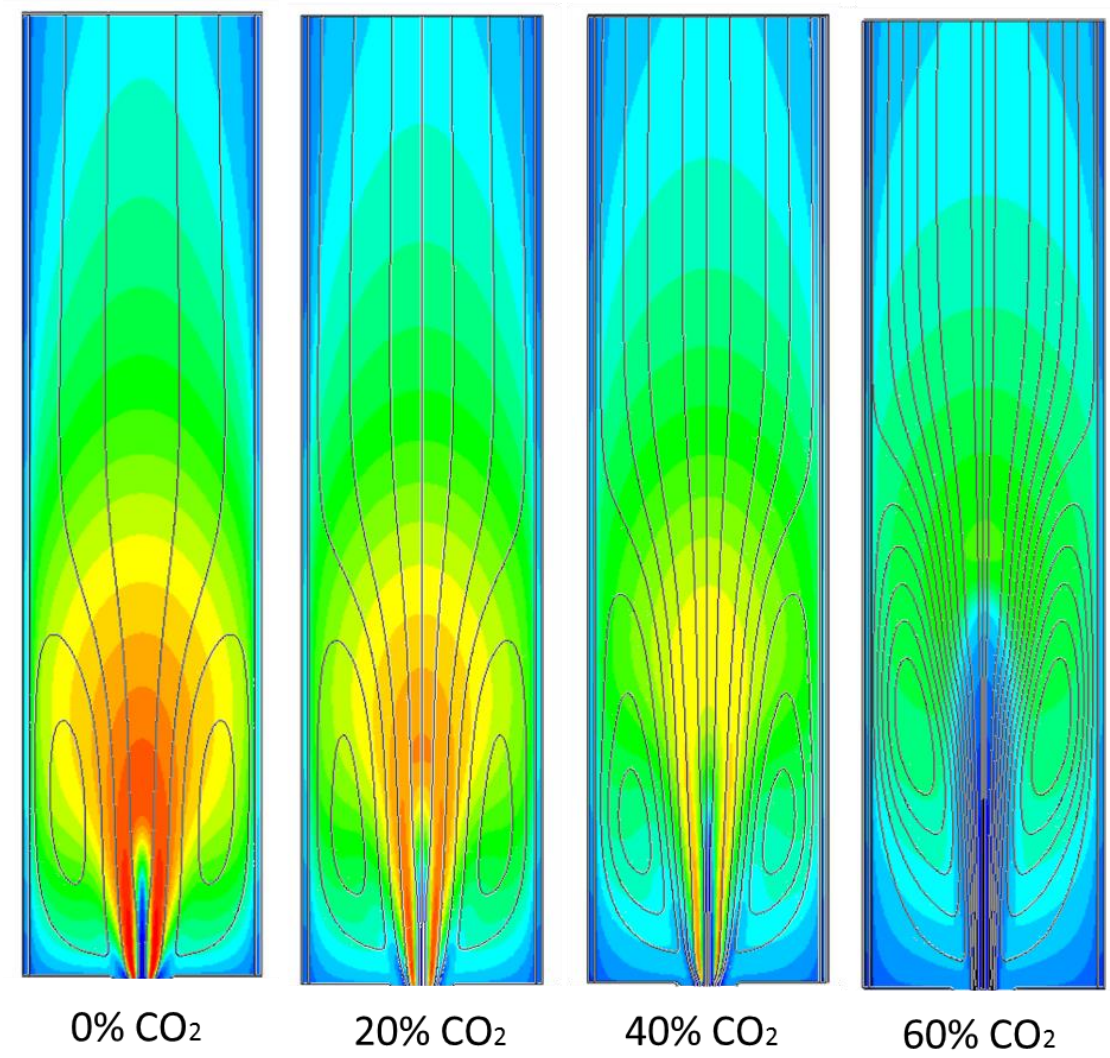

Figure 4.15: Streamlines of flow superimposed over temperature contour

The flow inside the combustor is characterised by a recirculation zone near the combustor dump plane. The recirculation zone increases in strength with increase in the CO_2 composition in the CO_2/O_2 oxidizer mixture, because of the increased mass flow rate through the combustor. As the amount of CO_2 added to the CO_2/O_2 oxidizer mixture, the recirculation zone also tends to increase in size, with 60% CO_2 having the strongest and the largest recirculation zone of the studied case. This recirculation zone tends to destabilise the flame near the nozzle and tends to lift the flame, resulting in a lifted flame

at 60% CO_2 in the CO_2/O_2 oxidizer stream. Figure 4.16 shows the axial velocity of the gases along the centre of the combustor.

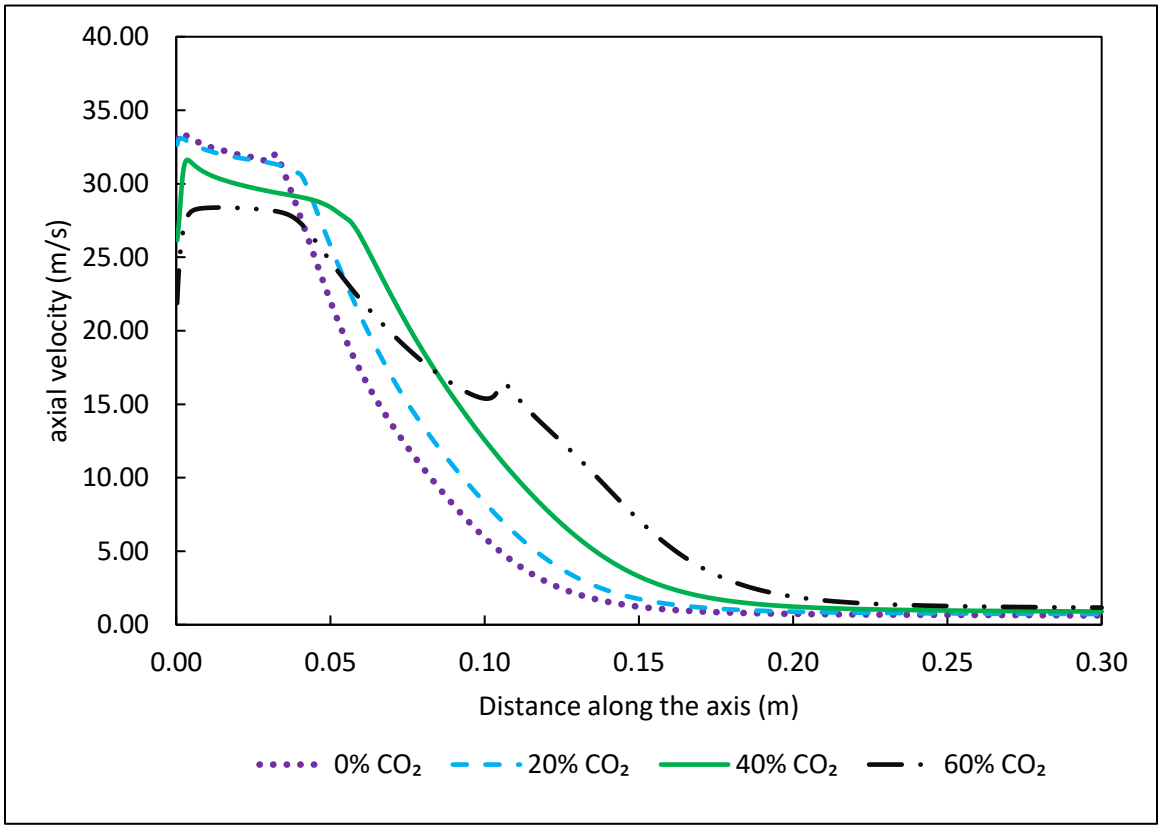

Figure 4.16: Axial velocity along the axis of the combustor at different CO_2 percentage

The velocity shown for the case of 0% CO_2 shown in Figure 4.16 is the highest near the fuel nozzle, despite having a low mass flow rate in comparison to cases with CO_2 present in the oxidizer stream. It should be noted that the presented axial velocity is for the axis inside the combustor. The gas for the case of pure oxy-methane combustion has the highest temperature, hence the gas expands more and this result in a lower density but higher velocity to maintain the continuity. Hence, high velocity exists near the fuel nozzle. However, beyond the flame zone, it can be seen that the velocity for the case of pure oxy-

methane combustion, decreases to the lowest, while the case with 60% CO_2 has the highest velocity near the exit of the combustor.

The fuel and the oxidizer meat at the fuel inlet plane, to mix and combust. A 45° swirler was used to provide a swirl flow to the oxidizer. However, once the oxidizer passes through the burner head, a significant decrease in the swirl angle, was found at the fuel inlet plane. Figure 4.17 shows the detail view of burner head with arrows representing the flow pattern. The decrease in the swirl angle is because of the burner head which obstructs the incoming swirling flow from the swirler. The annulus diameter of the burner head is smaller than that of the swirler centre body, due to which, the flow has to change direction, towards the centre of the combustor, resulting in most of the flow moving radially before it can move axially and pass through the annulus in the burner head. This change in directions causes the flow to lose a significant amount of swirl, resulting in a low swirl angle at the fuel inlet plane.

The swirl angle at the fuel inlet plane is calculated as [110],

$$\tan^{-1}\left(\frac{V_\theta}{V_{axial}}\right) \tag{4.2}$$

Figure 4.18 shows the calculated swirl angle at the fuel inlet plane when a swirler with vane angles of 45° is used. At the fuel inlet plane, the swirl angle is expected to be in the vicinity of 45° so as to have an efficient mixing. The swirl flow also helps stabilise the flame [110,111]. The decreased swirl angle, causes the flame to behave more like a jet flame. As the amount of CO_2 in the oxidizer stream is increased from 0% to 60% the swirl angle increases, as can be seen in Figure 4.18 but still is significantly smaller than 45°.

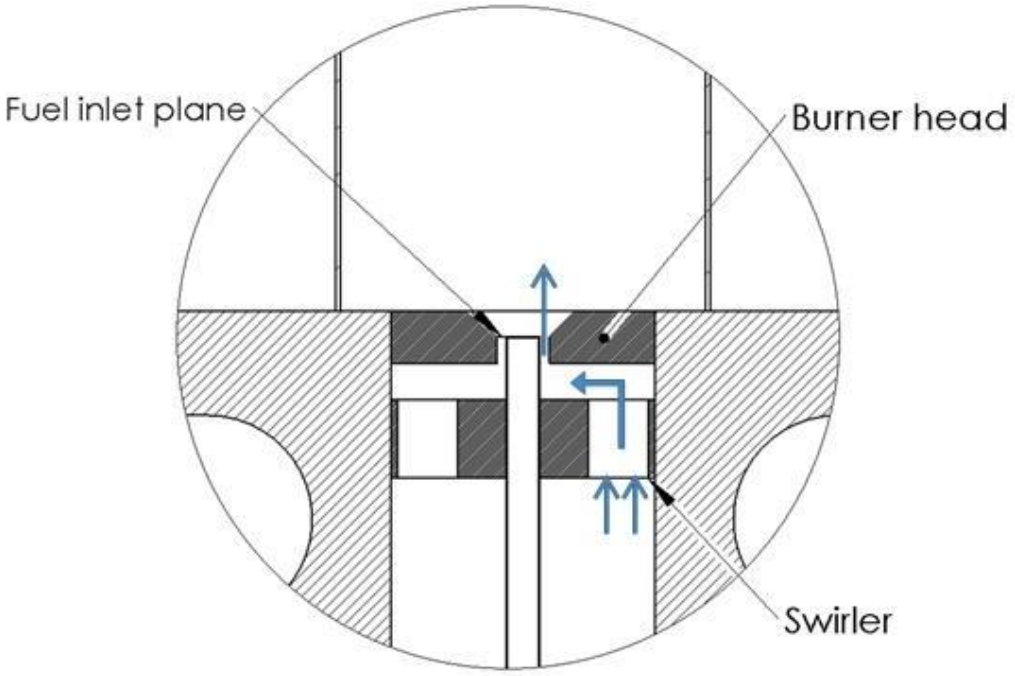

Figure 4.17: Detail view of flow through swirler and burner head

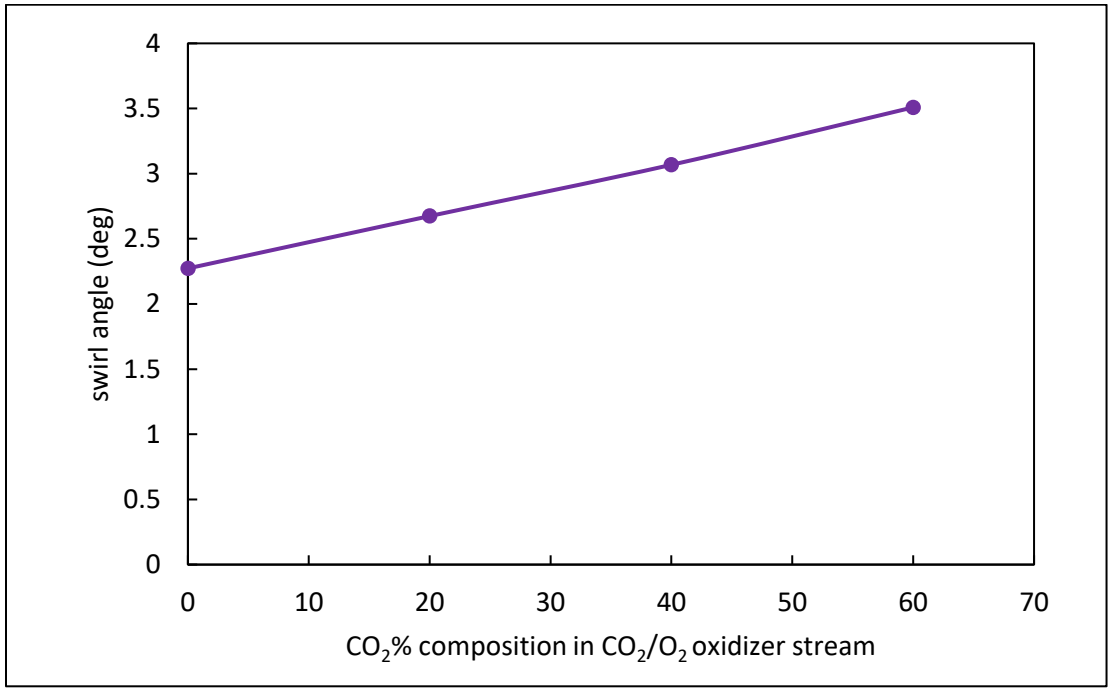

Figure 4.18: Swirl angle at the fuel inlet plane with a swirler of 45° vane angle

This improper design of the burner head also causes stability issues, as lifted flames are observed at 30/70 ratio of O_2/CO_2 oxidizer composition. 30/70 ratio of O_2/CO_2 oxidizer composition gives adiabatic flame temperature close to that of air.

Thus, a better design for burner head is needed, which can provide a good swirl flow, this is addressed in Chapter 6. The following studies in section 4.8 and 4.9 are carried out using the poorly designed burner head.

4.8 Effect of Energy Level

In this section, the effect of varying the energy level of the combustor is examined while keeping the composition of CO_2 in the CO_2/O_2 oxidizer mixture constant. All the results discussed in this section pertains to cases with 0% and 40% CO_2 in the CO_2/O_2 oxidizer mixture. Figure 4.19 shows the temperature contour plot for different energy levels.

The energy level is varied by changing the mass flow rate of the fuel (Methane, CH_4). correspondingly the oxidizer mass flow rate is also increased to maintain a stoichiometric (Φ=1) combustion condition. It can be seen in Figure 4.19 that as the energy level is increased the flame tends to increase in length. As the mass flow rate increases due to increase in energy level, the flame tends to lift off from the fuel nozzle and stabilise at a small distance away from the fuel nozzle. Despite the increase in energy level the maximum temperature inside the combustor remains almost constant, as can be seen in Figure 4.20. Figure 4.20 shows the maximum flame temperature and the temperature at the exhaust of the combustor.

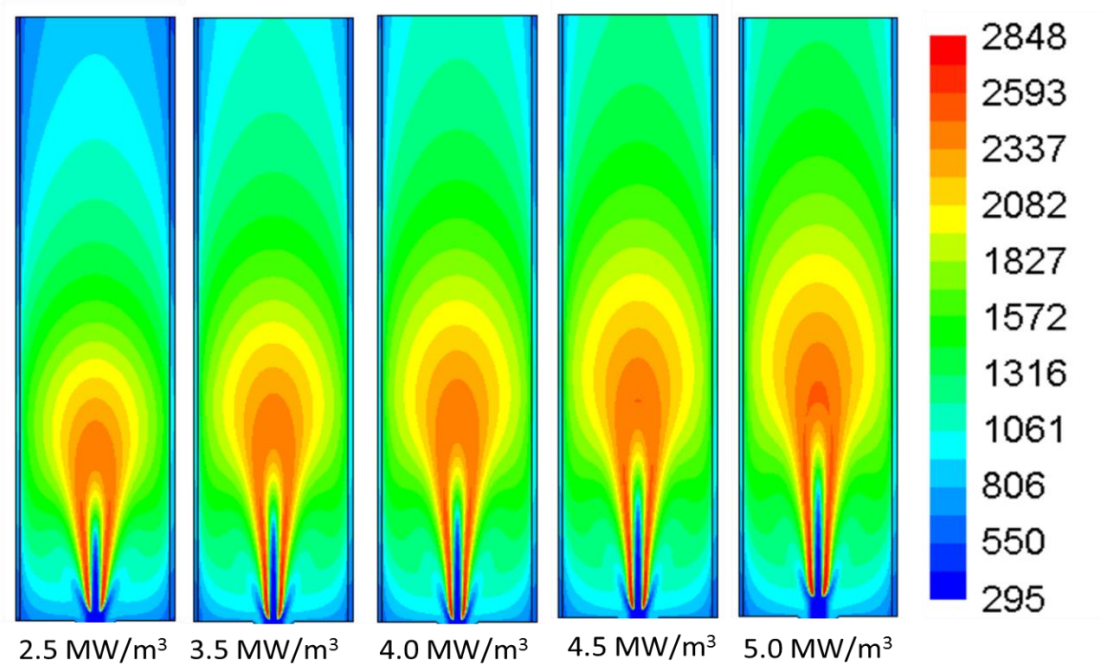

Figure 4.19: Temperature contour plots in Kelvin for 40% CO_2 in CO_2/O_2 oxidizer stream at different combustor firing rates

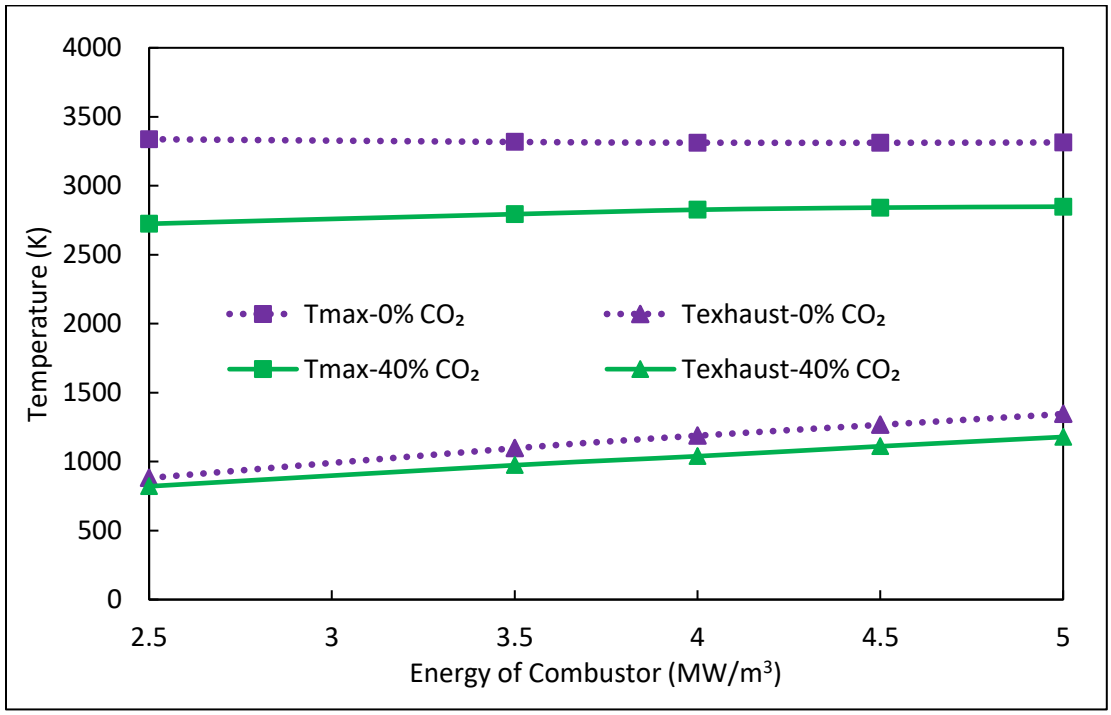

Figure 4.20: Maximum Temperature and Temperature at exhaust for 0% CO_2 and 40% CO_2

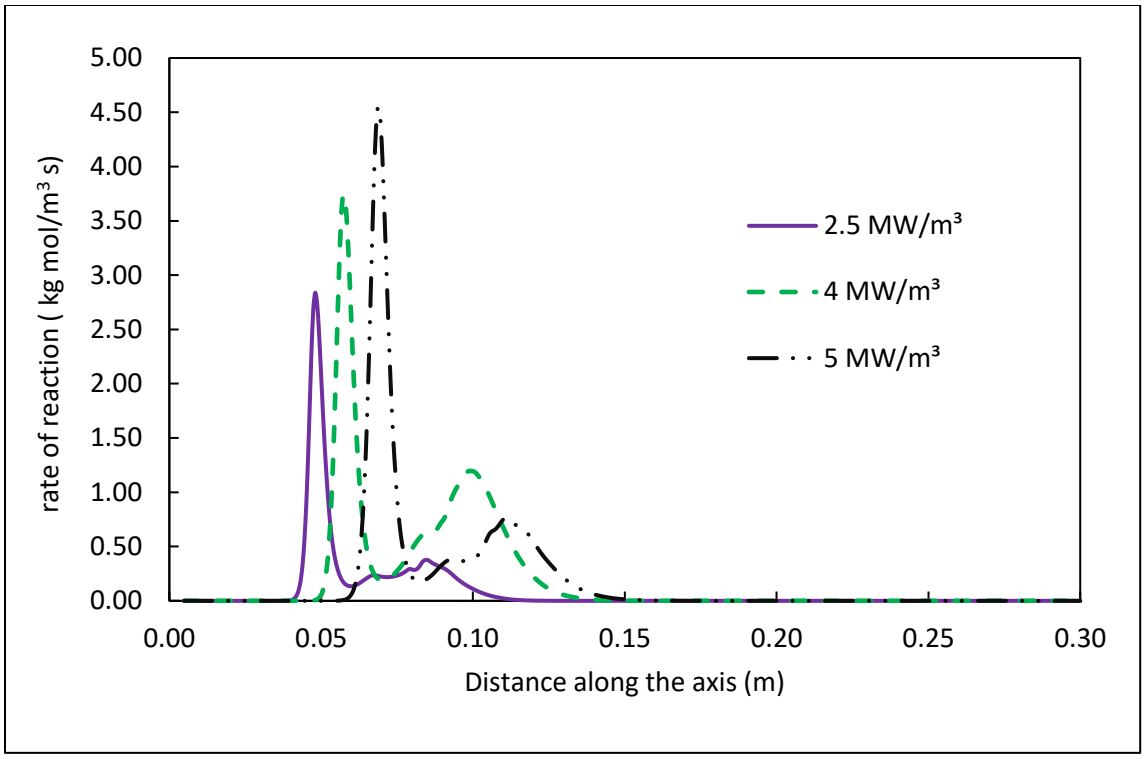

Figure 4.21: Kinetic rate of reaction-1 for different energy levels of the combustor at 40% CO_2 composition

The increase in energy level increases the rate of consumption of CH_4 inside the combustion. Figure 4.21 shows the rate of reaction for different energy levels of the combustor at 40% CO_2 in the CO_2/O_2 oxidizer mixture. However, the increased reaction rate does not lead to an increase in the maximum temperature inside the combustor, as was observed in the case of CO_2 variation. The maximum temperature remains almost constant with varying energy level, but the temperature at the exhaust increases. This is because the increased energy needs to be carried away from the combustor.

A significant part of the energy produced by combustion of methane is lost through radiation. Figure 4.22 shows the radiation fraction of the heat loss by flame. It can be seen that as the Energy level increases the radiation fraction decreases. This is because of increase in mass flow rate through the combustor, wherein more mass of gases is available inside the combustor to carry heat away from the flame. This is reflected in Figure 4.20 where the exhaust temperature is shown to increase with an increase in Energy level. Thus, maintaining the energy balance.

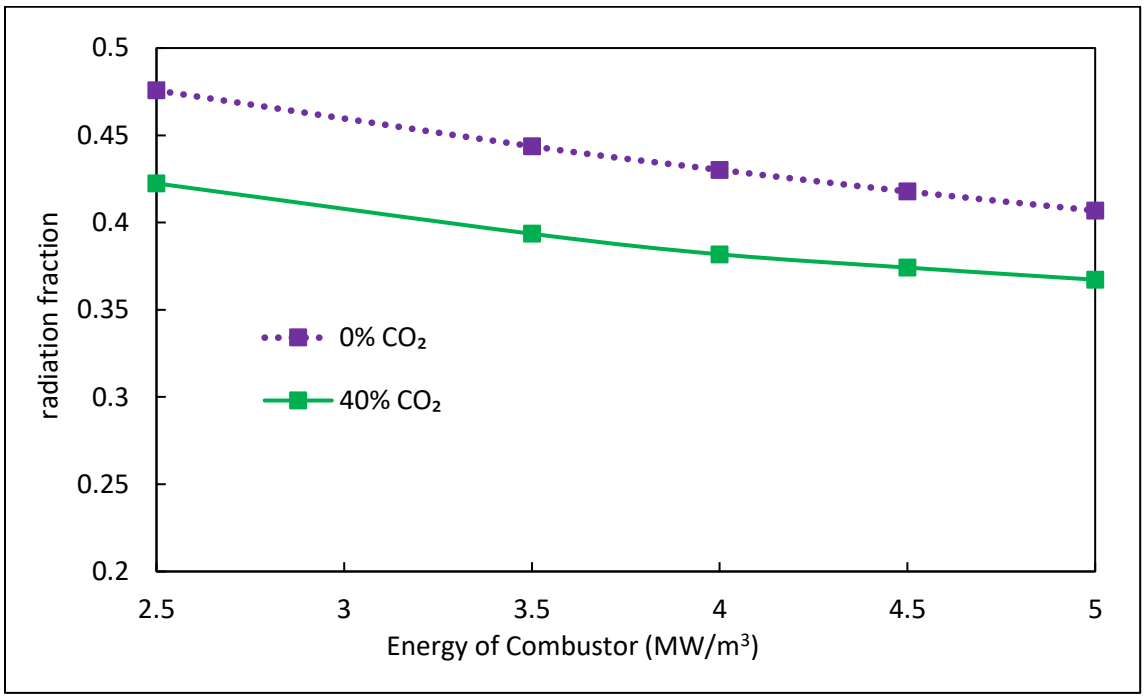

Figure 4.22: Radiation fraction vs Energy of Combustor at stoichiometry

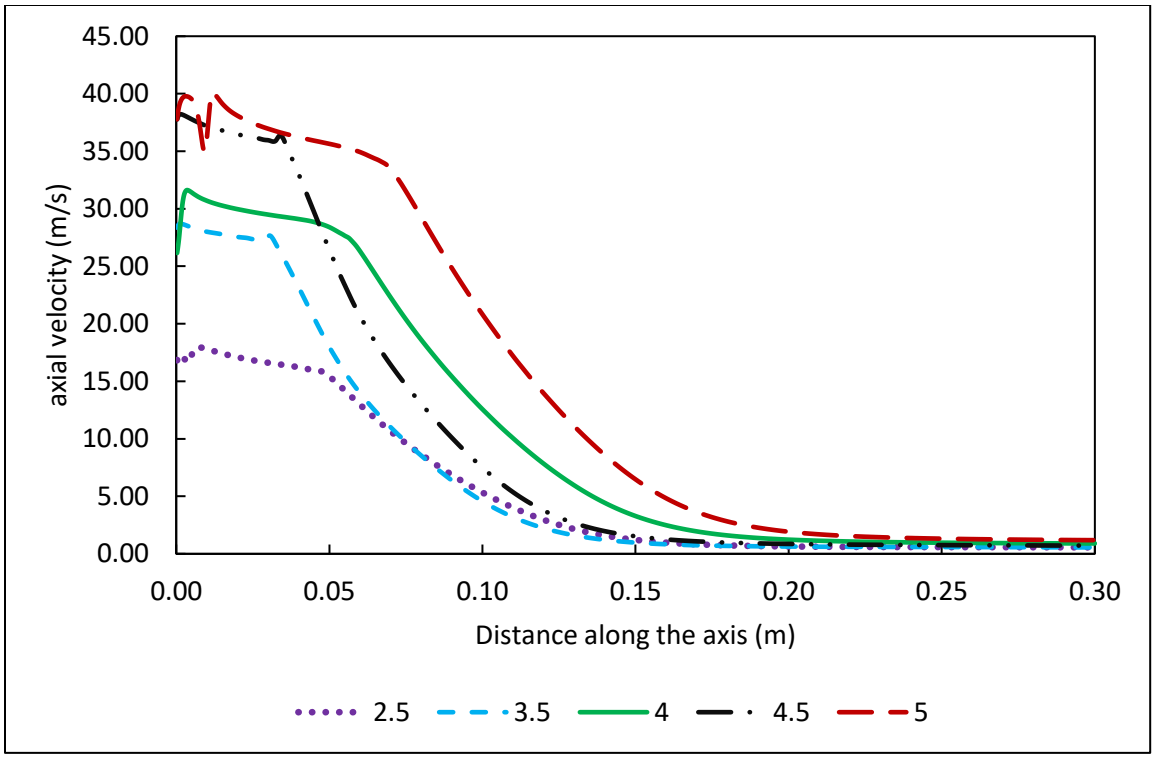

Figure 4.23: Axial velocity along the axis of the combustor at different energy level (MW/m^3) for 40% CO_2

Figure 4.23 shows the axial velocity along the combustor axis for different energy levels. As the energy level increases higher temperature distribution inside the combustor is obtained which compounded with increased mass flow rates inside the combustor leads to an increased expansion of gases. This increase in the volume of gases leads to higher velocity at higher energy level inside the combustor. After the flame, near the combustor exit, the velocity is reduced as the temperature decreases.

Figure 4.24 shows the CO emission from the exhaust of the combustor with varying energy level. The increased temperature improves the burning efficiency of the CO produced inside the combustor thus leading to a reduction in CO that is obtained at the exhaust of the combustor. The decrease in CO emission is not very significant in the case of 0% CO_2,

however, for the case of 40% CO_2, there is a decrease of nearly 50% in CO emission when moving from energy level of 4 MW/m^3 to 5 MW/m^3. Thus, suggesting enhanced combustion or burning of CO.

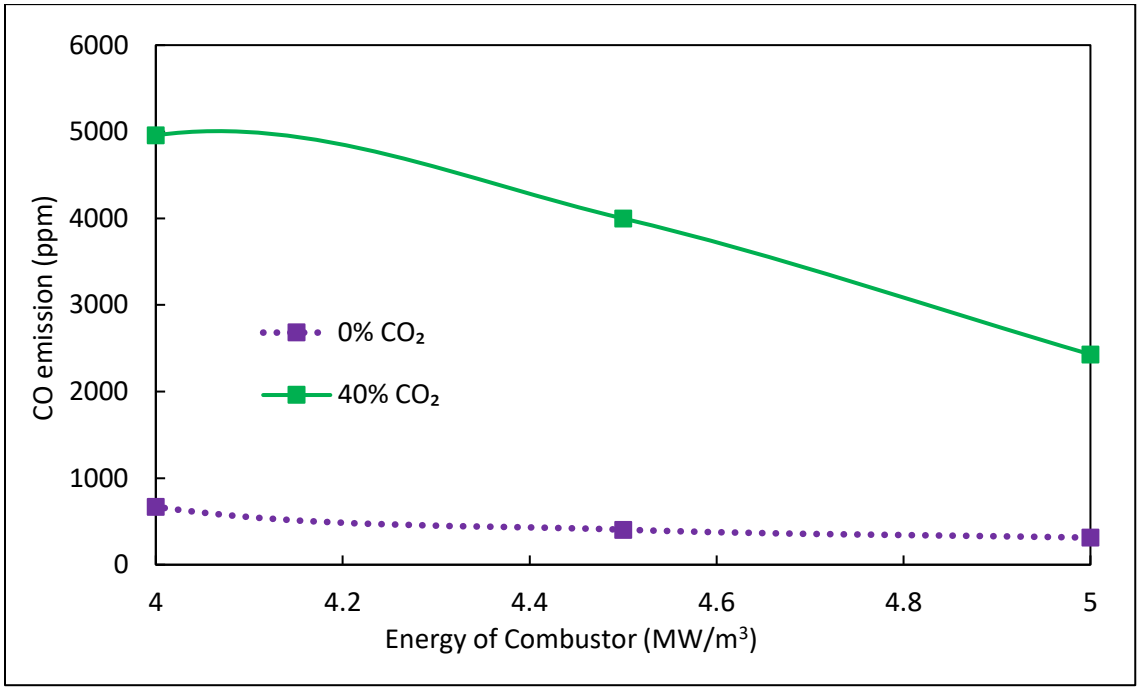

Figure 4.24: CO emission vs Energy of combustor at stoichiometry

4.9 Effect of Equivalence ratio

In this section, the effect of adding excess oxygen, in the oxidizer stream is studied. Results pertaining to 0% and 40% CO_2 at a combustor energy level of 4.0 MW/m^3 is presented. The mass of the CO_2 varies correspondingly with O_2, i.e. with excess oxygen in the oxidizer stream, excess CO_2 is also added to maintain a constant CO_2 composition in volume fraction at 40%. Figure 4.25 shows the experimental flame picture along with numerical temperature contour inside the combustor at a fixed CO_2 composition of 40% in the

oxidizer and varying equivalence ratio. Since our interest is in conserving the oxygen that is obtained after spending a significant amount of energy in the air separation unit, equivalence ratio close to stoichiometry on the lean side is examined. Equivalence ratio on the rich side will only increase the fuel wastage, hence for the present study, equivalence ratio between 0.8-1.0 is examined.

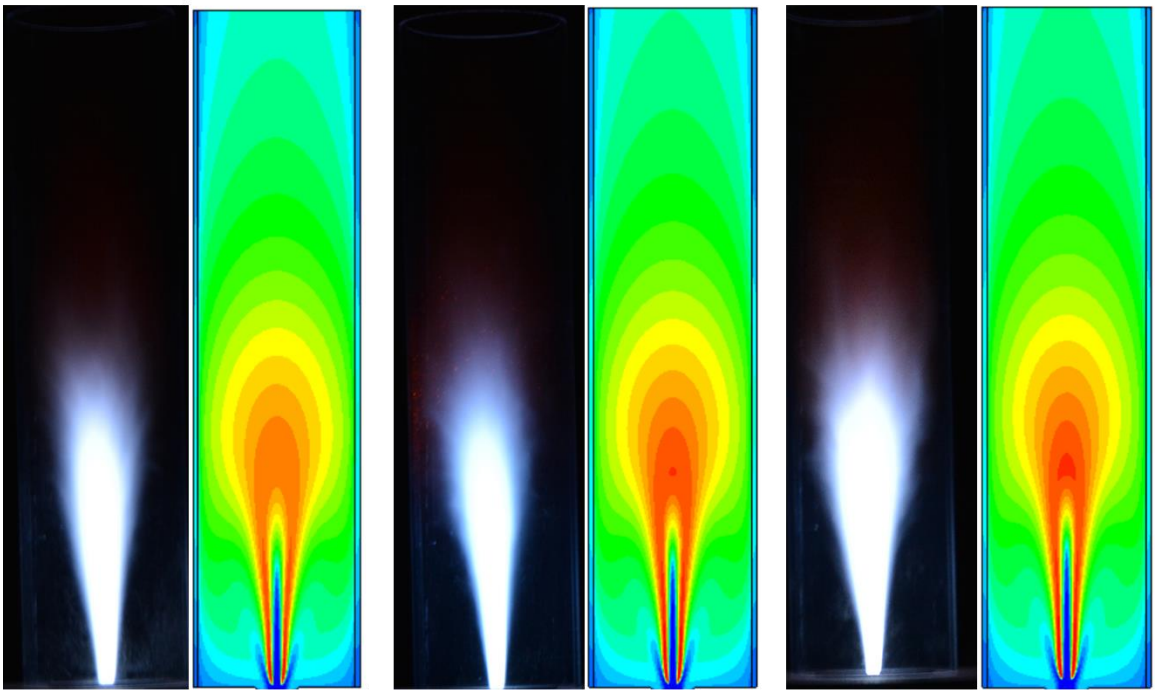

Figure 4.25: Experimental flame picture and numerical temperature contour at fixed CO_2 composition of 40% and varying equivalence ratio

From Figure 4.25 it can be seen that there is no significant difference in the flame or the temperature contour at any of the equivalence ratio. The temperature distribution within the combustor remains similar. Figure 4.26 shows the maximum flame temperature and the temperature at the exhaust of the combustor.

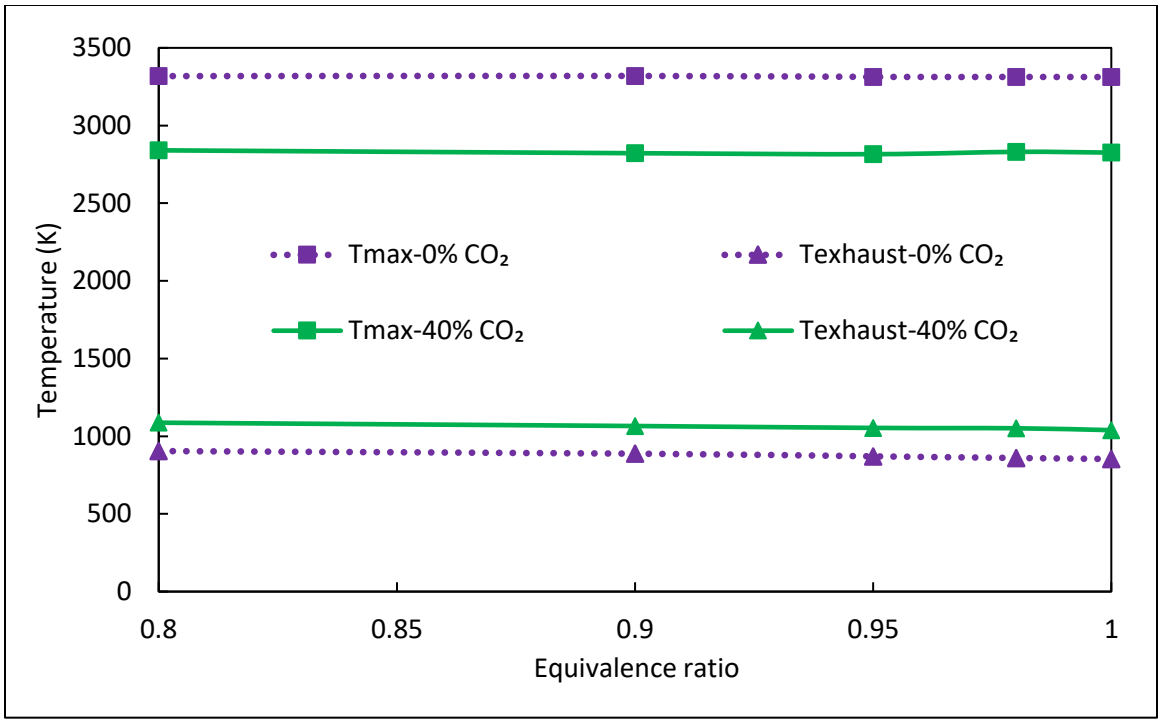

Figure 4.26: Maximum flame temperature and temperature at exhaust at different equivalence ratio

It can be seen that there is a very small increase in the temperatures at the exhaust and the maximum flame temperature with decrease in equivalence ratio. When the excess mass is added to any system, it is expected to lower the temperature. This behaviour of the gases at the exhaust to have an almost constant temperature despite the addition of excess O_2 could be because of reduction in radiation fraction of the flame.

Figure 4.27 shows the radiation fraction of heat loss from the flame. The radiation fraction decreases as the combustion is made leaner. The excess mass in the system picks up more amount of heat from the flame itself and carries out the heat. Consequently, the radiation fraction decreases of the heat loss from the flame decrease with a decrease in equivalence ratio, while the temperature at the exit of the combustor and the maximum flame temperature remains almost constant.

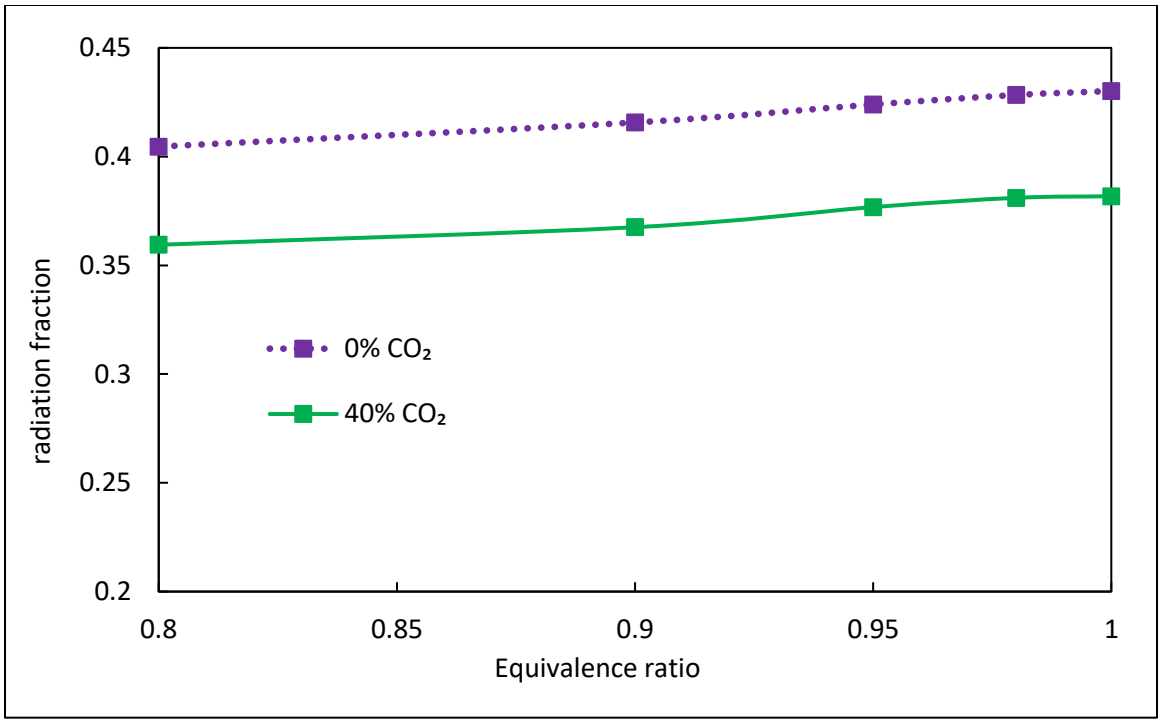

Figure 4.27: Radiation fraction of energy with varying equivalence ratio

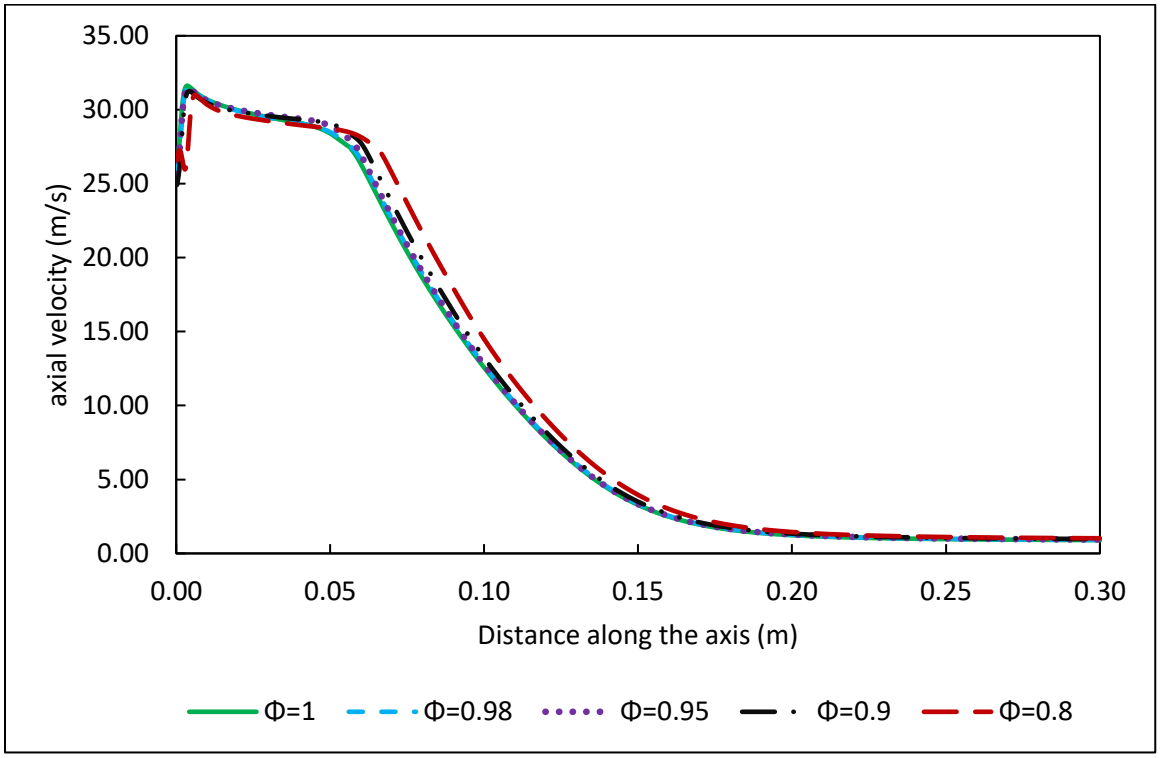

Figure 4.28: Axial velocity along the combustor axis at different equivalence ratio for 40% CO_2

Figure 4.28 shows the axial velocity of the gases along the combustor axis. There is a very small difference in the axial velocity with change in the equivalence ratio.

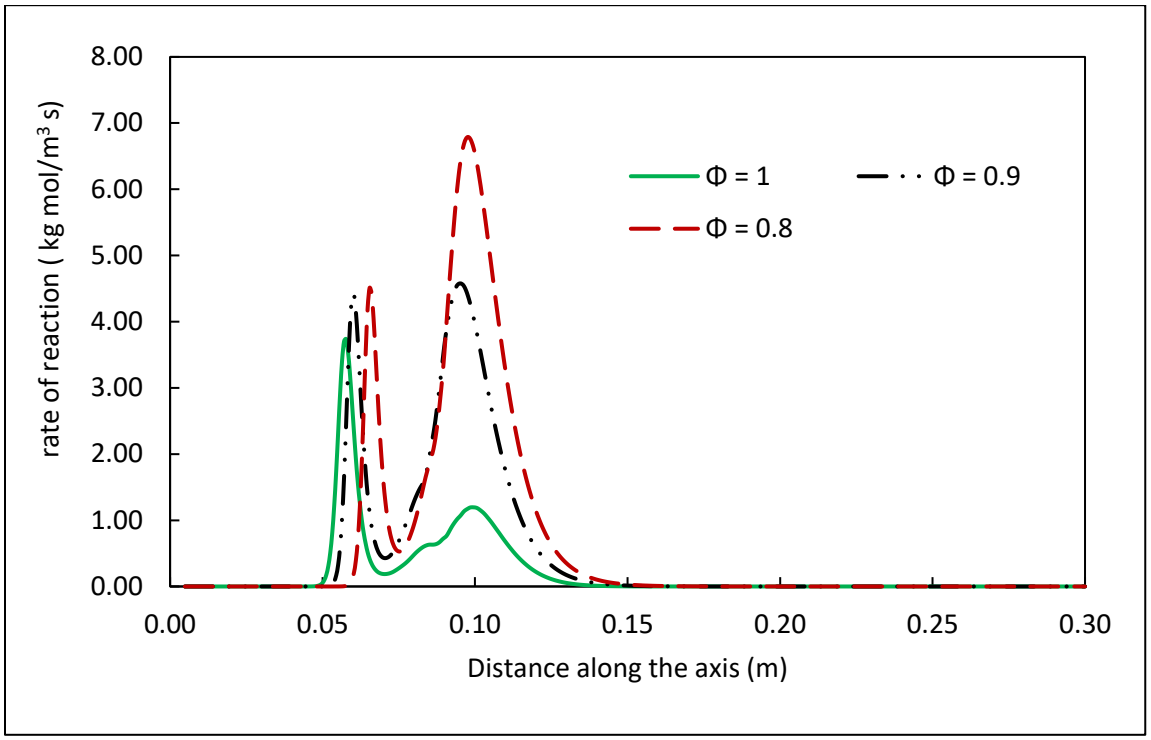

Figure 4.29: Kinetic rate of reaction-1(Table *2.2*) at different equivalence ratio for 40% CO_2

Figure 4.29 shows the kinetic rate of reaction of methane with O_2 (reaction-1, Table *2.2*). The decrease in equivalence ratio increases the combustion intensity of methane. It can be seen from Figure 4.29 that as the equivalence ratio decreases the second peak of the graph increases, while the first peak remains the same. The presence of excess oxygen in the oxidizer stream increases the intensity of combustion of methane.

The increased intensity results in an increased production of CO by reaction-1, which can be seen in Figure 4.30. Below 0.98 equivalence ratio, the CO emission continues to increase, though the increase is very small.

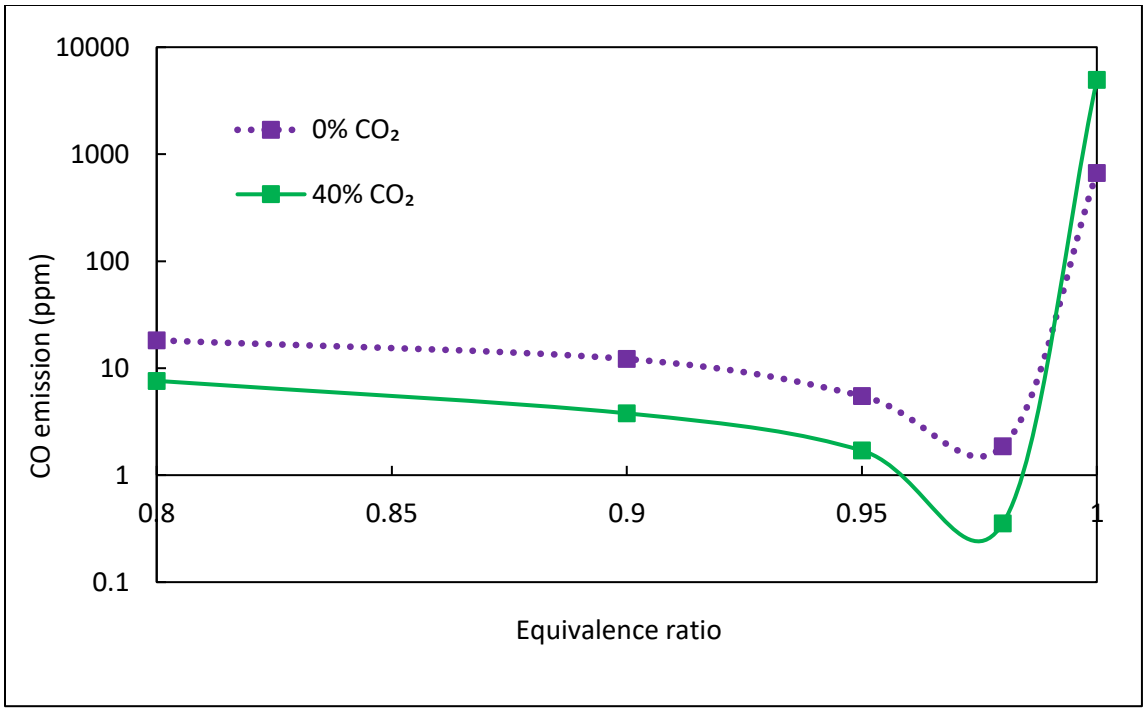

Figure 4.30: CO emission at the exhaust, at different equivalence ratio

From Figure 4.30 one can also note the drastic decrease in CO emission from Φ=1 to Φ=0.98. This decrease can be attributed to the presence of excess O_2 in the oxidizer. Due to which the CO_2 in reaction-5 is no more able to hinder the oxidation of CO, and hence a better combustion of methane is obtained at Φ=0.98 equivalence ratio. Another interesting point is the less CO emission at 40% CO_2 than at 0% CO_2 below Φ=0.98. This can be attributed to the increased mass flow within the system at 40% CO_2, which enhances the mixing and improves the combustion, resulting in lower CO emission.

CHAPTER 5

BURNER-HEAD DESIGN

In the previous chapter, it has been shown that the design of the burner head reduced the swirl angle of the flow at the fuel inlet plane from 45° to 2-3° (Figure 4.18). Thus, there is a need to improve the design so that a more efficient mixing within the combustor can be established. This section aims at studying different design and design parameters that might improve the swirling action of the flow.

5.1 Effect of increase of inlet diameter of the burner head

The burner head which is located after the swirler in order to increase the velocity of the flow. The inlet diameter of the burner head in studies conducted in previous chapters has been fixed at 10 mm. The flow coming from the swirler is obstructed by the burner head and has to change direction before arriving at the inlet of the burner head, which resulted in a decrease in the swirling effect of the flow. Figure 5.1 shows the original design of the burner head that has been used in studies reported in previous chapters.

In this section, the effect of increasing the diameter of the burner head is examined. The diameters studied are 10, 16, 20, 25, 27, 30 and 40 mm. It should be noted that when the flow from the swirler is obstructed by the burner head due to which burner head is slightly lifted to make way for the flow to pass through and the height of lift for the burner head varies with the velocity and the mass flow rate of the oxidizer. However, it is difficult to

determine the lift height and in numerical it is assumed that the lifted height is of 1 mm. As soon as the diameter of the inlet becomes such that there is a natural path for the flow to take place, without lifting the burner head, it is assumed that burner head does not lift off, and the entire flow is able to pass through whatever small opening is available for the fluid to enter the burner head.

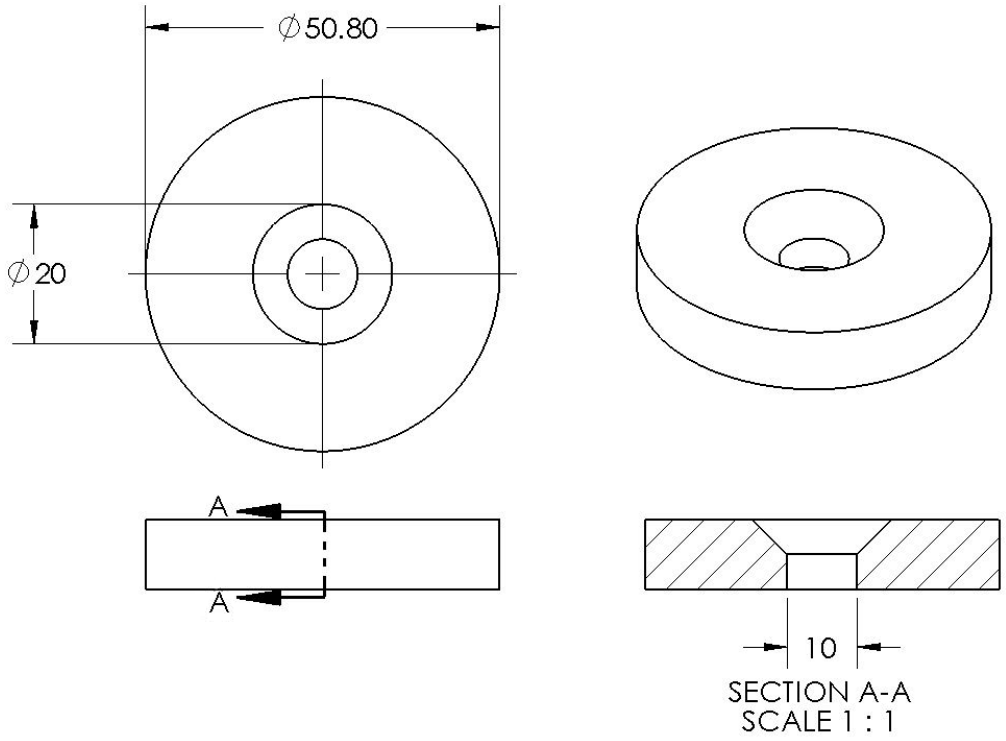

Figure 5.1: Original design of burner head

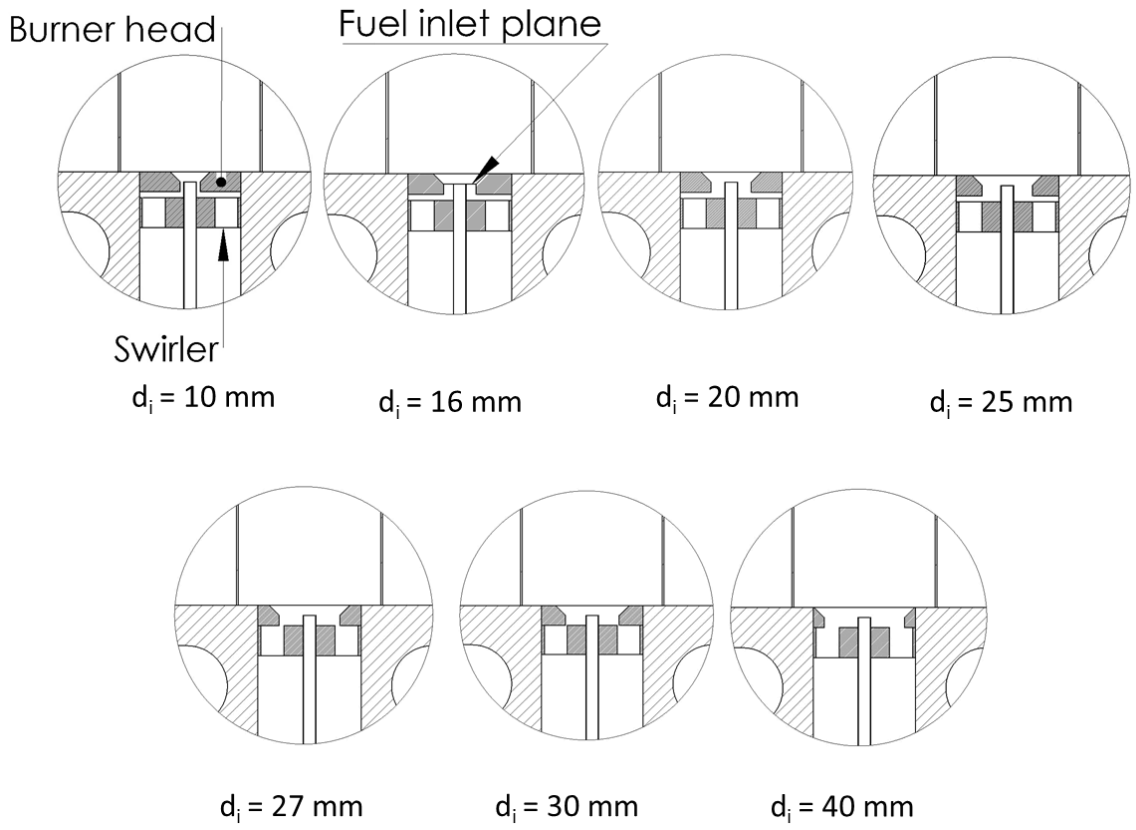

Figure 5.2: Detailed view of the burner head and swirler configuration before the combustor

Figure 5.2 shows the detailed view of the burner head and the swirler placement before the combustor. It can be seen that the burner head is slightly lifted (by 1mm) for cases with an inlet diameter of the burner head less than the diameter of the central body of the swirler (≤25 mm).

The study to examine the effect of increase in the inlet diameter of the burner head is carried out using a swirler of vane angle 45° (inlet boundary condition of the flow) at a fuel energy level of 4 MW/m^3, for stoichiometric conditions, while also maintaining 40% CO_2 in the CO_2/O_2 oxidizer mixture. Figure 5.3 shows the mass weighted axial and swirl velocities at the fuel inlet plane. In the figure, the axial component of the flow is represented by V_{axial}

and the tangential or the swirling component is represented by V_θ. It can be seen that as the diameter of the inlet to the burner head is increased the axial velocity decreases, but the swirl component of the flow remains almost the same until 25 mm. The swirler central body diameter is 25 mm. As the inlet to the burner head is increased the obstruction to the flow is removed and the flow easily enters the burner head. A sudden spike in the swirl velocity is seen beyond 25mm diameter, which then decreases with increase in diameter of the inlet to burner head. Figure 5.4 shows the flow swirl angle at the fuel inlet plane with varying diameter of the burner head inlet. The swirl angle is calculated using Equ. (4.2).

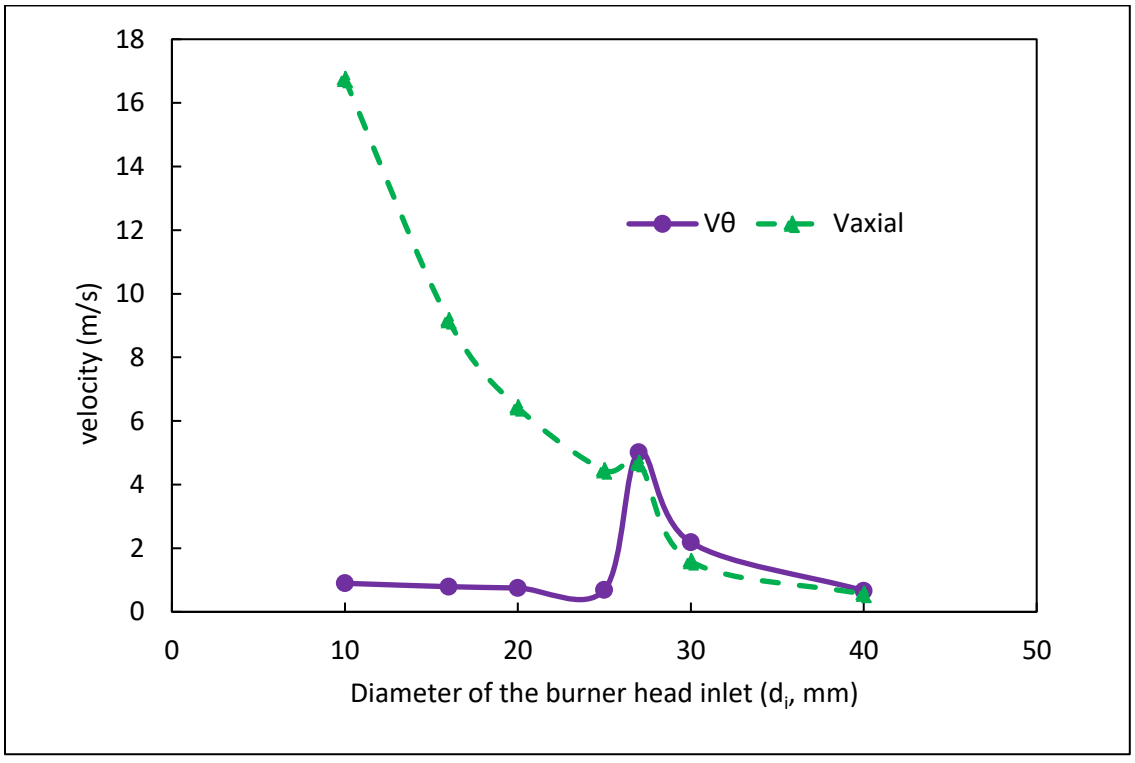

Figure 5.3: Mass-weighted average axial and swirl velocity at the fuel inlet plane

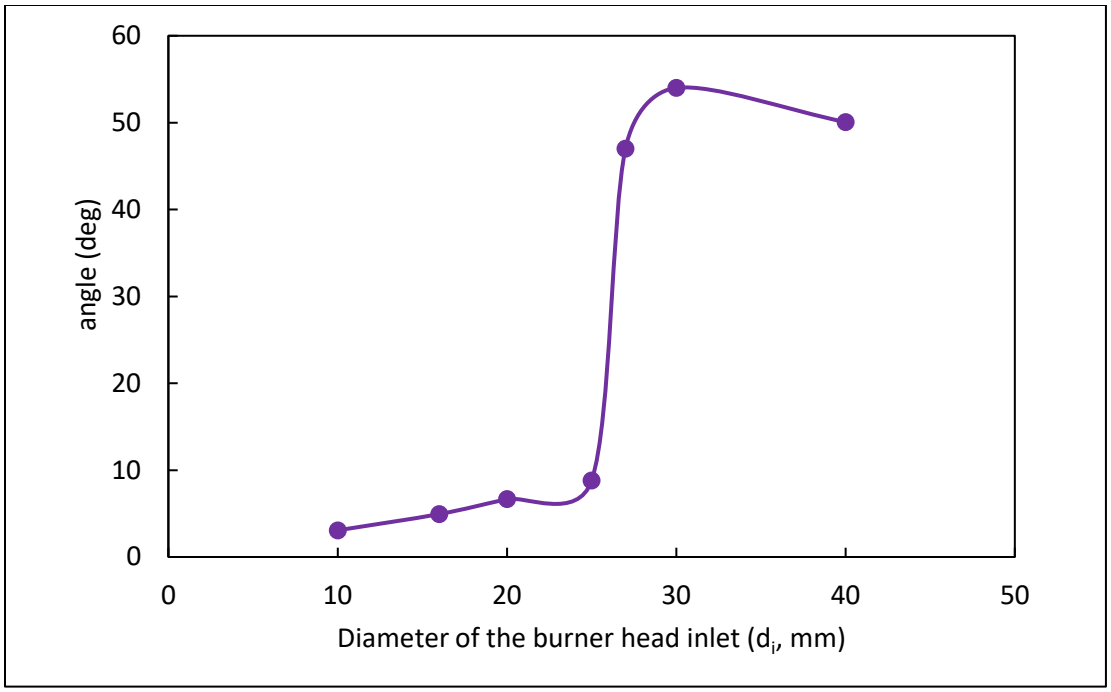

Figure 5.4: Variation in swirl angle at the fuel inlet plane for different diameters of the burner head inlet

It can be seen that as the diameter is increased from 10 mm the swirl angle at the fuel inlet plane increases slightly until a diameter of 25 mm, which is also the diameter of the swirler central body. Beyond 25 mm there is a drastic increase in the swirl angle reaching above 45°, which is the swirler vane angle. This increase in swirl angle beyond the swirler vane angle is because of the expansion that immediately starts after the fuel plane angle. The increased cross-section beyond the fuel plane angle decreases the axial velocity, due to which the swirl angle increases.

Another way to quantify the swirl at the fuel inlet plane is by using the Swirl Number. It is a non-dimensional number used to characterise the degree of the swirl. It can be defined as [110],

$$S = \frac{G/2}{1-(G/2)^2} \tag{5.1}$$

Where,

$$G = \frac{V_{tangential}}{V_{axial}} \tag{5.2}$$

An alternative way to calculate the swirl number for flow through a swirler involves the use of the hub diameter or the centre body diameter of the swirler and the diameter of the swirler, and is given as [110],

$$S = \frac{2}{3}\left[\frac{(1-(d_h/d)^3)}{1-(d_h/d)^2}\right]\tan\phi \tag{5.3}$$

Where, "d_h" is the diameter of the central hub of the swirler, which is 25 mm, "d" is the diameter of the swirler which is 50.8 mm and "ϕ" is the vane angle of the swirler. This leads to a Swirl number value of 0.774, coming out from the swirler.

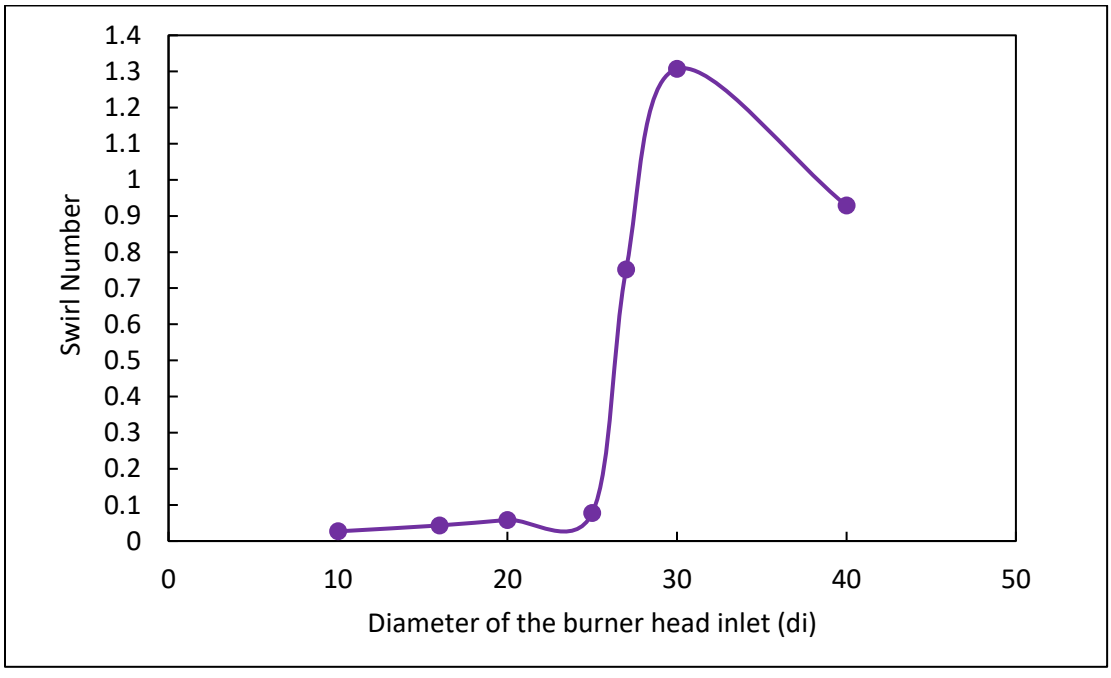

Figure 5.5: Swirl Number variance with increase in inlet diameter of burner head

Figure 5.5 shows the variance of swirl number with increase in inlet diameter of the burner head. A similar trend as seen in Figure 5.4 can be observed. A value of 0.75 is obtained for the swirl number at a diameter of 27mm which is closest to the swirl number of 0.774 that is obtained from the swirler.

Figure 5.6 shows the temperature contour plot for different diameters of the burner head inlet.

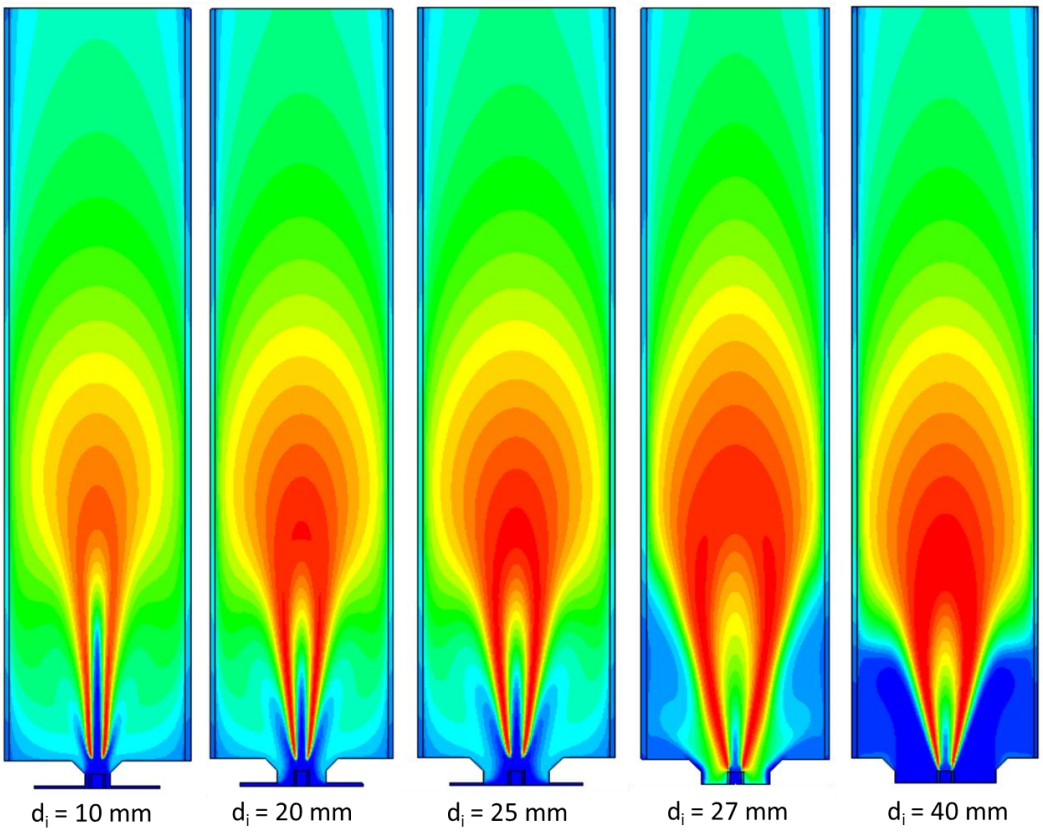

Figure 5.6: Temperature contour of the combustor for different inlet diameters of the burner head

For the cases where the diameter of the burner head inlet is lower than 25mm, the temperature contour plot appears to be similar. But as the diameter of the burner head inlet is increased beyond 25 mm a cool zone can be observed near the combustor inlet, this

cooler zone is more pronounced with a diameter of 40cm. This is due to the existence of a recirculation zone near the burner head. One can also notice the difference in the way the flame is attached to the fuel nozzle below and beyond 25 mm diameter. Figure 5.7 shows the streamlines for the flow with different inlet diameters of the burner head.

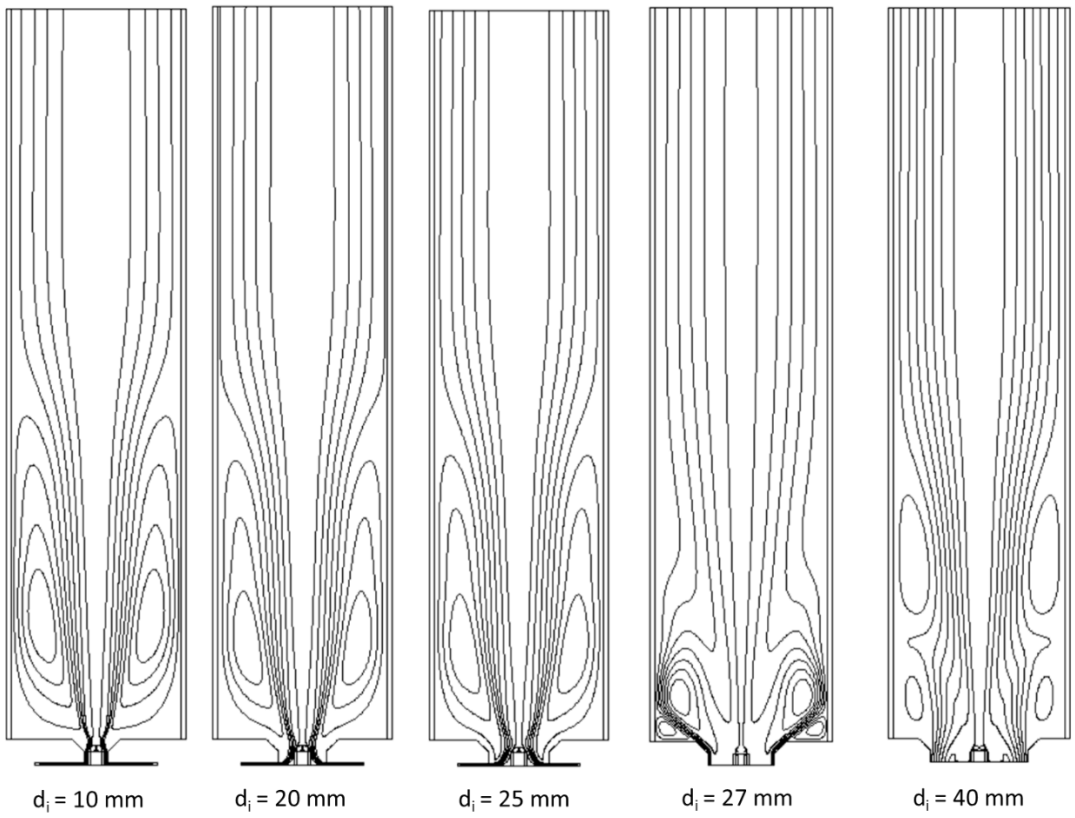

Figure 5.7: Streamlines of the flow through the combustor with different inlet diameters of the burner head

For the cases with diameters below 25 cm, the streamlines remain same. There is a single recirculation zone near the combustor entrance. The flow from the swirler moves towards the fuel pipe before entering into the combustor. This is due to the presence of radial velocity, which is a result of the flow from the swirler changing directions to find a path to travel. Beyond 25 cm the flow structure changes drastically. The flow seems to be more

concentrated towards the inner walls of the burner head, rather than being concentrated at the fuel pipe. Since the flow does not have to change directions anymore the radial component of the flow is reduced resulting in more flow near the inner walls of the burner head. As a result, the strain rate of the flame is low and the flame seems to be attached to the fuel nozzle (Figure 5.6). While a slightly lifted flame from the nozzle is observed for cases below 25 cm diameter of the burner head inlet.

For cases of 30 cm, two recirculation zones can be observed, an inner recirculation zone (IRZ) and an outer recirculation zone (ORZ). For the case of 27 mm diameter, the IRZ is very close to the burner head and quite small. For the case of 40 mm diameter the size of the IRZ increases and ORZ disappears and instead another recirculation zone appears along the combustor wall. This is due to the decrease in the expansion experienced by the flow entering the combustor. For the case of 40 mm, the expansion is very small when the flow enters the combustion chamber.

5.2 New Burner Head Design

In this section, we try to design a new burner head which directs the incoming flow from the swirler in such a manner that the flow retains its swirl number and enters the combustor close to the fuel nozzle, thus providing accelerated flow near the fuel nozzle. The design can be seen in Figure 5.8. A design study was carried out to optimise the design of the burner head in order to have a good swirl flow. Different parameters of the burner head were modified and its effect on the swirl number at the fuel inlet plane was studied. The study was carried out for a combustor operating at 4 MW/m^3-bar, with the CO_2/O_2 composition of 40/60, and a swirler of 45° vane angle. The inlet diameter of the burner

head was varied along with the neck length of the burner head. The positioning of the fuel pipe was also changed to see its effect on the swirl number at the fuel inlet plane. Figure 5.8 and Figure 5.9 shows the design of the burner head.

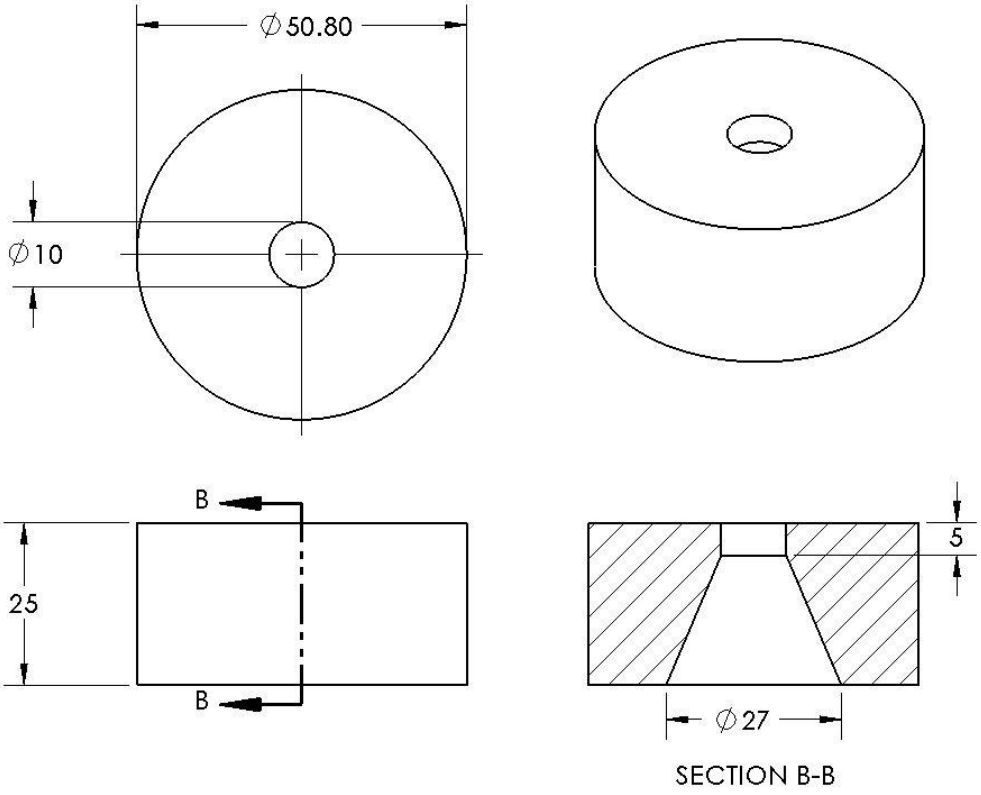

Figure 5.8: Design of New Burner Head (Dimensions in mm)

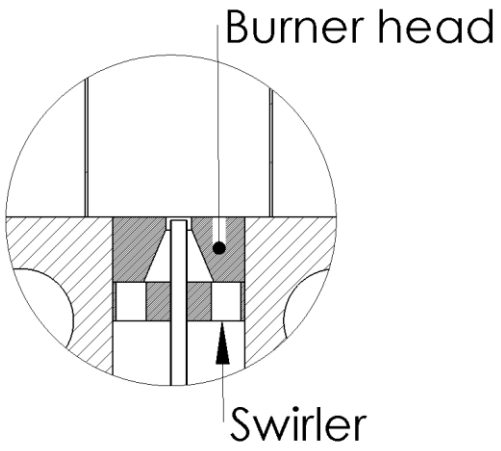

Figure 5.9: Detailed view of the new burner head setup

5.2.1 Effect of inlet diameter

For the new design, the effect of inlet diameter of the burner head was studied while keeping the neck length at 5 mm and the fuel pipe positioned in such a way that the fuel inlet lies 3mm below the dump plane (inlet to the combustor). Figure 5.10 shows the axial and tangential velocity at the fuel inlet plane. While the axial velocity remains the same with increasing diameter the swirl velocity decreases resulting in a decreased swirl flow at the fuel inlet plane. This can be seen in Figure 5.11, where the most optimum swirl number is obtained at a diameter of 27 mm for the burner head. Beyond 27 mm the swirl number continues to decrease. Thus suggesting 27 mm to be the optimum diameter for the burner head inlet.

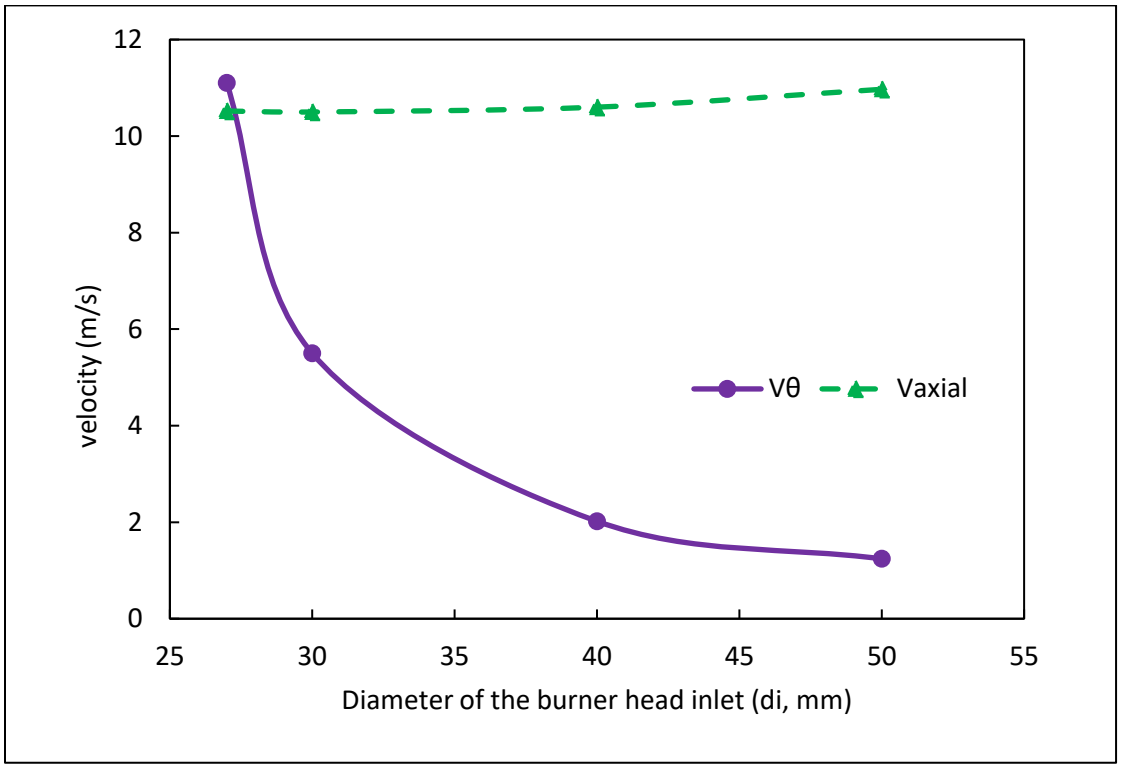

Figure 5.10: Axial and tangential velocity at the fuel inlet plane with changing burner head inlet diameter

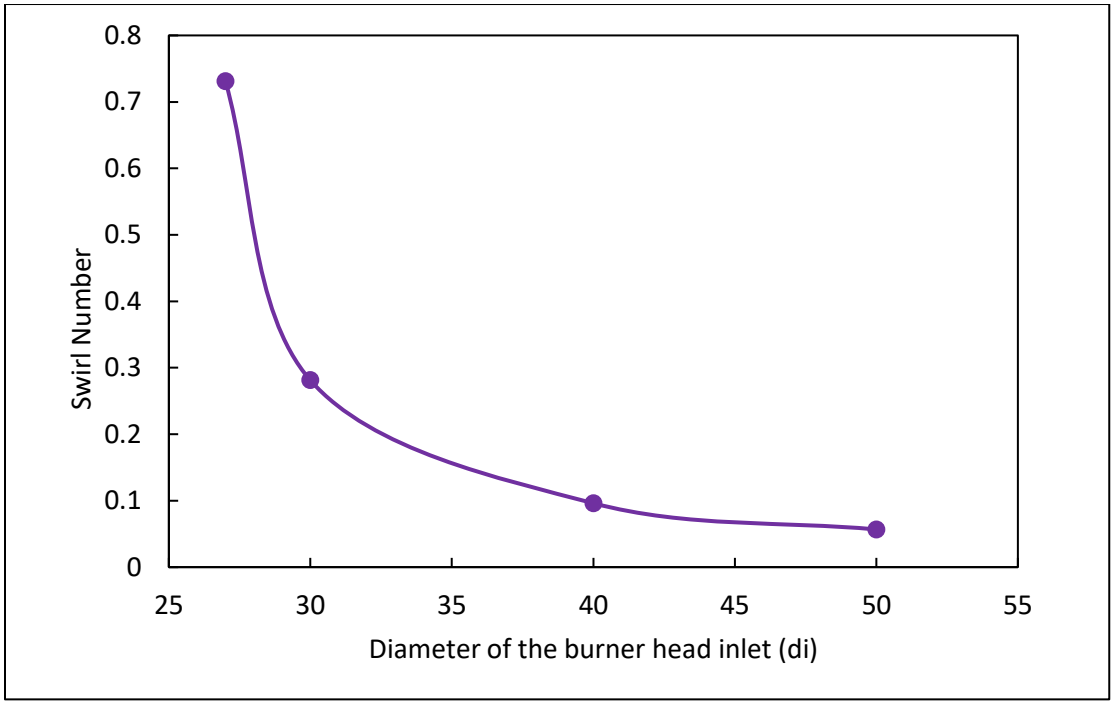

Figure 5.11: Swirl number variance with inlet diameter (new burner head)

5.2.2 Effect of Neck Length

Neck length corresponds to the small throat at the exit of the diameter which is made vertical to allow for a uniform flow at the inlet of the combustor. Figure 5.12 shows the variation in axial and tangential velocity at the fuel inlet plane with an inlet diameter of 27 mm and the fuel pipe positioned 3 mm below the dump plane. It can be seen that the elimination of the neck causes a sudden expansion near the fuel inlet plane, as a result of which the axial velocity decreases resulting in a high swirl flow. As the neck length is increased from 0 to 3 the axial velocity and the tangential velocity become almost same resulting in a better swirl flow. Figure 5.13 shows the swirl number as a function of neck length. The swirl number at zero neck length is very high and decreases to a value close to 0.75 at 5 mm, which is closer to the swirl number for the flow from swirler.

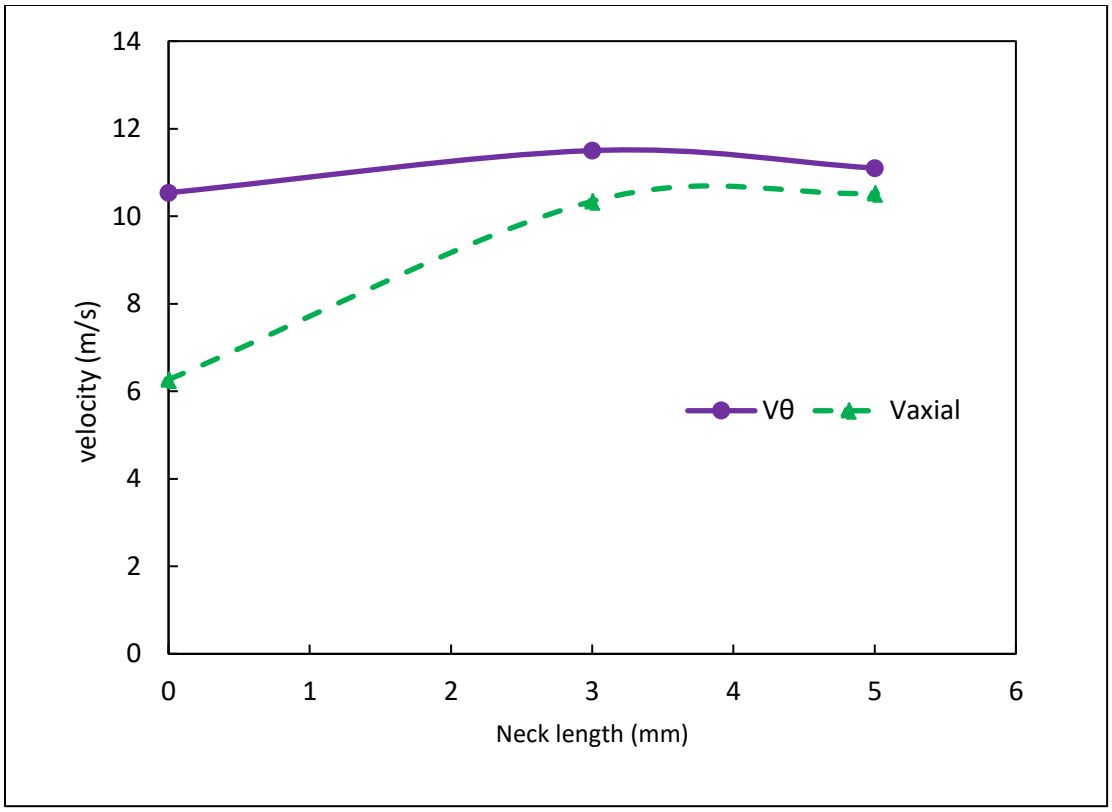

Figure 5.12: Axial and tangential velocity for different neck length of burner head

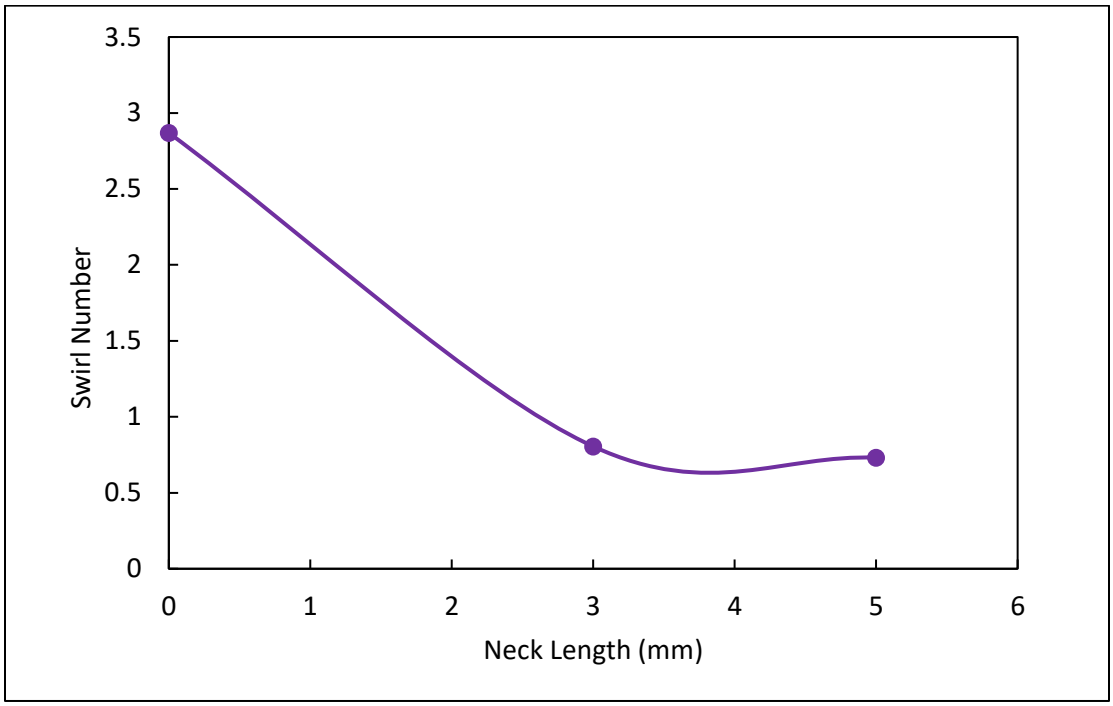

Figure 5.13: Swirl number vs the Neck length at the fuel inlet plane

5.2.3 Effect of fuel nozzle positioning

The positioning of the fuel nozzle was examined to study its effect on the swirl at the fuel inlet plane. Figure 5.14 shows the axial and tangential velocity at the fuel inlet plane while Figure 5.15 shows the swirl number at the fuel inlet plane for different positioning of the fuel nozzle. Negative values in the figure show the fuel nozzle being positioned above the dump plane inside the combustor, while the positive value shows the fuel nozzle being positioned inside the burner head below the dump plane.

It can be seen that positioning the fuel nozzle below the dump plane gives the closest swirl number (0.77) to that of flow coming from the swirler. While positioning it at the dump plane increases the swirl number increases the swirl number and positioning the fuel nozzle inside the combustor decreases the swirl number.

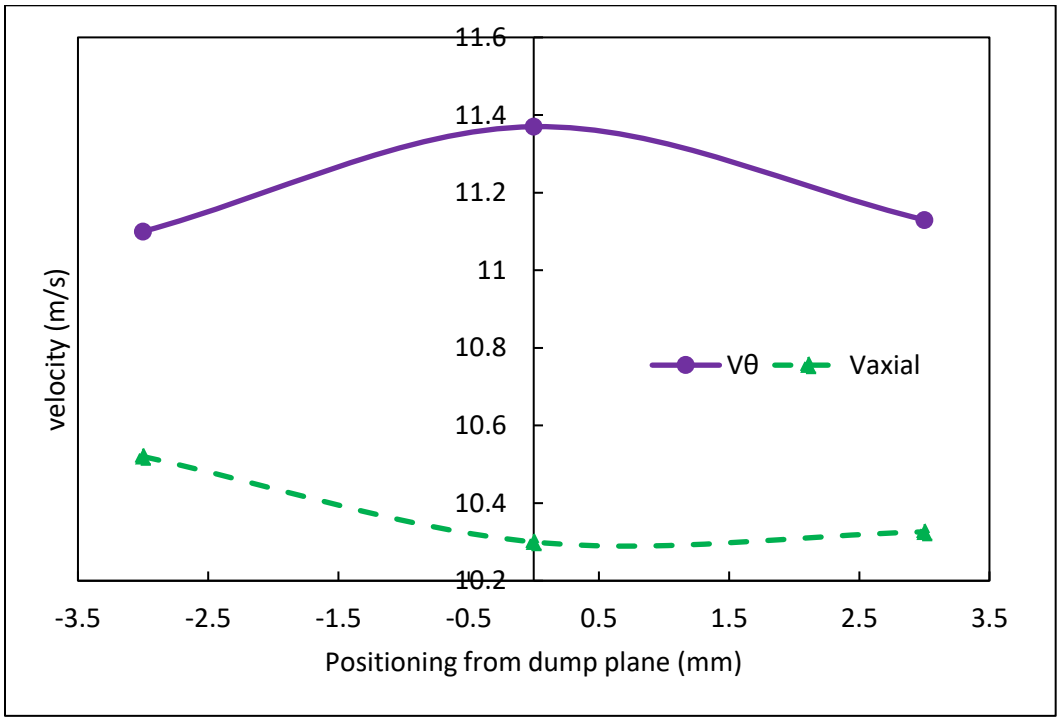

Figure 5.14: Axial and tangential velocity at the fuel inlet plane for different fuel inlet positioning

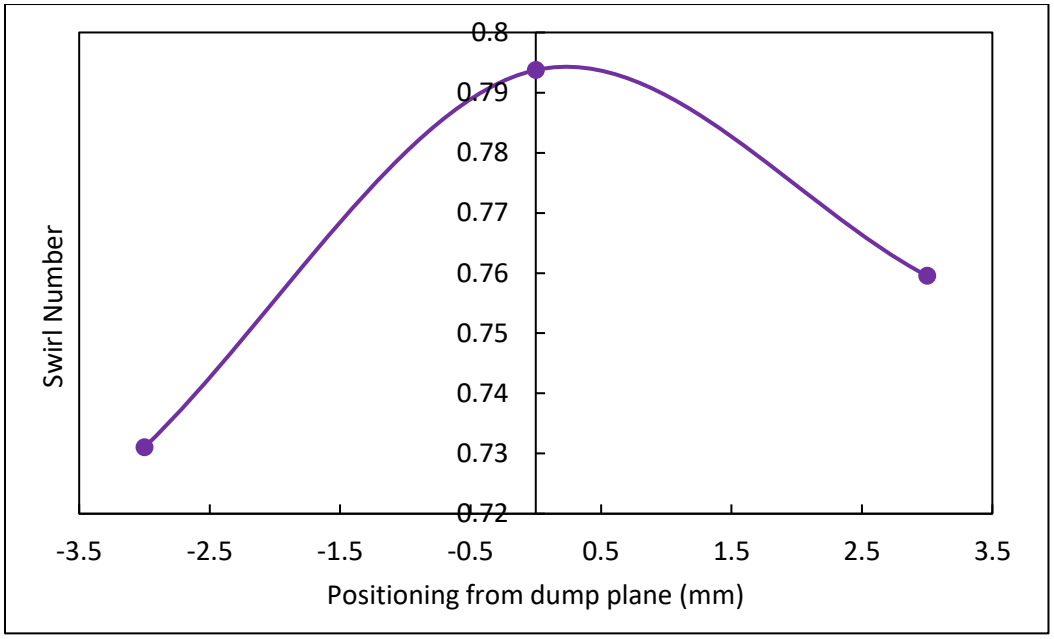

Figure 5.15: Swirl number for different positioning of fuel pipe

From above study, it can be concluded that the optimum values for different design parameters are as shown below in Table 5.1.

Table 5.1: Optimum values for various design parameters

Parameter	Optimum value
Inlet diameter of the burner head	27 mm
Neck length at the exit of burner head	5 mm
Fuel nozzle positioning	3 mm below the dump plane

5.2.4 Temperature contour and streamlines with the new Burner head

Based on the above design parameters another set of CO_2 variation study was carried out to examine the flame structure at various CO_2/O_2 composition,

Figure 5.16 shows the experimental flame picture and temperature contours of the combustor with different CO_2 percentages in the CO_2/O_2 oxidizer mixture. The combustor was operated under stoichiometric condition with a firing rate of the 4 MW/m^3, and the swirler used had a vane angle of 45°.

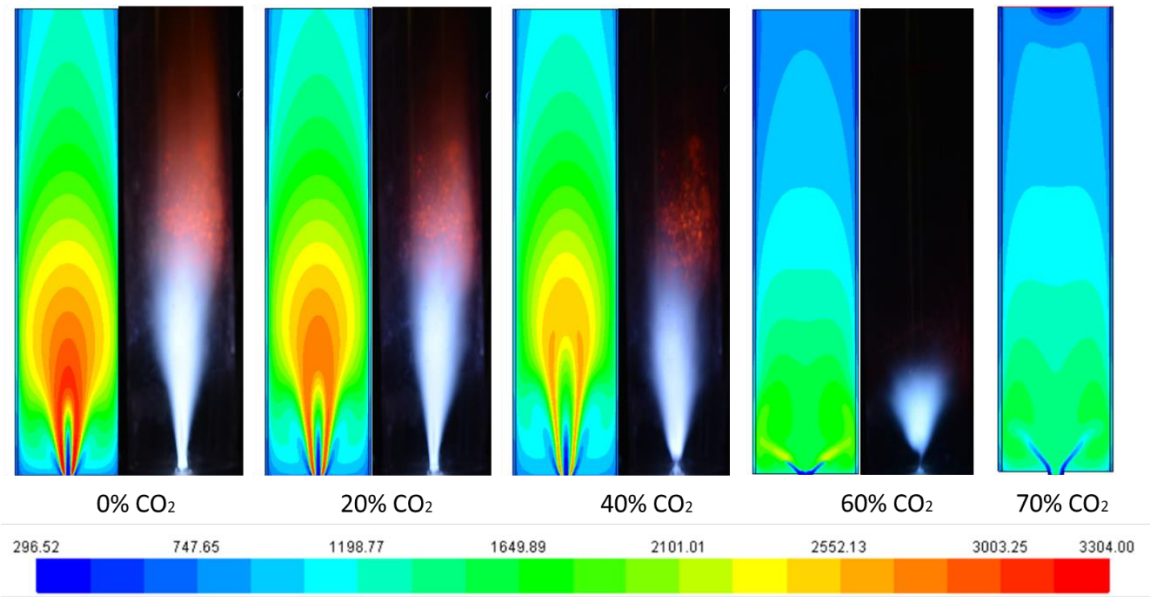

Figure 5.16: Temperature contour plot with varying CO_2 composition in the CO_2/O_2 mixture

It can be seen that the flame with 0-20 % CO_2 in the oxidizer mixture has a well attached flame structure. At 40% CO_2, the flame in the experimental image can be seen to become weak at the roots, which is attached to the fuel nozzle. This can also be seen in the numerical temperature contour, as thinning of the high temperature zone near the fuel nozzle. At 60% and 70% CO_2, the flame detaches from the fuel nozzle and stabilises at a

very small distance away from the fuel nozzle. Moreover, the shape of the flame also changes. Instead of a jet like flame, a V-shaped flame can be observed, which is also seen in numerical temperature contours.

Figure 5.17 shows the streamlines of the flow with varying CO_2 composition in the oxidizer.

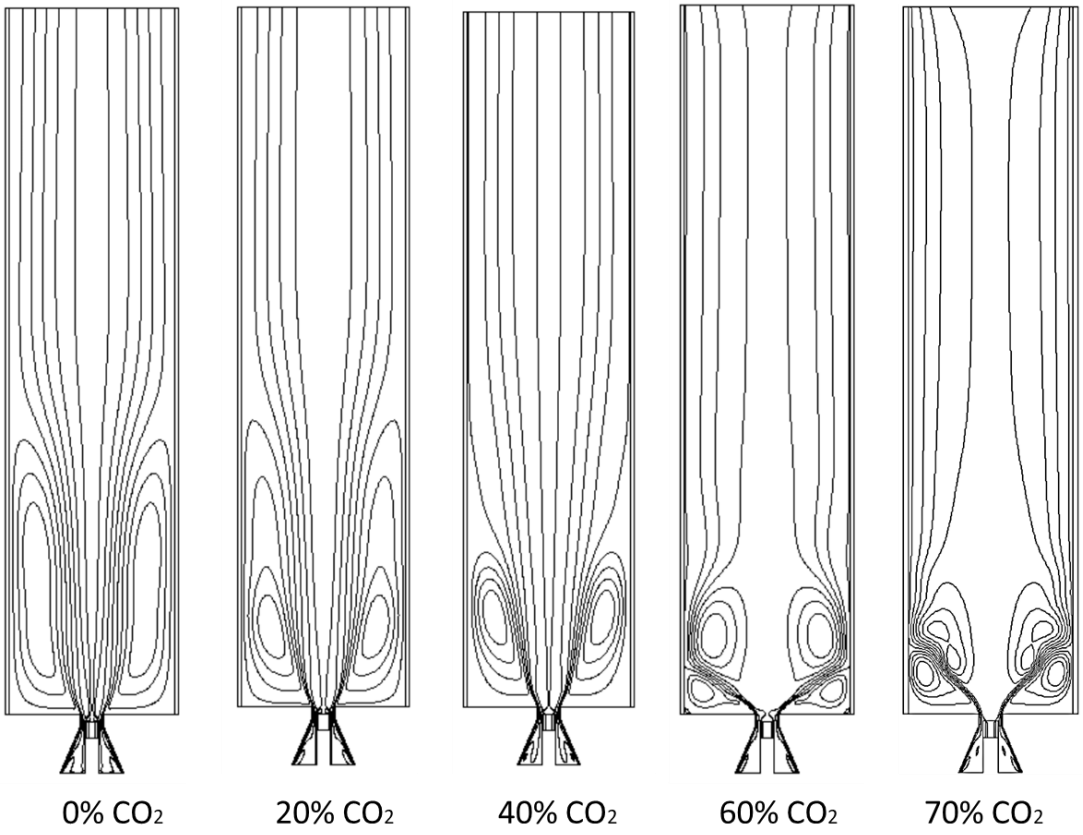

Figure 5.17: Streamlines of the flow with varying CO_2 composition in the CO_2/O_2 mixture

As the amount of CO_2 is increased the recirculation zone tends to become stronger and decreases in size for 0 to 40% CO_2. At 60% CO_2, the recirculation zone becomes very small, which leads to the development of an inner recirculation zone in the flame as can be seen in Figure 5.17. At 70% CO_2, the recirculation zone becomes stronger, and most of the

flow is concentrated close to the wall because of strong swirl flow due to higher mass flow through the system.

It should also be noted that with the new burner head no stability issues were observed numerically. When using the design of the old burner head very weak flames were observed at 70% CO_2 which extinguished at 75% CO_2 composition in the oxidizer. Numerically, no combustion occurred at 70% CO_2. However, with the design of the new burner head, the stability issues associated with combustion at high CO_2 composition in the oxidizer seems to be resolved. This enables the oxyfuel combustion of methane at 30/70 O_2/CO_2 ratio in the oxidizer to closely resemble air combustion. Thus, the use of the new burner head is recommended as it not only provides a good swirling flow but also enhances the flame stability.

CHAPTER 6

CONCLUSIONS AND RECOMMENDATIONS

6.1 Conclusions

The combustion characteristics such as temperature, stability, and emissions for a stoichiometric, oxyfuel combustion of methane in a model gas turbine combustor with transparent combustor walls have been studied experimentally and numerically. The following conclusions could be drawn from the study:

1. The flame was found to exhibit trimodal regime (i.e. Attached flame → Lifted flame → No flame), when the combustor is operated under gas turbine conditions (≥3.5 MW/m^3-bar), below which the flame exhibited bimodal regime (i.e. Attached flame → No flame). Weak flames at the nozzle exit were generally observed to precede the Attached flame → Lifted flame transition. The weak flame is due to the entrainment of more CO_2 containing oxidizer (O_2/ CO_2) to the fuel stream that reduces the flame burning rate. The Attached flame → Lifted flame transition regime was found to occur at a critical oxidizer velocity (U_{ox}). The transition regime was also found to strongly depend on the fuel composition such that fuel with higher strain resistance (such as H_2 containing fuel) similarly has higher critical U_{ox}. The leading edge of the lifted flame was observed to oscillate about different points (stabilisation points) within the combustor. These are points of lowest scalar dissipation rate where the edge flame speed balances the local flow velocity.

2. A Numerical model has been developed and validated using experimental data. The modified Westbrook-Dryer (WD) and the modified Jones-Lindstedt mechanisms (JL5) were found to be close in prediction of the temperature distribution. However, the temperature distribution was found to be dependent on the type of Weighted Sum of Grey Gas (WSGG) model. The parameters suggested by the more recent model by Bordbar et al. [85] was found to give most accurate results.
3. The increase of CO_2 content in the oxidizer mixture decreased the maximum flame temperature and the temperature at the exhaust. The fraction of heat loss from the combustion gases through radiation decreases with the increase of CO_2 content. However, the increase of CO_2 content increases the CO emission at the exhaust for stoichiometric condition (Φ=1). When a small amount of excess oxygen is added to the combustor (Φ=0.98) the CO emission drastically reduces at higher CO_2 content. The radiation fraction, however, increases as the combustion condition is shifted to the leaner side. There is very little change in the maximum flame temperature and the temperature at exhaust with decrease in equivalence ratio. The increase in energy level leads to higher temperatures inside the combustor and lower CO emissions. The radiation fraction was also found to decrease with the increase in the energy level.
4. The burner head was modified to increase the swirl angle of the flow at the plane where the fuel and the oxidizer meet. When the diameter of the burner head inlet and exit is increased simultaneously, the swirl angle was found to increase.

6.2 Recommendations

Oxyfuel combustion is a promising method for moving towards clean combustion to meet the energy demands of the ever-increasing population. The presented work aimed at tackling stability, temperature distribution and emission for oxyfuel combustion of methane at stoichiometry. Recommendations for future work,

1. In the present work, the fuel and the oxidizer were allowed to enter the combustion chamber at low temperatures, which might not be the case in practical applications, where CO_2 from the flue gas is recycled into the combustor. Thus, it might be interesting to examine the effect of preheating fuel and oxidizer on the temperature and emissions for oxyfuel combustion of methane at stoichiometry.
2. In the present work, stability was studied experimentally. It will be of utmost importance and of interest to model the stability of oxyfuel combustors numerically. This will provide a much better understanding of phenomenon leading to instability, which would save significant experimental resources.
3. The impact of soot radiation was ignored, which might be of interest, especially, at high temperatures, which are characteristics of oxyfuel combustion.

REFERENCES

[1] International Energy Agency, CO2 emissions from fuel combustion, Paris, 2016. doi:10.1787/co2_fuel-2016-en.

[2] IPCC, T.F. Stocker, D. Qin, G.-K. Plattner, M. Tignor, S.K. Allen, J. Boschung, A. Nauels, Y. Xia, V. Bex, P.M. Midgley, Climate Change 2013: The Physical Science Basis. Contribution of Working Group I to the Fifth Assessment Report of the Intergovernmental Panel on Climate Change, Cambridge University Press, Cambridge, United Kingdom and New York, NY, USA, 2013. doi:10.1017/CBO9781107415324.

[3] UNFCCC. Conference of the Parties (COP), Adoption of the Paris Agreement, 2015. doi:FCCC/CP/2015/L.9/Rev.1.

[4] IEA, World Energy Outlook 2016, IEA, Paris, 2016. doi:10.1787/weo-2016-en.

[5] G. Prati, B. Zani, The Effect of the Fukushima Nuclear Accident on Risk Perception, Antinuclear Behavioral Intentions, Attitude, Trust, Environmental Beliefs, and Values, Environ. Behav. 45 (2013) 782–798. doi:10.1177/0013916512444286.

[6] T. Perko, C. Turcanu, D. Gennen, Media reporting and changes in public opinion after Fukushima nuclear accident : Belgium as case study, Int . J . Nucl. Gov. , Econ. Ecol. 3 (2012) 291–307. doi:10.1504/IJNGEE.2012.053559.

[7] M. Siegrist, V.H.M. Visschers, Acceptance of nuclear power: The Fukushima effect, Energy Policy. 59 (2013) 112–119. doi:10.1016/j.enpol.2012.07.051.

[8] W. Poortinga, M. Aoyagi, N.F. Pidgeon, Public perceptions of climate change and energy futures before and after the Fukushima accident: A comparison between Britain and Japan, Energy Policy. 62 (2013) 1204–1211. doi:10.1016/j.enpol.2013.08.015.

[9] Y. Kim, M. Kim, W. Kim, Effect of the Fukushima nuclear disaster on global public acceptance of nuclear energy, Energy Policy. 61 (2013) 822–828. doi:10.1016/j.enpol.2013.06.107.

[10] IEA, Renewables Information 2013, Paris, 2013. doi:10.1787/renew-2013-en.

[11] O. Ellabban, H. Abu-Rub, F. Blaabjerg, Renewable energy resources: Current status, future prospects and their enabling technology, Renew. Sustain. Energy Rev. 39 (2014) 748–764. doi:10.1016/j.rser.2014.07.113.

[12] International Energy Agency, Key world energy statistics, Statistics (Ber). (2016) 80. doi:10.1787/key_energ_stat-2016-en.

[13] M.A. Nemitallah, M.A. Habib, Experimental and numerical investigations of an atmospheric diffusion oxy-combustion flame in a gas turbine model combustor, Appl. Energy. 111 (2013) 401–415. doi:10.1016/j.apenergy.2013.05.027.

[14] E.S. Rubin, C. Chen, A.B. Rao, Cost and performance of fossil fuel power plants with CO2 capture and storage, Energy Policy. 35 (2007) 4444–4454. doi:10.1016/j.enpol.2007.03.009.

[15] R.M. Cuéllar-Franca, A. Azapagic, Carbon capture, storage and utilisation technologies: A critical analysis and comparison of their life cycle environmental impacts, J. CO2 Util. 9 (2015) 82–102. doi:10.1016/j.jcou.2014.12.001.

[16] J.D. Figueroa, T. Fout, S. Plasynski, H. McIlvried, R.D. Srivastava, Advances in CO2 capture technology-The U.S. Department of Energy's Carbon Sequestration Program, Int. J. Greenh. Gas Control. 2 (2008) 9–20. doi:10.1016/S1750-5836(07)00094-1.

[17] K. Jordal, M. Anheden, J. Yan, L. Strömberg, Oxyfuel combustion for coal-fired power generation with CO2 capture-Opportunities and challenges, Greenh. Gas Control Technol. (2005) 201–209. doi:10.1016/B978-008044704-9/50021-5.

[18] T. Kuramochi, A. Ramírez, W. Turkenburg, A. Faaij, Comparative assessment of CO2 capture technologies for carbon-intensive industrial processes, Prog. Energy Combust. Sci. 38 (2012) 87–112. doi:10.1016/j.pecs.2011.05.001.

[19] D. Singh, E. Croiset, P.L. Douglas, M.A. Douglas, Techno-economic study of CO2 capture from an existing coal-fired power plant: MEA scrubbing vs. O2/CO2 recycle combustion, Energy Convers. Manag. 44 (2003) 3073–3091. doi:10.1016/S0196-8904(03)00040-2.

[20] N. Nsakala, C. Bozzuto, Engineering Feasiblity of CO2 capture on an existing coal-fired power plant, in: Conf. Carbon Sequestration, 2001.

[21] G.A. Richards, K.H. Casleton, B.T. Chorpening, CO2 and H2O diluted oxy-fuel combustion for zero-emission power, Proc. Inst. Mech. Eng. Part A J. Power Energy. 219 (2005) 121–126. doi:10.1243/095765005X5990.

[22] B.M. Abraham, J.G. Asbury, E.P. Lynch, A.P.S. Teotia, Coal-oxygen process provides CO2 for enhanced recovery, (1982). http://www.osti.gov/scitech/servlets/purl/5173184.

[23] R. Stanger, T. Wall, R. Spörl, M. Paneru, S. Grathwohl, M. Weidmann, G.

Scheffknecht, D. McDonald, K. Myöhänen, J. Ritvanen, S. Rahiala, T. Hyppänen, J. Mletzko, A. Kather, S. Santos, Oxyfuel combustion for CO2 capture in power plants, Int. J. Greenh. Gas Control. 40 (2015) 55–125. doi:10.1016/j.ijggc.2015.06.010.

[24] G. Scheffknecht, L. Al-Makhadmeh, U. Schnell, J. Maier, Oxy-fuel coal combustion-A review of the current state-of-the-art, Int. J. Greenh. Gas Control. 5 (2011) 16–35. doi:10.1016/j.ijggc.2011.05.020.

[25] T. Wall, Y. Liu, C. Spero, L. Elliott, S. Khare, R. Rathnam, F. Zeenathal, B. Moghtaderi, B. Buhre, C. Sheng, R. Gupta, T. Yamada, K. Makino, J. Yu, An overview on oxyfuel coal combustion-State of the art research and technology development, Chem. Eng. Res. Des. 87 (2009) 1003–1016. doi:10.1016/j.cherd.2009.02.005.

[26] B.J.P. Buhre, L.K. Elliott, C.D. Sheng, R.P. Gupta, T.F. Wall, Oxy-fuel combustion technology for coal-fired power generation, Prog. Energy Combust. Sci. 31 (2005) 283–307. doi:10.1016/j.pecs.2005.07.001.

[27] M.A. Habib, H.M. Badr, S.F. Ahmed, R. Ben-Mansour, K. Mezghani, S. Imashuku, G.J. la O', Y. Shao-Horn, N.D. Mancini, A. Mitsos, P. Kirchen, A.F. Ghoneim, A review of recent developments in carbon capture utilizing oxy-fuel combustion in conventional and ion transport membrane systems, Int. J. Energy Res. 35 (2011) 741–764. doi:10.1002/er.1798.

[28] I. Hadjipaschalis, G. Kourtis, A. Poullikkas, Assessment of oxyfuel power generation technologies, Renew. Sustain. Energy Rev. 13 (2009) 2637–2644. doi:10.1016/j.rser.2009.07.001.

[29] Y. Tan, M.A. Douglas, K. V. Thambimuthu, CO2 capture using oxygen enhanced combustion strategies for natural gas power plants, Fuel. 81 (2002) 1007–1016. doi:10.1016/S0016-2361(02)00014-5.

[30] J. Maier, B. Dhungel, P. Mönckert, G. Scheffknecht, Combustion and emission behaviour under oxy-fuel condition. 39, in: Kraftwerkstechnisches Kolloquium, 2007: pp. 11–12.

[31] J. Maier, B. Dhungel, P. Mönckert, G. Scheffknecht, Coal combustion and emission behaviour under oxy-fuel combustion, in: Proc. 31st Int. Tech. Conf. Coal Util. Fuel Syst., 2006.

[32] P.J. Edge, P.J. Heggs, M. Pourkashanian, P.L. Stephenson, A. Williams, A reduced order full plant model for oxyfuel combustion, Fuel. 101 (2012) 234–243. doi:10.1016/j.fuel.2011.05.005.

[33] M. Ditaranto, T. Oppelt, Radiative heat flux characteristics of methane flames in oxy-fuel atmospheres, Exp. Therm. Fluid Sci. 35 (2011) 1343–1350. doi:10.1016/j.expthermflusci.2011.05.002.

[34] H.K. Kim, Y. Kim, S.M. Lee, K.Y. Ahn, Studies on combustion characteristics and flame length of turbulent oxy-fuel flames, Energy and Fuels. 21 (2007) 1459–1467. doi:10.1021/ef060346g.

[35] G.C. Krieger, A.P. V Campos, M.D.B. Takehara, F. Alfaia Da Cunha, C.A. Gurgel Veras, Numerical simulation of oxy-fuel combustion for gas turbine applications, Appl. Therm. Eng. 78 (2015) 471–481. doi:10.1016/j.applthermaleng.2015.01.001.

[36] P. Kutne, B.K. Kapadia, W. Meier, M. Aigner, Experimental analysis of the combustion behaviour of oxyfuel flames in a gas turbine model combustor, Proc. Combust. Inst. 33 (2011) 3383–3390. doi:10.1016/j.proci.2010.07.008.

[37] M. Ditaranto, J. Hals, Combustion instabilities in sudden expansion oxy-fuel flames, Combust. Flame. 146 (2006) 493–512. doi:10.1016/j.combustflame.2006.04.015.

[38] K. Andersson, F. Johnsson, Flame and radiation characteristics of gas-fired O2/CO2 combustion, Fuel. 86 (2007) 656–668. doi:10.1016/j.fuel.2006.08.013.

[39] K. Andersson, F. Johnsson, Combustion and flame characteristics of oxy-fuel combustion-experimental activities within the Encap project, in: Proc. GHGT-8 Conf. Trondheim, 2006, 2006.

[40] K. Andersson, F. Johnsson, Radiative Properties of A 100 kW Oxy-fuel flame--Experiments and Modelling of the Chalmers test facility, in: Proc. Clear. Conf. Florida, 2006, 2006.

[41] P. Heil, D. Toporov, H. Stadler, S. Tschunko, M. Förster, R. Kneer, Development of an oxycoal swirl burner operating at low O2 concentrations, Fuel. 88 (2009) 1269–1274. doi:10.1016/j.fuel.2008.12.025.

[42] C.Y. Liu, G. Chen, N. Sip??cz, M. Assadi, X.S. Bai, Characteristics of oxy-fuel combustion in gas turbines, Appl. Energy. 89 (2012) 387–394. doi:10.1016/j.apenergy.2011.08.004.

[43] M.A. Habib, M.A. Nemitallah, P. Ahmed, M.H. Sharqawy, H.M. Badr, I. Muhammad, M. Yaqub, Experimental analysis of oxygen-methane combustion inside a gas turbine reactor under various operating conditions, Energy. 86 (2015) 105–114. doi:10.1016/j.energy.2015.03.120.

[44] M.A. Habib, S.S. Rashwan, M.A. Nemitallah, A. Abdelhafez, Stability maps of non-premixed methane flames in different oxidizing environments of a gas turbine model

combustor, Appl. Energy. 189 (2017) 177–186. doi:10.1016/j.apenergy.2016.12.067.

[45] S. Seepana, S. Jayanti, Flame structure and NO generation in oxy-fuel combustion at high pressures, Energy Convers. Manag. 50 (2009) 1116–1123. doi:10.1016/j.enconman.2008.11.005.

[46] S. Seepana, S. Jayanti, Experimental studies of flame extinction in a swirl-stabilized oxy-fuel burner, Fuel. 93 (2012) 75–81. doi:10.1016/j.fuel.2011.10.065.

[47] S. Seepana, S. Jayanti, Steam-moderated oxy-fuel combustion, Energy Convers. Manag. 51 (2010) 1981–1988. doi:10.1016/j.enconman.2010.02.031.

[48] S. Seepana, S. Jayanti, Flame structure investigations of oxy-fuel combustion, Fuel. 93 (2012) 52–58. doi:10.1016/j.fuel.2011.07.033.

[49] C. Zhang, A. Atreya, K. Lee, Sooting structure of methane counterflow diffusion flames with preheated reactants and dilution by products of combustion, Symp. Combust. 24 (1992) 1049–1057. doi:10.1016/S0082-0784(06)80124-4.

[50] P. Glarborg, L. Bentzen, Chemical effects of a high CO2 concentration in oxy-fuel combustion of methane, Energy & Fuels. (2007) 291–296. doi:10.1021/ef7005854.

[51] F.M. White, I. Corfield, Viscous fluid flow, McGraw-Hill New York, 2006.

[52] K.K.J. Ranga Dinesh, J.A. Van Oijen, K.H. Luo, X. Jiang, Near-field local flame extinction of oxy-syngas non-premixed jet flames: A DNS study, Fuel. 130 (2014) 189–196. doi:10.1016/j.fuel.2014.04.011.

[53] K.K.J.R. Dinesh, E.S. Richardson, J.A. Van Oijen, K.H. Luo, X. Jiang, The Scalar Structure of Turbulent Oxy-fuel Non-premixed Flames, Phys. Procedia. 66 (2015) 305–308. doi:10.1016/j.egypro.2015.02.066.

[54] M.A. Habib, R. Ben-Mansour, H.M. Badr, S.F. Ahmed, A.F. Ghoniem, Computational fluid dynamic simulation of oxyfuel combustion in gas-fired water tube boilers, Comput. Fluids. 56 (2012) 152–165. doi:10.1016/j.compfluid.2011.12.009.

[55] M. Aliyu, M.A. Nemitallah, S.A. Said, M.A. Habib, Characteristics of H 2 -enriched CH 4 eO 2 diffusion flames in a swirl-stabilized gas turbine combustor: Experimental and numerical study, Int. J. Hydrogen Energy. 41 (2016) 20418–20432. doi:10.1016/j.ijhydene.2016.08.144.

[56] and A.S.L. Bergman, Theodore L., Frank P. Incropera, Fundamentals of Heat and Mass Transfer, John Wiley & Sons, 2011.

[57] A. Fluent, 12.0 Theory Guide, Ansys Inc. (2009).

[58] H. MagnussenBF, On mathematical models of turbulent combustion with special emphasis on soot formation and combustion, 16thSymp.(Int'l.) onCombustion. TheCombustionInstitute. (1976).

[59] B. Magnussen, On the structure of turbulence and a generalized eddy dissipation concept for chemical reaction in turbulent flow, in: 19th Aerosp. Sci. Meet., 1981: p. 42.

[60] G.P. Smith, D.M. Golden, M. Frenklach, N.W. Moriarty, B. Eiteneer, M. Goldenberg, C.T. Bowman, R.K. Hanson, S. Song, W.C. Gardiner Jr, others, GRI-Mech 3.0, URL Http//www. Me. Berkeley. Edu/gri_mech. 51 (1999) 55.

[61] J. Andersen, C.L. Rasmussen, T. Giselsson, P. Glarborg, Global combustion mechanisms for use in CFD modeling under oxy-fuel conditions, Energy and Fuels. 23 (2009) 1379–1389. doi:10.1021/ef8003619.

[62] W.P. Jones, R.P. Lindstedt, Global reaction schemes for hydrocarbon combustion, Combust. Flame. 73 (1988) 233–249. doi:10.1016/0010-2180(88)90021-1.

[63] R.W. Bilger, S.H. Stårner, R.J. Kee, On reduced mechanisms for methaneair combustion in nonpremixed flames, Combust. Flame. 80 (1990) 135–149. doi:10.1016/0010-2180(90)90122-8.

[64] P. Glarborg, N.I. Lilleheie, S. Byggstøyl, B.F. Magnussen, P. Kilpinen, M. Hupa, A reduced mechanism for nitrogen chemistry in methane combustion, Symp. Combust. 24 (1992) 889–898. doi:10.1016/S0082-0784(06)80106-2.

[65] C.K. Westbrook, F.L. Dryer, Simplified Reaction Mechanisms for the Oxidation of Hydrocarbon Fuels in Flames, Combust. Sci. Technol. 27 (1981) 31–43. doi:10.1080/00102208108946970.

[66] A. Frassoldati, A. Cuoci, T. Faravelli, Simplified kinetic schemes for oxy-fuel combustion, in: 1st Int. Conf. Sustain. Foss. Fuels Futur. Energy, 2009: pp. 6–10. http://www.co2club.it/agenda/full paper/frassoldati_full paper.pdf.

[67] E. Ranzi, A. Frassoldati, S. Granata, T. Faravelli, Wide-Range Kinetic Modeling Study of the Pyrolysis, Partial Oxidation, and Combustion of Heavy n -Alkanes, Ind. Eng. Chem. Res. 44 (2005) 5170–5183. doi:10.1021/ie049318g.

[68] C. Yin, L.A. Rosendahl, S.K. Kær, Chemistry and radiation in oxy-fuel combustion: A computational fluid dynamics modeling study, Fuel. 90 (2011) 2519–2529. doi:10.1016/j.fuel.2011.03.023.

[69] J.P. Kim, U. Schnell, G. Scheffknecht, Comparison of Different Global Reaction Mechanisms for MILD Combustion of Natural Gas, Combust. Sci. Technol. 180 (2008) 565–592. doi:10.1080/00102200701838735.

[70] R. Viskanta, Radiation heat transfer in combustion systems, Prog. Energy Combust. Sci. 13 (1987) 97–160. doi:10.1016/0360-1285(87)90008-6.

[71] J.R. Howell, M.P. Menguc, R. Siegel, Thermal radiation heat transfer, 5th Editio, CRC press, Boca Raton, Florida, 2010.

[72] S. (Subrahmanyan) Chandrasekhar, Radiative transfer, Dover Publications, 1960. https://books.google.com.sa/books?hl=en&lr=&id=1YHCAgAAQBAJ&oi=fnd&pg=PP1&dq=s+chandrasekhar+radiative+transfer+dover+publication&ots=GrHKlwY0E1&sig=O3glJqyFKaA33KjP0eJ8R3dveFQ&redir_esc=y#v=onepage&q=schandrasekhar radiative transfer dover publication&f=false (accessed March 25, 2017).

[73] B.M. Herman, S.R. Browning, A Numerical Solution to the Equation of Radiative Transfer, J. Atmos. Sci. 22 (1965) 559–566.

[74] M.A. Heaslet, R.F. Warming, Radiative transport and wall temperature slip in an absorbing planar medium, Int. J. Heat Mass Transf. 8 (1965) 979–994. doi:10.1016/0017-9310(67)90029-4.

[75] K. Stamnes, S.C. Tsay, W. Wiscombe, K. Jayaweera, Numerically stable algorithm for discrete-ordinate-method radiative transfer in multiple scattering and emitting layered media., Appl. Opt. 27 (1988) 2502–2509. doi:10.1364/AO.27.002502.

[76] D.K. Edwards, Molecular gas band radiation, in: Adv. Heat Transf. Vol. 12. New York, Acad. Press. Inc., 1976, P. 115-193., 1976: pp. 115–193.

[77] H.C. Hottel, A.F. Sarofim, Radiative transport, McGraw Hill, New York. (1965).

[78] T.F. Smith, Z.F. Shen, J.N. Friedman, Evaluation of Coefficients for the Weighted Sum of Gray Gases Model, J. Heat Transfer. 104 (1982) 602. doi:10.1115/1.3245174.

[79] R. Porter, F. Liu, M. Pourkashanian, A. Williams, D. Smith, Evaluation of solution methods for radiative heat transfer in gaseous oxy-fuel combustion environments, J. Quant. Spectrosc. Radiat. Transf. 111 (2010) 2084–2094. doi:10.1016/j.jqsrt.2010.04.028.

[80] R. Johansson, K. Andersson, B. Leckner, H. Thunman, Models for gaseous radiative heat transfer applied to oxy-fuel conditions in boilers, Int. J. Heat Mass Transf. 53 (2010) 220–230. doi:10.1016/j.ijheatmasstransfer.2009.09.039.

[81] C. Yin, L.C.R. Johansen, L.A. Rosendahl, S.K. Kær, New weighted sum of gray gases model applicable to computational fluid dynamics (CFD) modeling of oxy-fuel combustion: Derivation, validation, and implementation, Energy and Fuels. 24 (2010) 6275–6282. doi:10.1021/ef101211p.

[82] R. Johansson, B. Leckner, K. Andersson, F. Johnsson, Account for variations in the H2O to CO2 molar ratio when modelling gaseous radiative heat transfer with the weighted-sum-of-grey-gases model, Combust. Flame. 158 (2011) 893–901. doi:10.1016/j.combustflame.2011.02.001.

[83] T. Kangwanpongpan, F.H.R. França, R. Corrêa Da Silva, P.S. Schneider, H.J. Krautz, New correlations for the weighted-sum-of-gray-gases model in oxy-fuel conditions based on HITEMP 2010 database, Int. J. Heat Mass Transf. 55 (2012) 7419–7433. doi:10.1016/j.ijheatmasstransfer.2012.07.032.

[84] L.J. Dorigon, G. Duciak, R. Brittes, F. Cassol, M. Galarça, F.H.R. França, WSGG correlations based on HITEMP2010 for computation of thermal radiation in non-isothermal, non-homogeneous H2O/CO2 mixtures, Int. J. Heat Mass Transf. 64 (2013) 863–873. doi:10.1016/j.ijheatmasstransfer.2013.05.010.

[85] M.H. Bordbar, G. Wecel, T. Hyppanen, A line by line based weighted sum of gray gases model for inhomogeneous CO2-H2O mixture in oxy-fired combustion, Combust. Flame. 161 (2014) 2435–2445. doi:10.1016/j.combustflame.2014.03.013.

[86] M.A. Rajhi, R. Ben-Mansour, M.A. Habib, M.A. Nemitallah, K. Andersson, Evaluation of gas radiation models in CFD modeling of oxy-combustion, Energy Convers. Manag. 81 (2014) 83–97. doi:10.1016/j.enconman.2014.02.019.

[87] V. Kez, F. Liu, J.L. Consalvi, J. Strohle, B. Epple, A comprehensive evaluation of different radiation models in a gas turbine combustor under conditions of oxy-fuel combustion with dry recycle, J. Quant. Spectrosc. Radiat. Transf. 172 (2016) 121–133. doi:10.1016/j.jqsrt.2015.11.002.

[88] V. Di Sarli, A. Di Benedetto, Effects of non-equidiffusion on unsteady propagation of hydrogen-enriched methane/air premixed flames, Int. J. Hydrogen Energy. 38 (2013) 7510–7518. doi:10.1016/j.ijhydene.2013.03.126.

[89] V. Di Sarli, A. Di Benedetto, E.J. Long, G.K. Hargrave, Time-Resolved Particle Image Velocimetry of dynamic interactions between hydrogen-enriched methane/air premixed flames and toroidal vortex structures, Int. J. Hydrogen Energy. 37 (2012) 16201–16213. doi:10.1016/j.ijhydene.2012.08.061.

[90] E.R. Hawkes, J.H. Chen, Direct numerical simulation of hydrogen-enriched lean premixed methane-air flames, Combust. Flame. 138 (2004) 242–258.

doi:10.1016/j.combustflame.2004.04.010.

[91] A.M. Briones, S.K. Aggarwal, V.R. Katta, A numerical investigation of flame liftoff, stabilization, and blowout, Phys. Fluids. 18 (2006). doi:10.1063/1.2191851.

[92] D.H. Um, J.M. Joo, S. Lee, O.C. Kwon, Combustion stability limits and NOx emissions of nonpremixed ammonia-substituted hydrogen-air flames, Int. J. Hydrogen Energy. 38 (2013) 14854–14865. doi:10.1016/j.ijhydene.2013.08.140.

[93] S.A.A. El-Ghafour, A.H.E. El-dein, A.A.R. Aref, Combustion characteristics of natural gas-hydrogen hybrid fuel turbulent diffusion flame, Int. J. Hydrogen Energy. 35 (2010) 2556–2565. doi:10.1016/j.ijhydene.2009.12.049.

[94] K.M. Lyons, Toward an understanding of the stabilization mechanisms of lifted turbulent jet flames: Experiments, Prog. Energy Combust. Sci. 33 (2007) 211–231. doi:10.1016/j.pecs.2006.11.001.

[95] J. Buckmaster, Edge-flames, Prog. Energy Combust. Sci. 28 (2002) 435–475. doi:10.1016/S0360-1285(02)00008-4.

[96] N. Peters, F.A. Williams, Liftoff characteristics of turbulent jet diffusion flames, AIAA J. 21 (1983) 423–429. doi:10.2514/3.8089.

[97] F. Takahashi, V.R. Katta, A reaction kernel hypothesis for the stability limit of methane jet diffusion flames, Proc. Combust. Inst. 28 (2000) 2071–2078. doi:10.1016/S0082-0784(00)80615-3.

[98] S.A. Filatyev, J.F. Driscoll, C.D. Carter, J.M. Donbar, Measured properties of turbulent premixed flames for model assessment, including burning velocities, stretch rates, and surface densities, Combust. Flame. 141 (2005) 1–21. doi:10.1016/j.combustflame.2004.07.010.

[99] J. Park, J.S. Kim, J.O. Chung, J.H. Yun, S.I. Keel, Chemical effects of added CO2 on the extinction characteristics of H2/CO/CO2 syngas diffusion flames, Int. J. Hydrogen Energy. 34 (2009) 8756–8762. doi:10.1016/j.ijhydene.2009.08.046.

[100] A.R. Choudhuri, S.R. Gollahalli, Characteristics of hydrogen-hydrocarbon composite fuel turbulent jet flames, Int. J. Hydrogen Energy. 28 (2003) 445–454. doi:10.1016/S0360-3199(02)00063-0.

[101] J. Oh, D. Noh, C. Ko, The effect of hydrogen addition on the flame behavior of a non-premixed oxy-methane jet in a lab-scale furnace, Energy. 62 (2013) 362–369. doi:10.1016/j.energy.2013.09.049.

[102] J. Oh, D. Noh, Lifted flame behavior of a non-premixed oxy-methane jet in a lab-

scale slot burner, Fuel. 103 (2013) 862–868.

[103] R.H. Chen, J.F. Driscoll, Nitric oxide levels of jet diffusion flames: Effects of coaxial air and other mixing parameters, Symp. Combust. 23 (1991) 281–288. doi:10.1016/S0082-0784(06)80271-7.

[104] W.J. a. Dahm, A.G. Mayman, Blowout limits of turbulent jet diffusion flames for arbitrary source conditions, AIAA J. 28 (1990) 1157–1162. doi:10.2514/3.25186.

[105] M. Kim, J. Oh, Y. Yoon, Flame length scaling in a non-premixed turbulent diluted hydrogen jet with coaxial air, Fuel. 90 (2011) 2624–2629. doi:10.1016/j.fuel.2011.03.036.

[106] R. Kitamura, L. Pilon, M. Jonasz, Optical constants of silica glass from extreme ultraviolet to far infrared at near room temperature, Appl. Opt. 46 (2007) 8118. doi:10.1364/AO.46.008118.

[107] S.S. Shy, Y.C. Chen, C.H. Yang, C.C. Liu, C.M. Huang, Effects of H2 or CO2 addition, equivalence ratio, and turbulent straining on turbulent burning velocities for lean premixed methane combustion, Combust. Flame. 153 (2008) 510–524. doi:10.1016/j.combustflame.2008.03.014.

[108] S.S. Shy, S.I. Yang, W.J. Lin, R.C. Su, Turbulent burning velocities of premixed CH4/diluent/air flames in intense isotropic turbulence with consideration of radiation losses, Combust. Flame. 143 (2005) 106–118. doi:10.1016/j.combustflame.2005.05.007.

[109] M. Abián, J. Giménez-López, R. Bilbao, M.U. Alzueta, Effect of different concentration levels of CO2 and H2O on the oxidation of CO: Experiments and modeling, Proc. Combust. Inst. 33 (2011) 317–323. doi:http://dx.doi.org/10.1016/j.proci.2010.05.078.

[110] A.K. Gupta, D.G. Lilley, N. Syred, Swirl flows, Tunbridge Wells, Kent, England, Abacus Press. 1984, 488 P. (1984).

[111] H. El-Asrag, S. Menon, Large eddy simulation of bluff-body stabilized swirling non-premixed flames, Proc. Combust. Inst. 31 II (2007) 1747–1754. doi:10.1016/j.proci.2006.07.251.

VITAE

Name:	Mohammad Raghib Shakeel
Date of Birth:	8th May 1991
Nationality:	Indian
Gender:	Male
Current Address:	Mechanical Engineering Department, King Fahd University of Petroleum and Minerals
Permanent Address:	New Delhi, India
Contact Number:	+966549417946
Email address:	raghib@kfupm.edu.sa, ragshakeel@gmail.com

Education:

M.Sc. Mechanical Engineering

King Fahd University of Petroleum and Minerals**,** Dhahran, Saudi Arabia, May 2017

B.Tech. Mechanical Engineering

Faculty of Engineering and Technology,

Jamia Millia Islamia,

New Delhi, India, June 2013

Publications:

1. M.R. Shakeel, J. Al-Sadah, E.M.A. Mokheimer, Analytical and Numerical Modeling of Solar Chimney, J. Energy Resour. Technol. (in press) (2017) 1–11. doi:10.1115/1.4035782.
2. Y.S. Sanusi, E.M.A. Mokheimer, M.R. Shakeel, Z. Abubakar, M.A. Habib, Oxy-Combustion of Hydrogen-Enriched Methane: Experimental Measurements and Analysis, Energy & Fuels. (2017) acs.energyfuels.6b03118. doi:10.1021/acs.energyfuels.6b03118.
3. E.M.A. Mokheimer, M.R. Shakeel, J. Al-Sadah, A Novel Design of Solar Chimney for Cooling Load Reduction and other Applications in Buildings (under review)